University of HUDDERSFIELD

University of Huddersfield Repository

Chuku, Difference

A NOVEL STRUCTURAL MONITORING SYSTEM BASED ON A LOW-COST DISPLACEMENT SENSING TECHNIQUE AND IN-SITU CALIBRATION

Original Citation

Chuku, Difference (2021) A NOVEL STRUCTURAL MONITORING SYSTEM BASED ON A LOW-COST DISPLACEMENT SENSING TECHNIQUE AND IN-SITU CALIBRATION. Doctoral thesis, University of Huddersfield.

This version is available at https://eprints.hud.ac.uk/id/eprint/35774/

The University Repository is a digital collection of the research output of the University, available on Open Access. Copyright and Moral Rights for the items on this site are retained by the individual author and/or other copyright owners. Users may access full items free of charge; copies of full text items generally can be reproduced, displayed or performed and given to third parties in any format or medium for personal research or study, educational or not-for-profit purposes without prior permission or charge, provided:

- The authors, title and full bibliographic details is credited in any copy;
- A hyperlink and/or URL is included for the original metadata page; and
- The content is not changed in any way.

For more information, including our policy and submission procedure, please contact the Repository Team at: E.mailbox@hud.ac.uk.

http://eprints.hud.ac.uk/

A NOVEL STRUCTURAL MONITORING SYSTEM BASED ON A LOW-COST DISPLACEMENT SENSING TECHNIQUE AND IN-SITU CALIBRATION

DIFFERENCE CHUKU

A thesis submitted to the University of Huddersfield in partial fulfilment of the requirements for the degree of Doctor of Philosophy.

Date of Submission: 08/06/2021

Copyright statement

i. The author of this thesis (including any appendices and/or schedules to this thesis) owns any copyright in it (the "Copyright") and s/he has given The University of Huddersfield the right to use such copyright for any administrative, promotional, educational and/or teaching purposes.

ii. Copies of this thesis, either in full or in extracts, may be made only in accordance with the regulations of the University Library. Details of these regulations may be obtained from the Librarian. This page must form part of any such copies made.

iii. The ownership of any patents, designs, trademarks and any and all other intellectual property rights except for the Copyright (the "Intellectual Property Rights") and any reproductions of copyright works, for example graphs and tables ("Reproductions"), which may be described in this thesis, may not be owned by the author and may be owned by third parties. Such Intellectual Property Rights and Reproductions cannot and must not be made available for use without the prior written permission of the owner(s) of the relevant Intellectual Property Rights and/or Reproductions

Abstract

The need for metrological systems with new capacities to perform measurements that go beyond the limits of existing measurement systems is being driven by recent technological advancements and innovation. Structures of machines distort due to thermal and finite stiffness effects which affect their performance hence the need for structural monitoring. At the design stage of machines and instruments, metrology must be embedded and accessed as part of the machines' and instruments' functioning. Structures of machines distort due to thermal and finite stiffness effects which affect their performance hence the need for structural monitoring. This need is not met by existing measurement systems and is the drive for innovation of new metrological systems. The result of this may take the form of metrological systems embedded in machines and instruments during the design stage to add structural monitoring functionality to the devices.

The performance specification for embedded sensing techniques is very strict regarding dimensional stability. The materials currently used in precision measurement systems have some limitations that preclude their use for most applications. Different methods and materials are being investigated for future precision measurement systems. The main properties considered are good dimensional stability, light weight, and low cost. Although strain measurement of a structural part is ubiquitous in many safety-critical systems, it is rarely employed in precision machinery to allow for error correction. This could be owing to the difficulty of installing multiple sensors to characterise complex bending of structural parts and the associated cost of embedding precision sensors. Every sensor has shortcomings, and knowing these limitations is important for accurately assessing a system's performance. Many well-defined parameters can provide a detailed characterisation of a sensor's output, rather than just specifying the quality of a sensor in terms of accuracy. Using special configurations and techniques, a designer may also minimise the impact of a sensor's inherent limitations.

In this thesis, the design of a new structural deformation monitoring system based on a low-cost displacement sensing methodology using off-the-shelf slotted photomicrosensors and connecting rods is investigated. The uncertainty contributors are investigated and a technique for in-situ calibration of the sensor is developed. This is especially important for embedded applications where it is impractical or costly to remove the sensors.

The sensor design incorporates a differential voltage technique that reduces the influence of variation in input voltage, ambient light variations and differential thermally induced expansion between the sensor circuit and shutter. Traditional rigid link mechanisms move due to rolling or sliding but this is undesirable as they can induce hysteresis, wear, and backlash. To overcome this limitation and provide precise displacements at the application of a force, a flexure mechanism was designed. The output of the sensor showed 90% correlation at zero lag to the output of a laser interferometer.

Misalignment of the sensors can occur due to vibration for example, which can affect the calibration accuracy. In an embedded application, it is impossible to ascertain which sensors have been misaligned during installation without removing the sensors. This is also true for long term variability such as drift or possible misalignment or damage during maintenance of the machinery on which the sensor is installed. To facilitate in-situ calibration, a self-excitation technique was developed utilising controlled voltage excitation to detect and correct for variation during the lifetime of the sensor while it is embedded on a machine. The voltage calibration technique achieved 60% reduction of errors due to shutter movements.

A limitation of the flexure mechanism is the introduction of additional stiffness. To reduce the stiffness introduced by the flexure mechanism and reduce the cost of machining intricate parts of the sensor by traditional means, an improved 3D printed design of the sensor is created. The sensor was configured together with suitable connecting rods to form a framework for measuring structural deformation. Simulation results show the reduced flexure stiffness resulting in 30% reduction in compression/tension losses of the connecting

rods. The results also show that the improved design measures over 50% more strain than the traditionally manufactured sensor.
Finally, the characterisation results are used to develop an uncertainty budget for a system that utilises the newly developed sensor for structural deformation monitoring. A total uncertainty of 4 μm was achieved for a system that uses the sensor for structural monitoring.

Acknowledgement

Working as a Ph.D. student at the Centre for Precision Technologies – ECMPG group has been a challenging and rewarding experience to me, made possible with the support and encouragement of various people in my life who either directly or indirectly contributed towards my effort in accomplishing this achievement.

Firstly, I would like to express my deepest gratitude to my supervisor Dr Simon Fletcher whose continuous supervision made it possible for me to perform the complex experiments presented in this thesis. His support and guidance is invaluable to the completion of this work. I would like to thank him for his patience, time, and understanding throughout this journey. I do not imagine that I would have accomplished this feat without his support.

I would also like to thank my co-supervisor Prof. Andrew Longstaff, for his guidance and contribution which boosted my confidence throughout the course of my Ph.D. Our meetings and interactions always left me relaxed and with a fresh perspective.

Secondly, my sincere thanks to my family – My parents – Chief & Mrs Nelson Chuku and my siblings, and my Fiancee Mutale Kangote. I am privileged to have a family who has shown an enormous amount of faith & patience with me. No words are enough to express my thankfulness towards them.

I would also like to thank Dr Naeem Mian, Andrew Bell (Applications Engineer), my friends and colleagues. I wish to acknowledge the helpful suggestions and timely support provided throughout the course. I would also specially thank Tom Furness for his assistance whenever I reached out to him. Tom assisted me with the mechanical aspects of sensor design and in setting up experiments.

Thirdly, I would love to take the opportunity of thanking my funding body EPSRC, who supported this research work.

Finally, I return all the glory to God for the gift of life, for the wisdom and grace to complete this research work, and thesis.

Table of Contents

Contents

Abstract i
Acknowledgement iii
Table of Contents iv
List of Abbreviations vii
List of Figures viii
List of Tables x
Chapter 1 – Introduction 11
1.2. Machine Tool Error Reduction Techniques 14
1.2.1. Error Avoidance Methods 15
1.2.2. Error Compensation Methods 17
1.3. On-Machine Measurement 18
1.4. Motivation 20
1.5. Aims and Objectives 20
1.5.1. Aim 20
1.5.2. Objectives 21
1.6. Novelties and Contributions to Knowledge 21
1.7. List of Published Papers 22
1.8. Summary 22
Chapter 2 - Literature Review 24
2.1. Sources of Uncertainty in On-Machine Measurement 24
2.1.1. Machine tool 24
2.1.2. Environment 24
2.2. Structural Deformation Monitoring 25
2.2.1. Review of Strain Measurement Sensors 26
2.3. Review of Displacement Sensors 29
2.3.1. Review of low-cost solutions 32
2.3.2. Photomicrosensors 33
2.4. Review of Analytical Methods 40
2.4.1. Finite Element Method 40
2.5. Summary of Findings from Literature 42
2.6. Methodology 43
Chapter 3 - Sensor Design 46
3.1. Introduction 47
3.2. Sensor Design and Description 49
3.3. Flexure Mechanism 51

3.4. Dual sensor on example structure....56
3.5. Strain Measurement System....62
3.5.1. Multistrain Experimental Setup....63
3.6. Experimental Tests and Results....67
3.7. Summary....74
Chapter 4 - Measurement System Uncertainty Evaluation....75
4.1. Introduction....75
4.2. Characterisation of the Measurement System....77
4.3 Identification of Error Sources....82
4.4 Method for Evaluating Uncertainties....84
4.4.1. Linearity....85
4.4.2. Repeatability....87
4.4.3. Resolution....87
4.4.4. Reproducibility....87
4.4.5. Light Contamination....88
4.4.6. Uncertainty of Temperature Control....89
4.4.7. Drift and Stability....90
4.4.8. Uncertainty of CTE (Coefficient of Thermal Expansion)....91
4.4.9. Shutter Misalignment....92
4.4.10. Signal Conditioning Circuit....93
4.4.11 Abbe Error....94
4.4.12 Cosine Error....95
4.5. Uncertainty Budget....96
4.6. Summary....98
Chapter 5 – In-situ Voltage Calibration Technique....99
5.1 Introduction....99
5.2. Effect of shutter movement....101
5.3. Experiment Setup and System Description....103
5.4. Voltage Self-Calibration Method....106
5.5 Alternative Voltage Self-calibration Method....114
5.6. Shutter Movement Error Correction....115
5.7. Summary....119
Chapter 6 - Improved sensor module design....120
6.1. Introduction....120
6.2 Justification for the improved design....120
6.3. The Physical Principle of the Improved 3D Printed Sensor....122
6.4. Description of proposed design....124

6.4.1. Flexure System....125
6.4.2. Sensor adjustment post installation....125
6.4.3. Model testing and evaluation....127
6.5. Multi-sensor strain setup....128
6.6 Validation of Improved Design....134
6.6.1. Description of the Setup....134
6.6.2. Calibration of the System....136
6.6.3. Results and Discussion....136
6.7. Sensor cost....139
6.8. Summary....140
Chapter 7 - Conclusion and Future Work....141
7.1. Thesis Summary and Contributions....141
7.2. Future Work....143
References....145
Appendices....151

List of Abbreviations

Computer Numerically Controlled (CNC)

Photomicrosensors (PMS)

Electromagnetic Interference (EMI)

Carbon Fibre Reinforced Plastics (CFRP)

Fibre Bragg Grating (FBG)

Convolutional Neural Network (CNN)

Multiple Regression Analysis (MRA)

Coordinate Measuring Machines (CMM)

International Standard Organisation (ISO)

Guide to the Expression Of Uncertainty In Measurement (GUM)

Slotted Photomicrosensors (SPM)

Light Emitting Diode (LED)

Fabry-Perot Interferometric (FPI)

Radio Frequency Interference (RFI)

Forward Voltage (VF)

Forward Current (IF)

Light Current (IL)

Dark Current (ID)

Finite Element Method (FEM)

Finite Element Analysis (FEA)

Structural Health Monitoring (SHM)

Vibrating Wire Strain Gauge (VWSG)

Electrical Resistance Sensors (ERS)

Degrees Of Freedom (DOF)

Nano/Microelectromechanical Systems (N/MEMS)

Vocabulary of Metrology (VIM)

Quad Small Slotted Sensor (QSSS)

Linear Variable Differential Transducer (LVDT)

Polylactic Acid (PLA)

Coefficient of Thermal Expansion (CTE)

List of Figures

Figure 1: Effect of thermal errors on a milling machine (a) Deformation due to internal heat sources, (b) deformation due to external heat sources [5] 12
Figure 2: Sources of thermal errors in a machine tool 13
Figure 3: Concept of on-machine tool measurement 19
Figure 4: Thermal Influence on a Machine Tool Structure Using FEM (a) Machine tool ram fixed at one end (b) Ram fixed at opposite end 25
Figure 5: (a) Cross section of photomicrosensor showing emitter, detector, and an object in the optical path (b) Circuit schematic of photomicrosensor 34
Figure 6: LED Forward Current vs Forward Voltage Characteristics [67] 35
Figure 7: Dark Current vs Environmental Temperature Plot [68] 36
Figure 8: Basic photomicrosensor signal conditioning circuitry [67] 37
Figure 9: Kingbright KRB021 Engineering data [67] 38
Figure 10: Cross section of single sensor and shutter [48] 48
Figure 11: Shutter and SPM implementation for differential measurement 49
Figure 12: Description of SPM sensor 50
Figure 13: Component parts of sensor housing (a) sensor base (stationary part), (b) shutter holder, (c) main axial flexure 52
Figure 14: Mesh properties from FEA evaluation of flexure static stiffness 53
Figure 15: Static Test on Self Aligning Quad SSS to determine the stiffness of the flexure on the application of 1 N force 54
Figure 16: Multi sensor setup to measure the strain on a structure using the SPM sensors and carbon fiber connecting rods 56
Figure 17: Multi sensor setup - strain measurement 57
Figure 18: Shutter displacement on left sensor 59
Figure 19: Dual sensor with short CFRP rod 61
Figure 20: Preliminary bench testing sensor housing 63
Figure 21: Rectilinear strain sensing frame 64
Figure 22: Rectilinear strain sensing frame with interferometer 65
Figure 23: LabView visualization software for strain framework setup 66
Figure 24: Thermal image of localised heating of the top bar of the test rig 67
Figure 25: Laser and SPM framework comparison 68
Figure 26: Strain measurement framework thermal test result 69
Figure 27: Comparison of SPM and Interferometer 70
Figure 28: Results for heating of top bar 71
Figure 29: Correlation Analysis of SPM and Interferometer 72
Figure 30: Linear Relationship between interferometer and SPM sensor 73
Figure 31: Measurement procedure with SPM displacement sensor 76
Figure 32: Cause-and effect diagram for SPM sensor 76
Figure 33: Schematic of setup for sensor calibration 77
Figure 35: Schematic of setup for voltage Self-calibration technique 77
Figure 35: Voltage Self-Calibration Setup 78
Figure 36: Close-up of setup showing attachment of laser optics to SPM sensor 78
Figure 37: Piezo calibration 81
Figure 38: Calibrated Piezo Controller 82
Figure 39: Method to compute uncertainties based on GUM [92] 83
Figure 40: Plot of actual position versus output voltage of a displacement sensor 85
Figure 41: Linearity Error 86
Figure 42: Variation in ambient light conditions; (a) with the lights OFF (b) with the lights ON 89
Figure 43: Single SPM sensor stability test 91

Figure 44: Measuring Circuit for investigating effect of changing limiting resistor 93
Figure 45: Effect of Abbe Error on SPM displacement measurement.....94
Figure 46: Effect of Cosine Error.....95
Figure 47: Uncertainty budget for measurement system 97
Figure 48: Relationship between distance, displacement and related parameters [51].....99
Figure 49: Insensitivity of sensor head to variation in power supply (a) Differential voltage between SPM 1 and SPM 2 (b) Differential voltage between SPM 3 and SPM 4 (c) Average of (a) and (b) [48] 102
Figure 50: Flowchart for voltage calibration technique 105
Figure 51: Relationship between light variation and shutter movement.....107
Figure 52: Comparison of sensors for a Good Setup 108
Figure 53: Comparison of sensors for a Bad Setup.....109
Figure 54: Graph for Good Setup and Bad Setup 109
Figure 55: Shutter Misalignment.....111
Figure 56: Differential voltage principle implementation on self-calibration technique for good setup (a) Good setup (b) Difference in voltage (DV1) between sensor S1 and S2, (c) Difference in voltage (DV2) between sensor S3 and S4, (d) Average of DV1 and DV2 112
Figure 57: Differential voltage schema implementation on voltage self-calibration for bad setup (a) Bad setup (b) Difference in voltage (DV1) between sensor S1 and S2, (c) Difference in voltage (DV2) between sensor S3 and S4, (d) Average of DV1 and DV2.....113
Figure 58: Plot showing the sensitivities for a misaligned sensor with shutter at nominal position, then displaced by 0.9 µm and 1.8 µm. 115
Figure 59: Correction procedure for an adjusted sensor 116
Figure 60: SPM final output (a) without compensation, (b) and (c) with compensation.....117
Figure 61: Fused deposition modelling 3DP process of a face shield. 3DP, three-dimensional printing.....122
Figure 62: Component of sensor housing (a) Sensor Base (static part) (b) Shutters and shutter holder (movable part) 124
Figure 63: Shutter adjustment mechanism 126
Figure 64: Resultant shutter movement after adjustment (a) Bottom of shutter holder showing the adjusted shutters (b) Top of shutter holder [112] 126
Figure 65: Stiffness Study on Self Aligning Quad SSS 127
Figure 66: Triple sensor setup overview - improved design.....129
Figure 67: Triple sensor setup overview - strain applied to structure.....130
Figure 68: Triple sensor setup overview - strain applied to structure.....130
Figure 69: Strain on middle sensor 132
Figure 70: Setup for 3D printed sensor design validation test 134
Figure 71: Calibration setup for 3D printed sensor design 135
Figure 72: Calibration curve 137
Figure 73: Residuals vs calculated strain plot.....137
Figure 74: Characteristic curve for bidirectional test.....138
Figure 75: Characteristic curve with magnification removed.....138

List of Tables

Table 1: Table of Ultra Stable Materials 16
Table 2: Working parameters of KRB021 Photomicrosensor 38
Table 3: Summary of displacement sensor performance characteristics 42
Table 4: Material Properties used in the FEA evaluation of the axial flexure static stiffness 53
Table 5: Table showing movement of shutters on the application of 1 N force 55
Table 6: Expansion of structure 58
Table 7: Static displacement results for multi sensor setup showing measurement of each sensor module 60
Table 8: Renishaw ML 10 Specification 79
Table 9: Uncertainty of shutter misalignment 92
Table 10: Data obtained for second voltage calibration method 114
Table 11: Cost analysis of SPM sensor housing 121
Table 12: Movement of shutters on the application of 1 N force 128
Table 13: Result for expansion of structure under test 131
Table 14: Static displacement on triple sensor setup 133
Table 15: Calculated strain and sensor output voltages for different loads 136

Chapter 1 – Introduction

Accurate measurements are of great import in the fields of science and engineering. This importance was first realized as far back as 1847 and since then, especially from the later part of the twenty-first century most manufacturing industries began to rely on precision measurements.

Recently, there is an increasing challenge for robust and accurate measurement infrastructures to meet the tighter tolerances and complex geometry of products. The information obtained from dimensional measurements is essential to support the manufacturing of components that adhere strictly with functional requirements and design specifications. The life cycle of a product is supported by accurate and precise dimensional measurements and accompanying techniques and a simple error in measurement can result in severe costs [1].

Machine tools and advanced manufacturing machinery are crucial to the operations of the manufacturing industry and have evolved from machines that were manually operated to the current computer numerically controlled (CNC) machines. Machine tools have been used in the manufacture of a wide range of products to relatively high levels of accuracy. However, their accuracy is hampered by error sources thus affecting the dimensional accuracy of produced parts. The principal sources of machine tool errors can be generally classified into three major groups which are geometric and kinematic errors, cutting force induced errors and thermal errors[2]

Geometric errors occur as a result of flaws in the design and inaccuracies during assembly. These errors are related to the quasi-static accuracy of moving surfaces and elements of a machine tool. Surface roughness and surface straightness influence the nature of these errors, which can be systemic or random. They include elements such as squareness error, straightness error, backlash error, and so on.

Kinematic errors, on the other hand, are errors that arise when multiple components of a machine tool shift relative to one another. When considering the combined motion of the various machine tool axes, they are especially noteworthy. A 3-axis machine tool is known to have 21 geometric error components [3].

Cutting force errors are the major source of error in metal-cutting machines because the force involved in the cutting operation is substantial. It results in dynamic stiffness of the components of a machine tool that are within the force-flux flow of the machine. The tool tip position with respect to the workpiece changes as a result of the distortion of the various components of the machine. As a result, a heavy cut will create more inaccuracies than a light cut.

Thermal errors have been identified as a major cause of workpiece inaccuracies accounting for almost 70% of the positioning errors in machine tools [2, 4]. These errors are the result of thermal distortions that occur on the elements of a machine due to changes in temperature.
There are three (3) sources of thermal errors in machine tools. These include.

- Heat sources that exist internally e.g., motors, ball screws, bearings, movement of guideways, etc.
- Environmental temperature variations
- Heat from external sources e.g., sunlight

The effect of these heat sources on structural components of precision machinery is as shown in Figure 1.

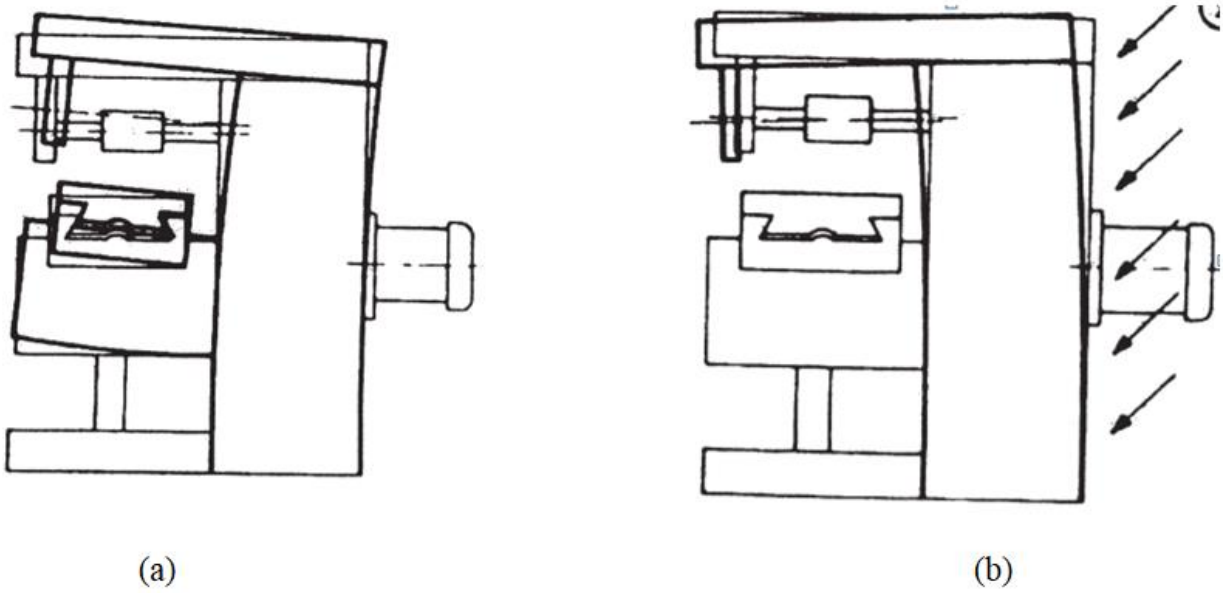

Figure 1: Effect of thermal errors on a milling machine (a) Deformation due to internal heat sources, (b) deformation due to external heat sources [5]

The influence of thermal errors on the accuracy of machine tools is receiving significant attention in recent times [6-9]. This is because it is not only important to achieve quality machining, but also to maintain the properties of machined parts under various disturbances. The various heat sources that affect a machine tool can have diverse underlying effects and causations.
The internal sources of heat include those sources of heat that directly conduct heat into the structure of the machine. These sources originate within the machine tool and fuels faster and higher temperature increases in the machine tool. However, these usually have a local affect [10].

External sources of heat are those attributed to the environmental conditions such as heat from other machines, lighting, and change in environmental temperature, in which the machine is situated. The challenge of maintaining a stable thermal environment is a complex problem due to the complex arrangement of the shop floor and the associated cost. However, studies have used integrated models which consider the various sources of heat to compensate errors in machine tool [8, 11].

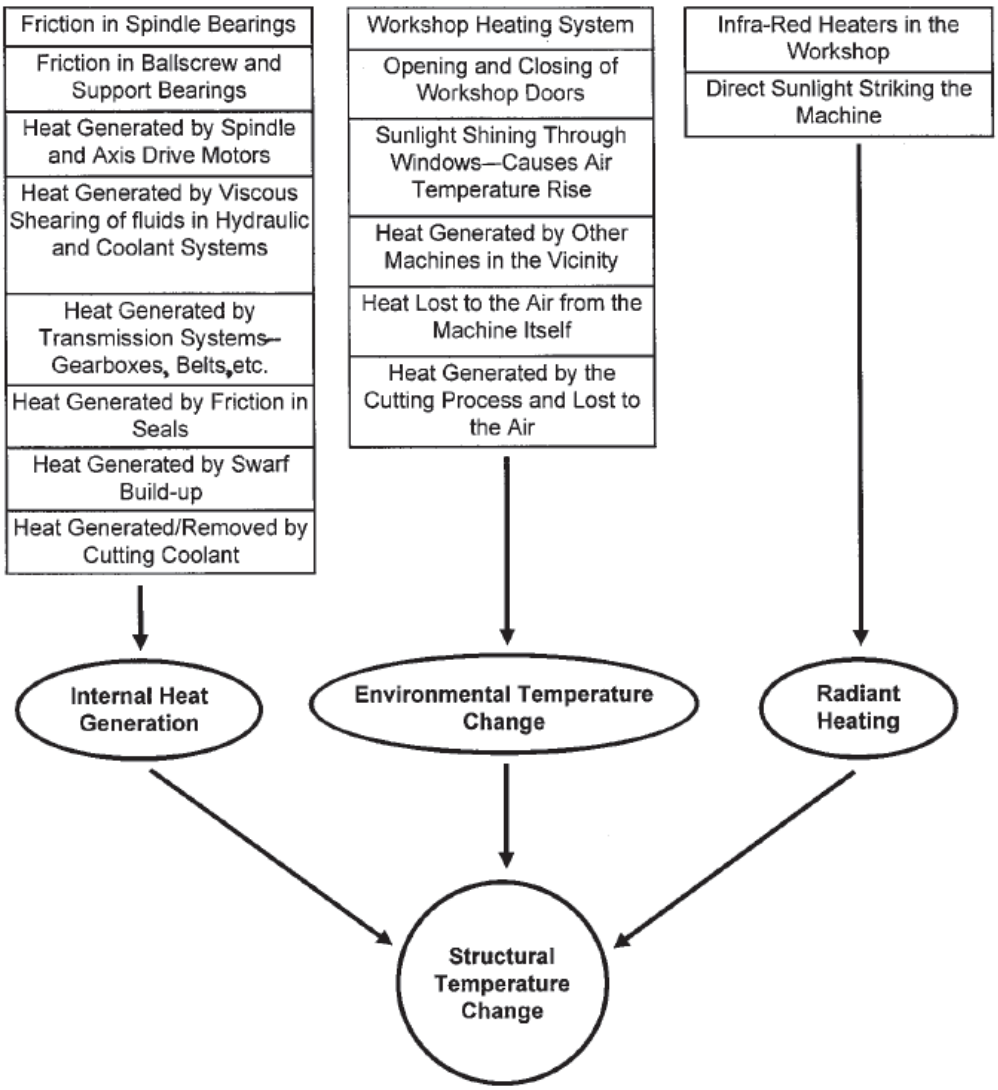

Figure 2: Sources of thermal errors in a machine tool

The subject of errors in a machine tool has generated attention and extensive research is ongoing to better understand the various sources, their effect and ways of avoiding or mitigating their effects. Prior to the implementation of CNC machines for automated manufacturing, operators with a wealth of expertise devised techniques for addressing thermal problems. With the introduction of CNC machines, manufacturing has shifted away from relying on the skills of operators to manufacture high-quality products. These machines have a range of benefits, including improved consistency,

productivity, and efficiency, as well as shorter and more consistent time periods. As a result, production costs are decreased as scrap and rework of produced parts are reduced.

Thermal distortions are caused by the multidimensional configuration of a machine tool and the temperature variance of device components, which are difficult to calculate or predict. This contributes to a wide variety of thermal error variations.

Because of the complexity of the thermal error problem, a number of techniques to eliminate or minimise its effects have been developed. For example, at the early stages of design, numerical techniques are used to model thermal effects of machine tools such that the origins of tool center point (TCP) displacements caused by heat can be identified. The results of steady state simulations are frequently relied on as against transient simulations because of the computation cost of the latter [6]. However, steady state results do not reveal the time-dependent behaviour preceding the steady state scenario, which can span several hours. The direction of TCP displacement can change during operation if the temperature field expands out from a heat source and becomes uniform after being driven by steep gradients. Such changes can be captured by transient simulations [12].

The following section discusses how thermal and finite stiffness effects are currently managed.

1.2. Machine Tool Error Reduction Techniques

Machine tools with the ability to reliably manufacture highly accurate parts are in demand. The errors in a machine tool are continuously changing because the cutting force and thermal state of the machine are also constantly changing. Because of the relative displacement between the tool tip and the workpiece during machining, defects in a machine tool affect the dimensional accuracy of machined parts. This makes it difficult to accurately determine or account for these errors. Many strategies exist for minimising errors in machine tools that result in accuracies, and they can be divided into two (2) categories: ‘error avoidance’ or ‘error elimination,’ and ‘error compensation’.

Elimination or error avoidance techniques are those strategies that seek to prevent or avoid the errors in a machine tool. Examples of the techniques employed in industries include using ultra stable materials in the machine design, etc. In most cases, these strategies are implemented during the machine's design stage, and they require end-users to follow good operating practices such as warming up and controlling the temperature of the environment.

Compensation techniques, on the other hand, use electronic or numerical methods to correct machine tool errors. They are more beneficial than error prevention strategies in general since they can be used at any point of the machine tool's life cycle other than just during the design and development phase.

1.2.1. Error Avoidance Methods

Error avoidance strategies are those that use deliberate efforts during the design or manufacturing stages to remove or minimise errors in a machine tool. It requires improvements to the machine tool's architecture as well as the use of low-coefficient-of-thermal-expansion materials. One obvious way of minimising the temperature change of the system is to minimise the internally produced heat in the machine tool structure.

A number of design improvements have been documented in [13] that have resulted in a major reduction in the heat produced in machine tools. Some of these involve putting heat sources outside of the machine's main structure, using electrical servo drives instead of hydraulic servo drives, regulating the machining environment's temperature, thermal error avoidance using chiller systems to remove excess heat, etc. Although these methods are effective, they are expensive and only applicable to local cooling of bearings and motors and not really the whole machine.

Thermal deformation of a machine tool can also be reduced by using a material with a low thermal expansion coefficient for (parts of) the machine. Sections of the structure of coordinate measurement machines (CMMs) have been constructed from materials such as carbon fibres or Zerodur, which have extremely low coefficient of thermal expansion [14]. With advancements in materials science, more applications incorporating these materials will emerge.
Temperature has an impact on the geometry of the workpiece and the measuring equipment, so it must be adequately reduced or compensated for. To design a suitable and traceable error compensation scheme, it is necessary, among other things, to have a good understanding of the thermal expansion coefficient of the machine tool components and the components of the measuring system. This would encourage the development of more precise measurement strategies and devices, resulting in fewer uncertainties in temperature and displacement measurements [6].

Table 1: Table of Ultra Stable Materials

TABLE OF MATERIALS AND THEIR PROPERTIES						
MATERIAL	PROPERTIES					
	Conductivity [W/(m.K)]	CTE	Chemical Stability	Availability	Machinability	Cost
Zerodur	1.46	0.05 ± 0.10e-6/K (20°C to 100°C)	Very high	Readily available	Easily machinable using diamond tools	Relatively cheap and affordable ($15 - $40)/Kg
ULE	1.31	E-8/K (5°C to 35°C)	High	Readily available in bulk; high availability	Can be machined using a diamond grinding process	High cost ($750) 1 - 99 Kg
Invar	12 (min) – 15 (max)	Less than 1.3e-6/°C	Very high	Readily available	Difficult to machine in the annealed condition	Relatively cheap and affordable ($20 - $30)/Kg
Super Invar	0.1	0.35E-6/°F	Very high	Readily available	Difficult to machine in the annealed condition	Relatively cheap and affordable ($20 - $30)/Kg
Clearceram-Z	CCZ Reg: 1.51 CCZ HS: 1.52	For 0°C to 50°C: CCZ Reg: 0.0 ± 1.0e-7/°C CCZ HS: 0.0 ± 0.2e-7/°C	Very high	Readily available	Easily machinable using diamond tools	High cost ($600 - $750) / Kg

Carbon fibre reinforced plastics (CFRP)-structures were employed in [15] to develop a system for reducing core spindle casing angular displacements due to thermal effects by heating the unidirectional carbon fibre reinforced laminate. Compensation of displacements was achieved using an adaptronic system that took into account the negative thermal expansion of CFRP-structures.

Merlo et al [16], discussed applications of alternative materials (for example CFRP) as a solution for the design of light structures for high-performance machine tools.

While a comprehensive design of a machine using advanced techniques can improve its performance and reduce thermal distortions, the accuracy that can be achieved is limited. These methods do not completely eliminate the effects of thermal errors because they do not account for the distortion caused by thermal effects on the shop floor or deformation caused by cutting force. Also, implementing new materials and improved design methods can be costly and difficult in existing machines.

1.2.2. Error Compensation Methods

Compensation approaches have found a broader application in reducing thermal effects, as an error reduction system is supposed to be more cost-effective [17]. Increasingly, thermal error compensation is being used to correct for errors, typically using temperature measurement of various parts of the machine. For example, a novel approach was proposed in [18] that explores thermo-mechanical errors using Fibre Bragg Grating (FBG) sensors embedded in the MT frame and uses compensation-based techniques to standardise a machine tool in real-time. The research compared the numerical model developed with experimental tests using FBG sensors. The proposed design consists of an adaptronic assembly of inert materials, Carbon Fiber Reinforced Polymers (CFRP), fitted with smart sensors (e.g., FBG sensors). Finite Element (FE) simulations were used to construct a model to explain the stresses in the machine tool structure. Despite the fact that experimental results indicate improved error prediction, the model's accuracy is influenced by the number and location of sensors.

Also, the results of a thermal sensitivity study on a turning centre were reported in [19]. The effect of temperature changes in machine elements on thermal deformation of the turning centre was defined using a transfer function. This approach is said to solve the problem of estimating this contribution using the finite element method. Temperature sensors were mounted on the machine tool and the convolutional neural network (CNN) was used to build a model that provided good prediction output for thermal displacement compensation based on the acquired temperature data.

Furthermore, [16] mounted five (5) FBG sensors in a ram (Z-axis) structure of a milling machine made of CFRP to test the axial elongation of the structure. Multiple Regression Analysis was used to estimate the tool tip's drift (MRA). The reported results revealed a residual drift error reduction of about ±10µmThese techniques do not avoid the errors. Rather, the errors are studied, measured and compensated for. Compensation is the method of correcting thermal errors by changing the tool and component locations to offset the errors being compensated. Error compensation is gaining popularity because it incorporates low cost, high accuracy, and high production volume, both of which are attractive qualities in today's industries. Increasingly, thermal error compensation is being used to correct for errors, typically using temperature measurement of various parts of the machine.

There are two types of error compensation methods (2). There are examples of "pre-calibrated error compensation," in which the error is calculated before or during a machining operation and then used to calibrate subsequent processes. On the other hand, ‘active error compensation' involves measuring the error during a machining routine and using the knowledge of the machining operation to adjust the process during the same operation.

The cumulative impact of the different error sources in a machine tool contributes to its accuracy, and the error compensation scheme should take into account the interaction of these sources rather than

their individual effects. As a consequence, error compensation is concerned with the effect of these error factors on the accuracy of a machine tool [2], rather than the absolute value of errors. To do so, the errors must be continually monitored because they change over time as the machine tools are subjected to constantly changing operating conditions [20].

An understanding of the possible causes and estimates of machine tool errors necessitates calibration. It characterises the machine's output and offers a means of detecting accuracy issues [21]. Machine tool calibration may be achieved with specialised equipment, but it often necessitates professional expertise and is time consuming, thus increasing the overall cost. This outweighs the advantages of the process [22].

Although pre-calibrated error compensation may provide a reasonably easy and repeatable mapping of machine tool geometric errors, correctly mapping thermal errors, which are based on factors like environmental conditions and machining effects, is more difficult. This restriction can be solved with active error compensation, resulting in a more suitable solution for engineering applications. However, there are additional costs associated with implementing this solution [23]. On-machine measurement, which incorporates on-line measurement, using a touch probe into manufacturing processes, is a readily available alternative [22]. A touch probe is an accessory that is mounted on the spindle of a CNC machine for quality inspection of parts during or after manufacture [24]. The advantages and problems of this kind of arrangement are highlighted in Section 1.3.

1.3. On-Machine Measurement

Process adjustment and production management activities must become more effective as demand for manufactured parts fluctuate and tolerance and accuracy standards tighten. These issues are addressed by incorporating measurement into the production process, and the method is adaptable for measurement or manufacturing processes [25]. On-machine measurements are used for simple workpiece configuration, in-process measurements for versatile manufacturing, and post-process measurements for product validation, resulting in a fully functional manufacturing system. From setup to final metrological validation of the manufactured component, dimensional measurements can be used at various stages of the development cycle. Figure 3 illustrates the basic principle of on-machine tool calculation.

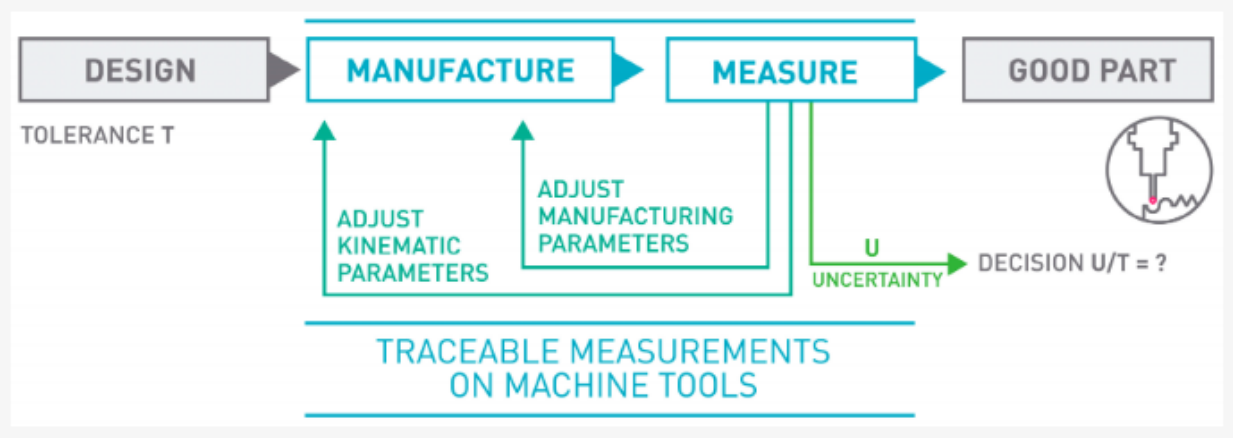

Figure 3: Concept of on-machine tool measurement

By incorporating the probe into the machine tool, in-process measurement allows for tracking of the output of a machine while it is in operation. The geometry of a machine can change during operation for a variety of reasons. In-process measurement techniques allow for the tracking and adjustments in machine geometry to prevent scrap and rework, as well as maintenance scheduling [26]. Also, during the machining operation, metrological measurements of a produced component on the system can be performed to provide correction values based on deviations from target measurements. By feeding calculated data back to the system controller, this allows for a more flexible manufacturing process. The physical limitations of this technique, as well as the added expense of integrating the measurement procedure, are its disadvantages [23].

Inspection of parts on standalone measurement devices, such as coordinate measuring machines (CMM) in a controlled environment, is part of the post-process measurement process. This necessitates the transfer of the component from the manufacturing to the inspection areas, causing delays and increasing the overall manufacturing cost. In addition, if the part fails the test, it must be scraped or reworked [27].

Despite the obvious advantages provided by on-machine touch probing for reducing and compensating machine tool errors, there are disadvantages which limit its application. One disadvantage is the lack of traceability of a machine tool. Since both the manufacturing and monitoring operations are done on the same machine, the error due to the geometry of the part will be observed by both processes. Hence, the geometric error of manufactured part cannot be observed except if the machine tool has been characterized for geometric errors before the measurement process [28].

In addition, the repeatability of the machine tool is undermined by changing environmental conditions on industrial shop floors. Furthermore, these systems can have significant residual errors due to hysteresis between distortion and surface temperature readings. Compensation systems rely on

complex models (sometimes grey or black box methods) and data from sensors which are not regularly calibrated therefore the ongoing uncertainty and traceability could be affected.

1.4. Motivation

A major engineering challenge is incorporating the measurement and inspection process into the machine tool. These processes can be done by touch probe systems on the most recent machines. However, since the procedure is not traceable, data from such measurement and inspection procedures cannot be used for process control. Interferences such as ambient temperature instabilities and design flaws are to blame. Thermal error avoidance techniques e.g. using chiller systems to remove excess heat are effective but expensive and are only applicable to local cooling of bearings and motors and not really the whole machine. Increasingly, thermal error compensation is being used to correct for errors, typically using temperature measurement of various parts of the machine. However, these systems can have significant residual errors due to hysteresis between distortion and surface temperature readings. Also, compensation systems rely on complex models (sometimes grey or black box methods) and data from sensors which are not regularly calibrated therefore the ongoing uncertainty and traceability could be affected.

Temperature-based error compensation can achieve better results if the bending of the structure can be measured directly using a strain sensor for example. FBGs have been employed as a strain sensor for monitoring structural deformation, but they are very expensive and have relatively low resolution and are subjected to temperature effects. Thus there is a need for a more cost effective, high resolution and low uncertainty solution.

The purpose of this study is to develop a novel displacement sensor, and using a comprehensive uncertainty evaluation together with in-situ calibration techniques, build a remote mechatronic device that can provide high-accuracy displacement measurements with long-term stability suitable for long term embedded structural monitoring.

1.5. Aims and Objectives

1.5.1. Aim

The aim of this research project is to design and create a sensor with reduced uncertainty suitable to be embedded for structural deformation monitoring in precision machinery such as CNC machine tools, cast iron and steel structures.

1.5.2. Objectives

The target has been broken down into the following detailed work packages in order to effectively complete this research work. These include;

- To create a displacement sensor that uses a novel arrangement of low-cost photomicrosensors.
- To identify the sources of uncertainties in a newly developed displacement sensor.
- To evaluate ultra-stable materials for use as reference standards.
- To investigate a method for reducing uncertainty through in-situ calibration
- To reduce the uncertainties in a newly developed structural deformation system by using an improved sensor design that reduces manufacturing cost.
- To design a framework that can enable strain measurement over different structural sizes

1.6. Novelties and Contributions to Knowledge

The contribution of this research work to knowledge is outlined as follows.

- The design and analysis of a new displacement sensor that uses very low-cost slotted photomicrosensors (SPM) and works on a differential voltage sensing technique.
- The development of a rectilinear framework for measuring structural distortion using the new displacement sensor design and suitable connecting rods.
- Investigation of the sources of uncertainty for a system that uses the newly developed SPM sensors and suitable connecting rods, and the creation of an uncertainty budget.
- Development of a new voltage self-calibration method to reduce the uncertainties associated with the SPM sensor in-situ. This is important especially for embedded applications where it is difficult or costly to remove the sensors for calibration. This technique was shown to reduce the errors on the sensor by 60%.
- Investigation and development of a 3D printable design of the sensor to improve the performance and reduce the manufacturing cost of the sensor. A new flexure design reduced compression/tension losses in the connection rod and reduced misalignment during installation.

1.7. List of Published Papers

1. Fletcher Simon, Chuku Difference., Furness Thomas, Longstaff Andrew, Design of a structural strain measurement system based on slotted photomicrosensors, in *14th International Conference and Exhibition on Laser Metrology, Coordinate Measuring Machine and Machine Tool Performance*. March 11, 2021, Euspen

   50% contribution to the published paper including providing support to the new design idea and experimental design, performing testing and data analysis.

1.8. Summary

In today's manufacturing industries, such as energy and transportation, losses during the production phase of high-value components are no longer appropriate. Complex and accurate components are needed in industries such as aerospace, automotive, shipbuilding, nuclear power, large research facilities, and wind power, which require close measurements and rapid input into their manufacturing processes. Despite the fact that current instrumentation allows for accurate calculation of deviation from precise geometry, easier, less costly methods are preferred.

New measurement technologies, such as integrated touch probes and fast interface capabilities, are now available in machine tools. They allow in-machine measurement of the workpiece during or after its manufacture, preserving the workpiece's original setup and preventing the manufacturing process from being disturbed by transporting the workpiece to a measuring location.
However, the traceability of the measurement process on a machine tool has yet to be developed, and measurement data is inadequate for process control and product validation. The scientific aim is to evaluate the degree of uncertainty in a machine tool measurement and, as a result, turn it into a machine-integrated traceable measuring procedure. An error budget should take into account error sources such as machine tools, components under evaluation, and their interactions for this reason.

Machine tool positioning errors have an immediate impact on the dimensional accuracy of manufactured items. Kinematic errors, geometric errors, thermal errors are common error sources. The control of thermally generated machine tool errors is undergoing substantial developments in the manufacturing industry. Many techniques have been investigated based on temperature based error compensation. However, research has shown that better results can be achieved through direct measurement of structural distortion using a strain sensor for example. Fiber-optic based sensors for example FBGs are being used extensively because of their several advantages. However, they are very

expensive, had relatively low resolution, and are susceptible to temperature effects. Hence, a more cost-effective solution with high resolution and low uncertainty is required.

Chapter 2 - Literature Review

A major aim of manufacturing engineering research is to integrate a traceable measurement technique into the machine tool. It ensures that quality inspection on the machine tool is traceable before, during, and after the machining process, lowers manufacturing costs, and provides high throughput and zero-defect manufacturing processes [29].

Performing a traceable measurement procedure on a machine tool is currently not assured, making measurement outcomes untrustworthy for an adaptive manufacturing process. On-machine tool measurement is a solution, but it is complicated by various sources of uncertainty related to shop floor conditions. These include temperature variations, machine tool geometric error, probing method, dirt, and vibrations. These sources of uncertainty are still unclear, leading to a lack of a traceable metrological chain, which makes the manufacturing process unreliable.
It is crucial to examine the measurement uncertainty caused by on-machine measurements in order to address the challenge of inaccurate manufacturing processes due to a lack of a traceable metrological chain. This can be achieved by defining all sources of uncertainty, quantifying their effects, and including them in the on-machine measurement uncertainty evaluation.

2.1. Sources of Uncertainty in On-Machine Measurement

The uncertainty assessment for on-machine metrology should comprise four (4) main error sources – the machine tool, the touch probe system, component under test (workpiece) and the environmental conditions.

2.1.1. Machine tool

Errors in a machine tool are caused by defects in the design, mechanical misalignments, and deformations in the machine's structure. These errors can be classified into two categories: random errors and systematic errors. Random errors are difficult to predict while systematic errors are easy to calculate and compensate for [30]. The major error sources associated with a machine tool to be thus considered are repeatability, geometric errors and thermal errors.

2.1.2. Environment

Changing ambient temperatures are one of the most common unstable conditions observed in industrial environments. Environmental temperatures, in particular, have been established as a major source of machine tool errors by researchers. [6, 31]. Figure *4*, obtained from a confidential technical report,

shows the finite element simulation of the effect of changing environmental conditions on the ram of a machine tool.

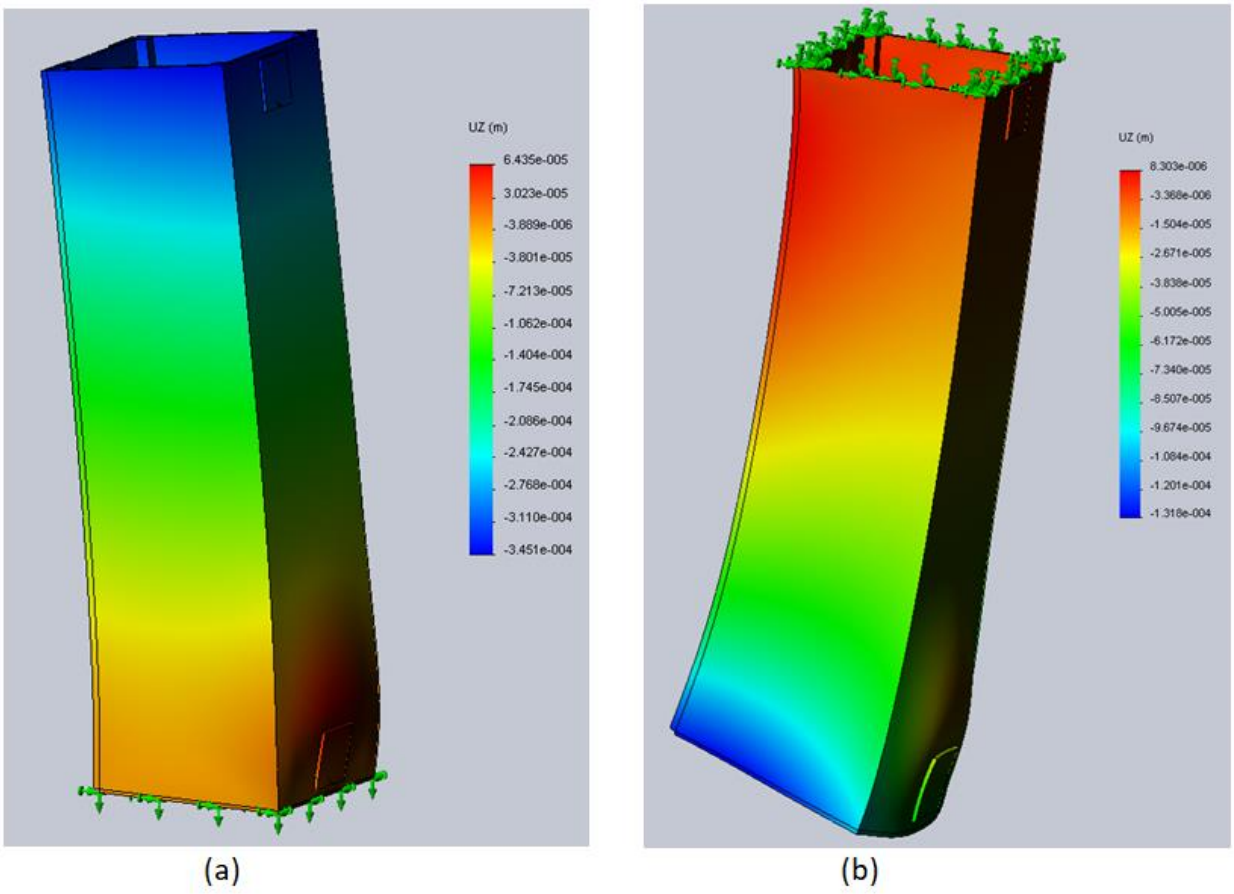

Figure 4: Thermal Influence on a Machine Tool Structure Using FEM (a) Machine tool ram fixed at one end (b) Ram fixed at opposite end

2.2. Structural Deformation Monitoring

Structural deformations are one of the most critical causes of errors in most engineering systems. Although these deformations are complex and difficult to be modelled, they must be evaluated to guarantee integrity and safety of these structures. Usually, this is achieved by numerical and analytical analysis because of the high cost and complexity of performing full-scale experiments on these systems. However, the use of unconventional composite materials and new manufacturing technologies has increased the demand for effective experimental methods to assist analytical and numerical assessments [32]. Structural health monitoring provides a solution that assesses and monitors the condition of essential structures. The measurement of displacement, deformation, and other physical parameters is necessary for monitoring the health of engineering systems. As a result, a

variety of sensing technologies have been used in structural monitoring applications many of which rely on strain measurements [33]. Several scientific studies have demonstrated that proper structural monitoring implementation can have a massive influence on a structure's life-cycle cost, resulting in a favourable cost/benefit ratio. A review of the new developments in strain measurement techniques is presented in the following section.

2.2.1. Review of Strain Measurement Sensors

Strain is the amount of deformation that a body undergoes as a result of an applied force [34]. It is the ratio of the change in length per unit length of a material in response to an applied stress. Strain may be either negative or positive, depending on whether it is caused by contraction (compressive) or elongation (extensive) (tensile). Strain is a non-dimensional quantity that is commonly measured in inches per inch (in./in) or millimetres per millimetre (mm/mm). The magnitude of the strain measured in real applications is very small, mostly limited to about 10^{-3}, hence it is commonly expressed in microstrain (μstrain) [34].

For small strain approximation, u, v, and w being the components of displacement along x, y, and z directions, then the six components of strain can be evaluated as:

$$\varepsilon_x = \frac{\partial u}{\partial x}, \varepsilon_y = \frac{\partial v}{\partial y}, \varepsilon_x = \frac{\partial w}{\partial z}, \gamma_{xy} = \frac{\partial v}{\partial x} + \frac{\partial u}{\partial y}, \gamma_{yz} = \frac{\partial w}{\partial y} + \frac{\partial v}{\partial z}, \gamma_{xy} = \frac{\partial w}{\partial x} + \frac{\partial u}{\partial z}$$

Measurements of strain are typically done on the free surfaces of bodies hence the determination of only three components of the strain tensor, ε_x, ε_y, γ_{xy} is sufficient for experimental analysis of stress[35].

Strain is a non-uniform point feature in general, but current sensing systems are unable to quantify strain at a single point. Typically, the strain is measured as an average over a finite length or within a finite field. The differential displacement-strain equation is approximated using the following formula:

$$\varepsilon_x = \frac{\partial u}{\partial x} \cong \frac{\Delta u}{\Delta x} = \frac{\ell_x - \ell_{x_o}}{\ell_{x_o}}, \varepsilon_y = \frac{\partial v}{\partial y} \cong \frac{\Delta v}{\Delta y} = \frac{\ell_y - \ell_{y_o}}{\ell_{y_o}}$$

where ℓ_{x_o} defines the original length under no-load, and ℓ_x is the final length of the unit under test in the x-direction with the application of force. As a result, most strain measurement techniques are focused on calculating the length shift of an initial length.

Researchers have studied many sensors for the measurement of strain. C. Wheatstone claimed in 1843 that mechanical stress changes the resistance of a wire. After 80 years, E.E. Simmons (at CALTEC)

and A.C. Ruge (at MIT) created the first strain gauges based on this effect. A stress and strain measurement device were created by attaching the measuring wire to a carrier material. The metal strain gauge works as a bonded sensor and is the most common method of strain measurement. Mechanical strain sensors were the first strain sensors, and they detected strain by comparing the measured change in length to the object's original length. However, these devices were bulky, difficult to use and had low resolutions. Also, a mechanical strain gauge's relative change in resistance (gauge factor) is equal to twice the strain, which is much too poor for practical applications.

The resistive strain gauge is a physically simple device that can be used to make simple surface deformation measurements. Only the deformations of the surface to which the sensor is connected will cause the resistance of an ideal strain sensor to change. In practical applications, resistive strain sensors have a higher sensitivity than capacitive strain sensors [36, 37]. They are, however, hysteresis-affected, have non-linear behavior, and have a weak response to dynamic strains [37]. The thin-film strain gauge and diffused semiconductor strain gauges were developed to eliminate the requirement for adhesive bonding. As a result, the installation will be more reliable, and errors caused by sensor drift and hysteresis will be reduced.

Semiconductor strain gauges are more sensitive and have a higher resistance than other strain gauge varieties. They are much more compact and less expensive, and their gauge factor can be practically 60 times higher [38] than metallic foil sensors. These devices use the piezoresistive effect of silicon or germanium to calculate the change in resistance with stress rather than strain. They have no hysteresis or creep, making them ideal for long-term installations. However, they have a greater propensity to drift and are more vulnerable to temperature effects as compared to metallic foil sensors. A temperature compensation circuitry could be used as a potential mitigation [39] but this increases the complexity and cost of the solution. They also have a nonlinear relationship between resistance and strain.

Capacitive-type strain sensors operate on the capacitive concept. They overcome the limitations of the resistive strain gauges for practical applications. Capacitive sensors have better noise density, higher linearity, and faster response time than resistive strain sensors[40], and have also been shown to be extremely repeatable [41]. However, their sensitivity to surface irregularities, complexity of their circuit and requirements for mounting has restricted their use. Also, they are limited by low sensitivity caused by the structure of the parallel plate [37, 42].

In many applications, it is necessary to detect the strain in many locations of a structure without compromising its structural integrity. Using strain gauges in such applications would result in a dense system of sensors with a significant number of electric wires, which would increase the size of the setup [32].

From this standpoint, optical sensors are one of the structural monitoring alternatives to strain gauge-based sensors. Optical sensors detect strain by using interference fringes created by optical flats. They have been used in a variety of applications. They have good sensitivity and accuracy, but they are fragile, making them unsuitable for industrial applications. Optical sensors are ideally suited for use in a laboratory environment. The photoelectric gauge generates an electrical current proportional to strain using a light beam, two fine gratings, and a photocell detector. Their gauge length can be as short as 15mm, but they are costly and difficult to work with.

Fiber-optic sensors have inherent advantages over traditional sensors, hence are finding more applications. They can be incorporated into structural composite materials due to their small size and high mechanical strength. For strain measurements, many fibre strain probe manufacturing techniques based on optical/interferometric principles are available.

The authors in [43] demonstrated the efficiency of an interferometric fibre optic sensor with a light emitting diode (LED) as the light source and two (2) fibre Fabry-Perot interferometers as the temperature sensors. LED was used as the light source to minimize the disadvantages of semiconductor lasers. [44] summarized and illustrated several innovative methods for overcoming the limitations of Extrinsic Fabry-Perot interferometric sensors in measuring pressure, temperature, and vibration at the same time. In an application, a fibre in-line etalon with a self-enclosed cavity that is temperature stable was used as a low-cost temperature-insensitive wavelength reference in optical fibre communications. The working theory of a sensor device that overcomes the two (2) inherent flaws of fiber-optic Fabry–Perot strain sensors, namely, poor signal and difficult multiplexing, is addressed in [45] and in [46] a study of fiber-optic FPI sensor working concepts, fabrication processes, and sensing applications was reported. The analysis outlined the disadvantages of FPI fibre optic sensors as well as areas that need further testing, such as output reliability and prolonged service.

The key benefits of fibre-optic sensors are their light weight, compact size, passive nature, and immunity to electromagnetic interference (EMI). They also use little power and cause little attenuation, and they have great sensitivity, a wide bandwidth, and are resistant to the environmental conditions. Their main drawbacks are their high cost and limited knowledge of the end-users. Optical sensors based on Fibre Bragg Gratings (FBGs) are gaining increased attention because of several advantages: compact configuration, without the need for wiring, adaptability for non-invasive remote sensing, lightweight [47]. They retain all the advantages of fibre optic sensors and are also inherently resistant to electromagnetic interference (EMI), radio frequency interference (RFI) and can relate to data communication systems, leading to their extensive use in many sensing applications. A review of FBG strain sensors was presented in [47] where the principle of operation and the performance of different schemes were described. FBGs are extremely sensitive to a variety of environmental factors, including

physical, chemical, and biological factors, hence are employed to monitor the health of several engineering structures. However, the configurations discussed are complex and the interrogation systems are expensive, thus increasing the total cost of using FBGs. For example, the dynamic reading unit 4CH, 1000Hz, 100 nm range from SMARTEC costs about £20000 in 2022.

2.3. Review of Displacement Sensors

A review of displacement sensors is presented in this section focusing on those sensors that can detect displacement and strain. The review was included because it leads to an introduction of photomicrosensors (sensors for detecting binary presence), which have been reported to be used to create a displacement sensor in [48]. These photomicrosensors are fundamental to the application discussed in this thesis.

In nanotechnology, semiconductor technology, and biotechnology, displacement is a crucial factor. It is important to obtain accurate measurements of this variable. For measuring displacement, a variety of sensors are available. Capacitive sensors, inductive sensors, eddy current sensors, linear variable differential sensors, linear encoders, laser interferometers, and other types of sensors fall into this group.

The selection of a sensor for a given application is based on matching the sensor's operating characteristics to the particular application requirements while additional factors such as budget and impedance matching help in the final decision. Capacitive sensors, for example, have the highest resolution over short distances, are temperature tolerant, and are simple to construct, but they are constrained for general-purpose applications due to alignment errors. Eddy current sensors have very good resolutions for measurement ranges greater than 100 µm. They're much less susceptible to dust and other contaminates. They are, however, more temperature sensitive than capacitive sensors [49].

A comparison of the performance of existing displacement sensors was presented in [40]. The advantages and disadvantages of existing sensing technologies were compared for various applications. For example, the intrinsic linearity of LVDT sensors is high, and they can be shielded from magnetic interferences, but their maximum resolution is limited by their physical construction. The construction of inductive sensors is close to that of eddy current sensors. They're also resistant to contaminants and dust, but magnetic disruptions prevent them from being used for nanometer-scale applications. Sensors that can achieve long-range displacement measurements with high resolution are in higher demand. Laser interferometers and optical encoders, when compared to other sensors; provide a solution to this problem.

Laser interferometers are more accurate instruments for traceable measurements, but their price and size preclude them from being incorporated into small mechanical systems [50]. The primary competitors of interferometry are optical encoders. Invar or Zerodur gratings can achieve centimeter range and hundreds of nanometer cycles. They are, however, costly and susceptible to thermal distortion [51], as well as interference from ambient light.

Many researchers are studying methods for overcoming the limitations of the various types of sensors that are available in order to extend their industrial applications. A systematic approach for selecting the best sensor for a given application was reported in [52] where performance charts were shown to help in the selection of sensors for unique applications. The authors in [49] suggested a method for minimizing eddy current sensor thermal drift. Experiments revealed that eddy current sensors' probes can detect precise displacement and temperatures without the use of external hardware. The self-correcting eddy current sensor was used to achieve a recorded thermal drift of 2.6nm/°C. To achieve optimal results, the rate of temperature change should be less than 1°C/hr. which is difficult to achieve on the shop floor. A new displacement eddy current sensor for high-pressure applications was described in [53] and backed up by [49]. In this sensor, temperature changes induce a change in coil resistance rather than coil inductance, according to the study. A non-inductive compensating coil was used to compensate for temperature drift.

An absolute method of calibrating displacement sensors was introduced by [54]. The accuracy of displacement sensors is harmed by inherent systemic errors, such as sensor output linearity error, according to the paper. Since linearity error characteristics do not stay constant, displacement sensors must be adjusted on a regular basis to account for changes in the environment in which they are used (i.e., in-situ condition). As a consequence, these sensors must be calibrated in-situ. The linearity error and mean sensitivity of the sensor were calculated using an in-situ calibration process and the results revealed that the mean sensitivity and linearity error of a displacement sensor can be precisely calculated when used in combination with a laser interferometer. The laser interferometer was used in the experiment to calculate the laser light's displacement shift quantity.

Angular displacements were measured by using a high-resolution fiber optic sensor [55]. Two configurations of the sensor were discussed, one with a long range (± 23.4°) and another with a shorter range (±14.5°) and lower resolution. The proposed sensor's small size allows it to be embedded in compact mechanical systems. The results of the experiments and simulations for modelling ‘lens-free configuration' and ‘GRIN micro-lens configuration' were very similar, and measurement sensitivity improved by a factor of two.

Nanometre sensors are a relatively new type of sensor. They have nanometer or sub-nanometer resolution and a few nanometers of variability across a spectrum of at least many micrometers. This

group of sensors includes capacitive sensors, inductive sensors, laser interferometers, and holographic scales. The system mechanical and electronic accuracy is limited by linearity errors and drift. As a result, traceable methods for evaluating these errors are needed and can be accomplished by calibrating the sensor on a traceable instrument or using a measuring principle based solely on traceable elements. Some researchers have investigated this solution and reported results are quite promising. For example, a Fabry-Perot interferometer with nanometer accuracy was developed in [54] for the calibration of displacement sensors,. The resonant frequency of the interferometer can be determined by locking a tuneable diode laser to the Fabry-Perot cavity using frequency modulation. A beat calculation with an iodine-stabilized helium-neon laser is used to calculate the diode laser frequency. The laser diode frequency is shifted over the free spectral spectrum as the beat frequency begins to surpass the measurement range (up or down). To achieve nanometer precision, the cavity design and operating environment are of particular importance. Zerodur rods were used to reduce temperature effects and to determine cavity length. [56] identified a method for calibrating displacement sensors to nanometer precision and traceability to a primary length standard. A Fabry-Perot interferometer was used to achieve traceable measurement. A Fabry-Perot cavity is used to lock the frequency of a laser. The slave laser records the shift in cavity resonance frequency when one mirror of the Fabry-Perot interferometer is displaced. The mirror is attached to a sensor that needs to be calibrated and the frequency difference between the iodine-stabilized laser and the slave laser is calculated by a frequency counter. The frequency measurement is used to determine displacement, which is then compared to the sensor readout to provide calibration results. [57] proposed a fibre bragg grating-based optical sensor with a low finesse cavity. This configuration allows for temperature control when calculating displacement. The sensor includes an integrated fibre bragg grating that monitors local temperature and acts as a reference for any thermal insensitivity of the cavity, as well as a high-resolution Fabry-Perot cavity for displacement measurements.

A simple optical sensor with nanometre resolution and centimetre range was described in [50]. A laser-diode module and a photodiode array make up this non-contact sensor. The use of optical fibre and a normalization method allows for high repeatability and limited drifts, while the corner cube configuration makes the device insensitive to mechanical faults from the mobile platform. However, the sensor suffers from non-linearities, and the accuracy of the sensor was limited by the uncertainty in the deflection angle of the cheap corner cube mirror used in this application. Although better accuracy can be achieved by using a more expensive mirror, this increases the cost of the sensor.

A high accuracy capacitive displacement sensor for non-contact precision displacement measurement have been investigated in [58]. A high-accuracy displacement sensor was used to calculate lateral thermal deformation of the spindle, and the device consisted of a National Instrument data acquisition

board and personal computer. The effect of temperature and other environmental factors was decreased, according to the results of the experiments.

The development and performance characterisation of a novel displacement sensor was reported in [48]. The displacement sensing head was reported to use a differential technique and commercially available and low-cost infrared (IR) transmissive sensors, also known as slotted photo-microsensors (SPMs) or photo-interrupters. The size of the SPM sensor is (3.4mm × 3mm × 3 mm) and is used in applications for binary presence detection. Each sensor comprised of an arrangement of a light emitting diode as light source (emitter) on one side, and a phototransistor as the light detector (receiver) on the opposite side facing each other. A small gap separated the emitter and the receiver, and the mechanical shutter was positioned in this gap. The operation of the SPM sensing head is based on the measurement of the intensity of a beam of light as a function of the position of an obstruction, in this case, the shutter placed in the optical path of the light beam.

This sensing head applied a differential voltage schema (Eq. 1) to reduce uncertainties due to the effect of variation in input voltage, influence of ambient light variations and differential thermally induced expansion between the sensor circuit and shutter.

$$D = K \times \frac{\left[\frac{(V1-V2)}{2}+\frac{(V3-V4)}{2}\right]}{2} \quad \ldots\ldots\ldots\

Their small size and low cost make them fit to be considered for embedding into machinery. For example, an optoelectronic displacement sensor consisting of a light source and photo receiver for micrometre range measurement of displacement was proposed and designed in [61, 62]. The performance of a similar sensor was investigated in [63, 64] where it was observed that the unfiltered resolution of the IR sensor was within sub-micron level range. An opaque box was used to cover the entire setup, and hence the effect of environmental variations was not reported. However, optoelectronic sensors are typically used for detection of binary presence and are affected by variations in ambient light.

Strain is the small change in dimension (length, width, or height) of a body when subjected to a force along that dimension. Strain measurement is used to determine the durability of materials subject to alternating strains during service (e.g., engine parts). Various techniques are available for measurement of strain. For example, strain gauges have the advantage of compact structure and low cost, but require surfaces that are clean as they are typically bonded to the surface being monitored [59]. This limits their application for use in harsh environments (e.g., shop floor). The performance of strain gauges is also affected by temperature effects, while their accuracy and repeatability decrease with prolonged usage. FBGs are becoming more widely used for measurement of strain due to the advantages of immunity to electromagnetic interference, and long life [65]. However, interrogation systems for FBG sensors are costly [66].

The real-time challenges of temperature compensation are not taken into account in current study findings. When the displacement sensor and the temperature compensation system are located in different locations, their response times to ambient temperature changes differ, causing temperature compensation to be erroneous. Research on real-time and accurate temperature-compensated displacement sensors, which may be used in circumstances where temperature varies regularly, is gaining popularity.

2.3.2. Photomicrosensors

A photomicrosensor, also known as a photointerrupter, is a small photoelectronic sensor that incorporates an emitter and a light detecting element facing each other with an optical light path between them. The emitter is a light emitting diode (LED) while the detecting element is a phototransistor. When there is an obstruction in the gap between the LED and phototransistor, the optical beam of the LED is blocked which reduces the amount of light incident on the phototransistor. In this way, the obstruction is detected by the photomicrosensor. Photomicrosensors are commonly

used as components in electronic equipment. They have an integrated amplifier and are used in a variety of applications, including positioning and object detection.

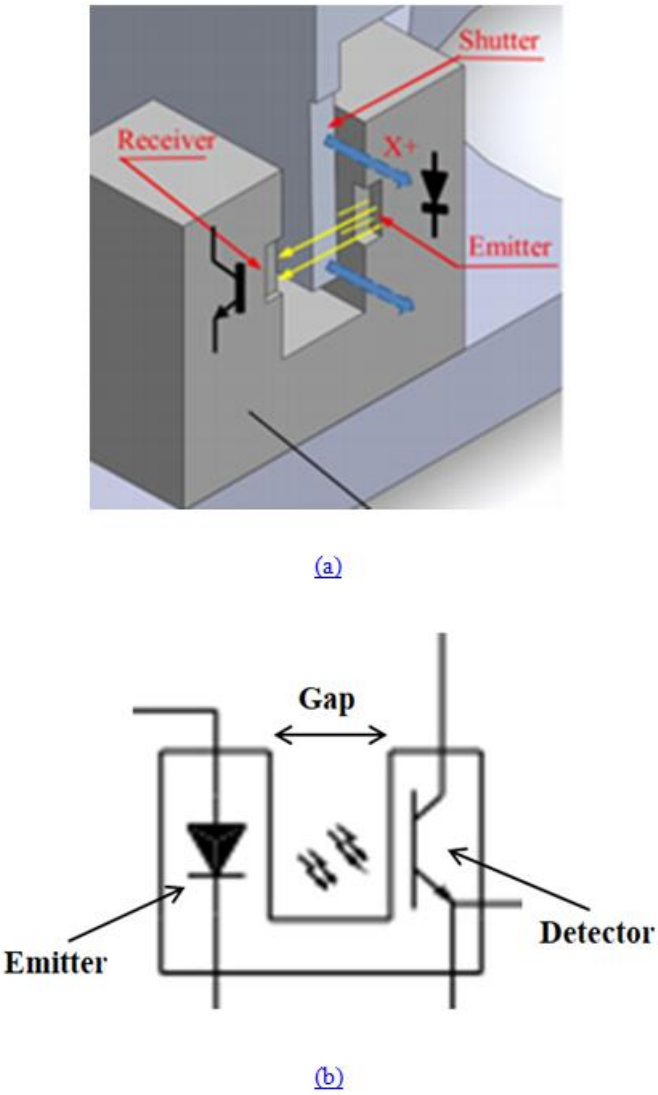

Figure 5: (a) Cross section of photomicrosensor showing emitter, detector, and an object in the optical path (b) Circuit schematic of photomicrosensor

Photomicrosensors are divided into several categories, including through-beam sensors, diffuse-reflective sensors, retroreflective sensors, and slot sensors. Because of their ease of setup and suitability for high precision position sensing, slot sensors were chosen for this study.

Characteristics of Emitter

The forward voltage of the LED incorporated by the emitter of the KRB021 is typically 1.1 V when a forward current of 25 mA flows through it. The LED output characteristics in Figure 6 shows that the forward voltage varies with a change in the forward current. Therefore, for optimum performance of the photomicrosensor, the forward current of the must not be too high or too low.

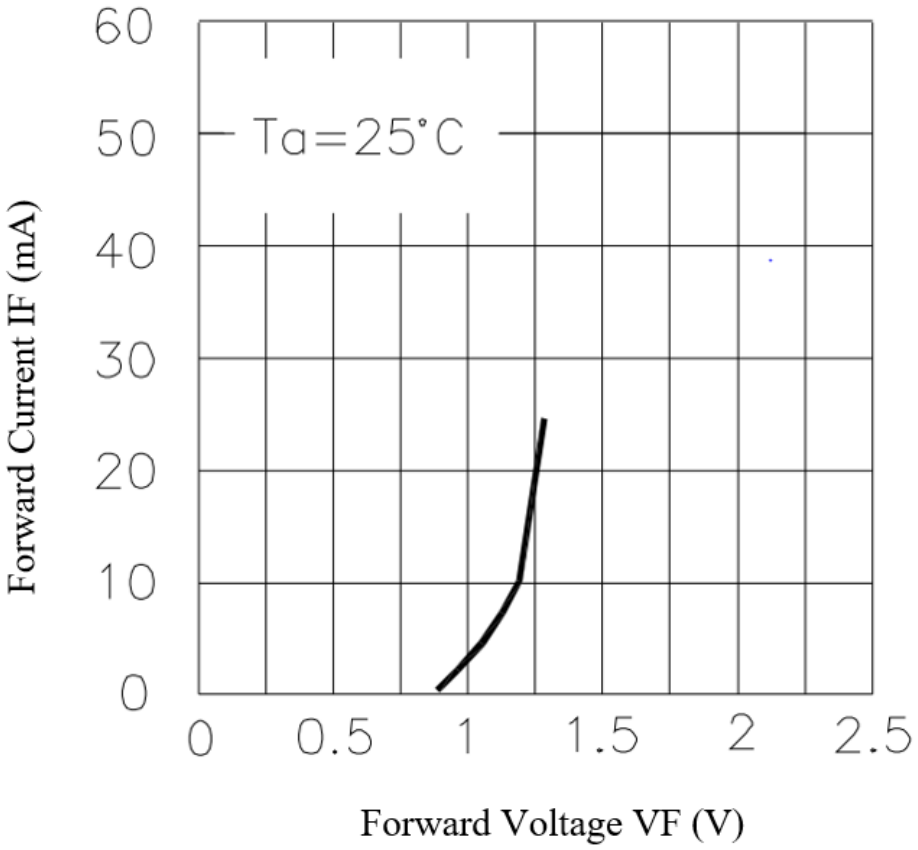

Figure 6: LED Forward Current vs Forward Voltage Characteristics [67]

Characteristics of Detector Element

The detector element of the photomicrosensor is a phototransistor. The amount of light from the emitter that flows in the detector is determined by the LED forward current. When an appropriate level of forward current flows through the emitter, and there is object between the emitter and detector, the light current flows into the detector. Conversely, when there is no forward current from the emitter to the detector, a leaking current from the phototransistor called dark current, flows in the circuit. The dark current becomes larger with increasing temperature of the environment as shown in Figure 7. Therefore, it is important to avoid dark current when designing circuits with photomicrosensors especially for high temperature applications.

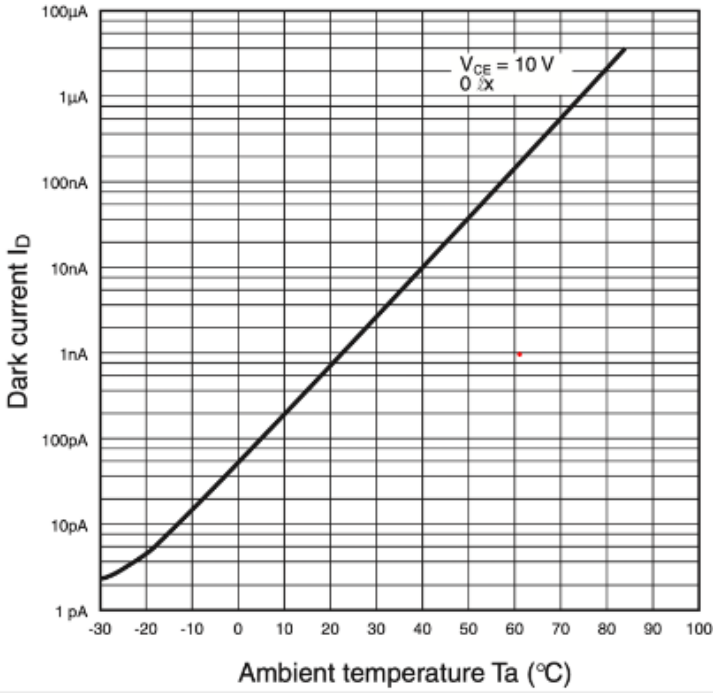

Figure 7: Dark Current vs Environmental Temperature Plot [68]

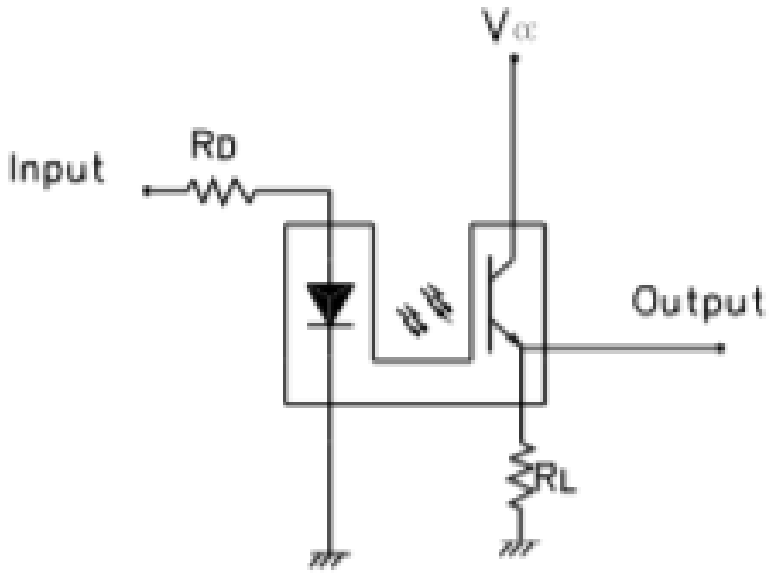

Figure 8: Basic photomicrosensor signal conditioning circuitry [67]

RD is a limiting resistor and RL is a load resistor.

A signal conditioning circuit that powers the LED of a photomicrosensor includes a limiting resistor and a load resistor as shown in Figure 8. The forward impedance of the LED is low and if the LED is connected without a limiting resistor, a large current will flow through it. This will cause the LED to burn out. To avoid this, the limiting resistor must be carefully chosen.

The photomicrosensor carefully chosen for the sensor control circuit design in this research is the model Kingbright KRB021 and the working parameters considered in the circuit design is shown in Figure 9 and Table 2.

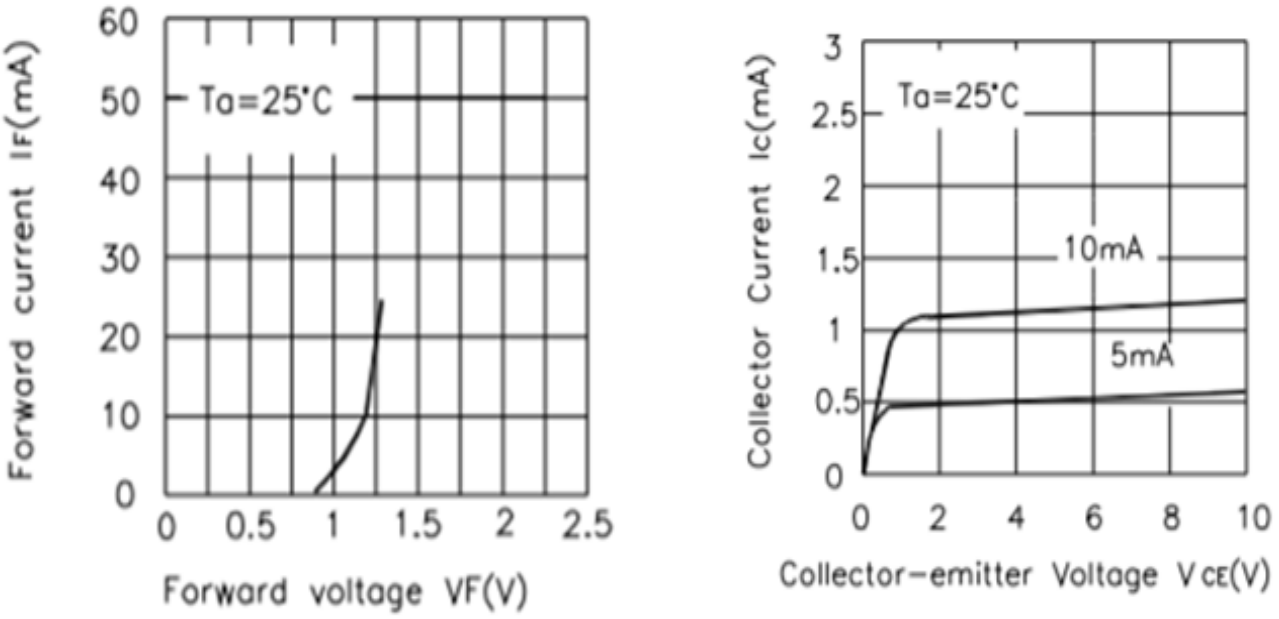

Figure 9: Kingbright KRB021 Engineering data [67]

Table 2: Working parameters of KRB021 Photomicrosensor

	Item	Rated Value
Emitter (LED)	Forward current	I_F = 25 mA
	Forward voltage	V_F = 1.1 V
Detector	Collector Emitter saturation voltage	V_{CE} = 1.1 V
	Collector current	I_C = 150 µA

According to a manufacturer of photomicrosensors OMRON, the forward voltage upper limit is not defined if the LED is connected to a suitable current limiting resistor. However, it is required that the LED forward voltage lower limit should be between 1.1 V to 1.3 V to allow the flow of forward current to the LED.

From the above, the limiting current resistor is determined as follows. The forward current (IF) of the KRB021 is 25 mA. Therefore, the limiting resistor must be selected to allow approximately 25 mA forward current to flow to the LED. The value of the limiting resistor can be gotten from Ohm's Law as follows:

$$R = \frac{V_{CC} - V_F}{I_F}$$

Where V_{CC} is the supply voltage.

For the circuit implementation,$V_{CC} = 10$ V, $V_F = 1.1$ V and $I_F = 25$ mA. Thus, the limiting resistor is estimated as 356 Ω. The closest standard resistor used in the circuit design is 330 Ω.

It is important to set a correct value of load resistance to the photomicrosensor circuit. This will ensure that the phototransistor can allow the flow of the correct amount of circuit current. If the value of the load resistance is too small, the circuit current will not flow.

Generally, when designing a system that uses a photomicrosensor, consideration is made for a reduction of the light current I_L by 50%. This is due to temperature effects and degradation over time.

Calculation for Load Resistance Value

Most manufacturers of photomicrosensors report that the light current $I_{L(MIN)}$ is typically 0.5 mA for a forward current I_F = 20 mA.

Although $I_F = 25$ mA for the KRB021, the actual forward current for the circuit used in this design is $I_F = \frac{V_{cc} - V_F}{R_D} = 26.9\, mA$.

$$\text{Actual } I_{L(MIN)} = \frac{0.5 \times 26.9}{20} mA = 0.673\, mA \ (at\ I_F = 26.9\, mA).$$

Allowing for degradation, Actual $I_{L(MIN)} = 0.5 \times 0.673\, mA = 0.336\, mA$.

The load resistor is obtained using the relation;

$$R_L = \frac{V_{cc} - V_{CE(SAT)}}{I_c}$$

$V_{CE(SAT)} = 0.1\, V(typical) to\ 0.4\, V(maximum), I_C = 150\ \mu A$ from datasheet of KRB021 [67].

Substituting the values in the equation results in a load resistance value $R_L = 32.67\ k\Omega$. The closest standard resistor value is 33 $k\Omega$.

2.4. Review of Analytical Methods

2.4.1. Finite Element Method

The FEA is a computational mechanics method to develop and simulate mathematical model of a system using numerical methods. It is a valuable tool used to estimate various effects such as strains, distortions etc., resulting from mechanical and thermal loads. It provides the possibility to carry out a comprehensive analysis of the thermal performance or behaviour of the components of machine tools when subjected to the varying sources of heat present in the structure of the machine tool, and in its environments. With the implementation of the Finite Element Method (FEM), research on methods of identifying and thermal errors of machine tools gained more attention and became more successful Figure *4* Figure 4 shows the FEA result of the thermal influence on a machine tool structure. Knowledge from FEA results can be applied to reduce or eliminate these effects on structural parts.

At the design stage of machine tools, numerical methods are used to simulate the effect of temperature on machine tool components and to identify the components or sources of thermally induced distortions. Due to computing time, machine design engineers often calculate only the results of steady state simulations. While this is simple, steady state simulations data cannot reliably capture the behaviour of the machine tool over time. Transient simulations [12] can effectively capture this behaviour over time. It is important to accurately predict the thermal stability of machine tools in order to prevent costly machine tool design changes and achieve higher accuracies.
With the implementation of the Finite Element Method (FEM), research on methods of identifying and thermal errors of machine tools gained more attention and became more successful [6].

Many manufacturing structures are subjected to repeated temperature changes on a regular basis. Hence a thorough understanding of the influence of temperature effects on strain measurements is vital for accurate determination of the mechanical strain induced by any unpredicted loading situations.
Sensors are used to measure the physical parameters in structural health monitoring (SHM). And structural strain change is one of the most frequently measured quantities in SHM to examine the performance of structures under loading. Unfortunately, the sensors used in these SHM schemes are exposed to and adversely affected by changes in temperature which induces a thermal component in the strain measured by the sensors. This is primarily due to differences in the thermal expansion properties of the materials that make up the sensor and the material of the structure in which it is installed. [69], for example, measured the output of four strain sensors under load, including a vibrating wire strain gauge (VWSG) and a fibre Bragg grating (FBG) sensor. The findings of the investigations

showed a 25% variation in the senor performance under a constant temperature. The VWSG was shown to produce the most stable and reliable results while the electrical resistance (ERS) sensors showed the most unreliable results because of their sensitivity to the test environment.

In conclusion, there is increased demand for high quality measurement systems for use in many engineering applications. Because most of the commercially used strain sensors are impacted by temperature to some extent, the accuracy of their output values need careful calibration and validation. There is also increased interest in procedures that will allow comparison of the results from measuring systems. Customers and end-users of developed technologies want to know that the measurements taken by the measuring systems are accurate and traceable. As the result of every measurement is only an estimate of the true value, the only way to prove that measurements are accurate is to compare them against measurements from more accurate instruments, and show that their uncertainty is low enough that the appropriate conclusions can be formed from the data, such as whether a workpiece fulfils its specifications. As a result, the best way to demonstrate traceability is to start with the measurement's uncertainty budget. Most studies in the literature would generally include readings from multiple independent devices to allow cross calibration and comparison, but there is currently little quantitative evidence on the sensor's reliability when subjected to exogenous influences.

Laser interferometers are very accurate and well-established measuring instruments and are often used as a measurement standard against which other measuring devices can be compared. Employing measurement standards in a measurement system builds confidence in the system and allows the use of different technologies to perform the same measurements. In this way, the measurement parameters can be easily and confidently combined for analytical purposes. The papers reviewed in the literature did not use a laser interferometer as a traceable reference for their tests. External and environmental factors, such as temperature, can alter the output characteristics of a sensor over time. Also, the reviewed literatures did not provide a thorough uncertainty assessment of the measurement system. Furthermore, the literatures did not discuss the traceable calibration of sensors in embedded applications without removing the sensors from the process. This is particularly relevant in digital factories where many sensors are embedded, and calibration is difficult to achieve. Simple sensors with high resolution over long distances and low-price potential have been the subject of research. The available measuring systems reviewed in this literature have not provided a solution that is cheap and combines high resolution measurement over long distances. Thus, the production of easy-to-use instruments for measuring displacement at nanometre levels remains a challenge for nanotechnology.

2.5. Summary of Findings from Literature

An overview of the most common and least common sensing procedures have been presented. Strain monitoring is an effective way to understand the material behaviour when loaded, which is important for the reliable use of composite materials. A summary of sensor performance characteristics discussed in this review is presented in *Table 3*.

Table 3: Summary of displacement sensor performance characteristics [40]

Sensor type	Range	Resolution	Accuracy
Metal foil	10 - 500 µm	23 nm	1% FSR
Piezoresistive	1 - 500 µm	0.49 nm	1% FSR
Capacitve	10 µm to 10 mm	2.4 nm	0.1% FSR
Eddy Current Sensors	100 µm to 80 mm	1 nm	0.1% FSR
LVDT	0.5 to 500 mm	5 nm	0.25% FSR
Linear Encoders	Several Meters	6 nm	5 ppm FSR
Laser Interferometer	Several Meters	0.49 nm	1 ppm FSR

Electrical strain gauge-based sensors have been widely used for strain measurement. However, their sensitivity to electromagnetic fields, limited surface area, and incompatibility for embedding applications are some drawbacks. Their resistance during fatigue reduces, resulting in unreliable strain monitoring.

Semiconductor strain gauges have key advantages over typical strain gauges. They have a longer fatigue life, making them suitable for long-term applications. They have a high gauge factor, which means they have a lot of sensitivity. They are smaller in size compared to foil metal strain gauges which allows for the measurement of localised strains. However, their non-linearity and high temperature dependence are notable drawbacks.

Fibre optic based displacement sensors such as FBGs are being developed and applied to machinery structural monitoring applications. They also feature crucial characteristics including light weight, multiplexing and accurate measuring capacity, as well as resistance to corrosion, making them excellent for strain and structural health monitoring applications. A major disadvantage is their exceptional fragility, which necessitates meticulous and competent installation.

Miniaturization and integration of several sensing technologies is becoming increasingly popular today. As with the interferometric methods, the combination of high number of sensors, signal conditioning and signal processing means that the overall costs are prohibitive for many embedded

applications where the costs cannot be shared across multiple machines or a factory. The benefits of direct measurement of strain in place of, or to complement, temperature monitoring has been shown therefore there is a need for an alternative sensor which has the requisite performance and cost compatibility.
Generally, a sensor that will be applied for structural deformation monitoring in precision machinery such as CNC machine tools, cast iron steel structures, etc is expected to have a resolution (6σ) of better than 10 nm, must not present any characteristics that will limit repeatability such as hysteresis, especially as machine tools depend on repeatability. Such a sensor should also exhibit frictionless motion between the reference and moving target [40].

The analysis presented in this review is critical in providing newer highly integrated systems to ensure the performance of complicated structural configurations. Based on the discussed scenarios the key projected impacts of the present research will include creating a sensor that uses a novel arrangement of low-cost mass-manufactured photomicrosensors, which can be combined in a framework to enable structural distortion sensing.

2.6. Methodology

A methodology based on literature review and experimental design is described to fulfil the goals and objectives of this research work.

In **chapter 3**, the design considerations of a novel SPM-based sensor will be described.
Four SPMs will be soldered unto a circuit board to be attached to the sensor base and connected to a signal conditioning circuit. The sensor design consists of two parts – static and dynamic parts, held together by a flexure system.
In order to evaluate the flexure stiffness, finite element analysis (FEA) simulations will be performed using SolidWorks by applying an axial force of 1 N on one flexure and measuring the distortion.
To investigate the application of the sensor for structural monitoring, a setup comprising of the sensor and connecting rods made of Carbon Fiber Reinforced Plastics (CFRP) will be designed. FEA simulations will be performed to examine the response of the system by observing the change in the structure as a function of temperature variation.

To validate the suitability of the sensor for structural deformation monitoring, a framework will be validated through tests using an XL 80 Renishaw interferometer as a reference measurement.

In Chapter 4, the performance of the newly designed sensor will be investigated through experiments to examine its repeatability, linearity, and stability. The test setup will consist a Coordinate Measuring Machine (CMM) (Eley Toccata), an ML 10 laser interferometer, a Thorlabs PAZ015 piezoelectric actuator with feedback, and the newly designed sensors.
Tests will be performed by moving the piezoelectric actuator over the linear range of the sensor. The SPM-based sensor will be paced on the CMM bed while the laser optics will be mounted on the SPM sensor. The piezo transducer will be attached to the shutter of the sensor. In this way, the sensor and laser optics will experience the same displacements.
The sensor will be put through a series of tests in order to characterise it and estimate the influence of uncertainty contributors on the sensor performance based on the GUM.

In chapter 5, an in-situ calibration technique that reduces the impact of the error sources on the sensor that has been newly designed and manufactured after preliminary frame testing in Chapter 3.
To investigate the in-situ calibration method, tests will be performed using the setup in Chapter 4. The supply voltage to the sensor will be varied by mechanically turning its knob at different positions within its measurement range for an uncalibrated and calibrated sensor. A piezo controller and actuator will be attached to the SPM sensor module to perform controlled displacements.
The results for both the calibrated and uncalibrated sensor will be compared by statistical means and a differential voltage method will be applied to detect and correct the errors.

In chapter 6, an improved 3D printed design of the SPM sensor is presented. The design considerations of the improved sensor with the changes made are described, and FEA simulations will be performed to investigate the performance of the improved design. In order to eliminate friction in the mechanism that allows relative movement of the two sections of the sensor, a flexure solution will be employed. Fine adjustment of the shutters will be done using M2 grub screws.
Finite Element Analysis (FEA) will be used to validate the 3D sensor design and investigate the effect of changing environmental conditions on the joining members. To determine the sensor static stiffness, a force of 1 N will be applied axially to one flexure and the distortion of the flexure will be measured.

Finally, a setup of the sensor with suitable zerodur connecting rods for strain monitoring will be investigated.

Chapter 7 presents a summary of the output of this research work, and suggestions for further research on this subject.

Chapter 3 - Sensor Design

A displacement sensing head was created in [48] using cheap slotted photo-microsensors (SPMs) which are easily accessible. The design consists of a unique compact arrangement of SPMs with specially designed shutter assembly that proved the principle of a differential voltage sensing method. The differential principle was reported to reduce the uncertainty contributions from changing ambient light conditions and power supply. The performance of this displacement sensing head under ideal conditions was determined through experiments and tests using a laser interferometer as a reference measurement. The reported characterisation results include sensitivity of 0.1648 V/ µm, resolution of 21 nm, repeatability of 90 nm, a linear range of 20 µm, and an accuracy of ±1% over the full scale range of 20 µm.

However, [48] did not create a measuring system that incorporates a sensor housing, flexure system, a way of transmitting the loads using suitable connecting rods, and which can be applied for structural monitoring. Also, the sensing head developed in the previous research had significant design challenges which precludes its application for structural monitoring especially in embedded applications. For example, the shutters had to be filed until they fit into the gap in the SPM. This made it difficult and time-consuming to achieve pairwise clustering of the SPMs, which is a vital characteristic of the sensor.

The very good characteristics of the sensor (resolution of 21 nm, linear range of 20 µm) will be exploited to create a sensor design that can be applied for monitoring structural deformation. These values will be quoted in this research work because no change was made to the differential principle of the sensor created in [48], and the design improvements in this research work have been implemented in such a way as to maintain the exploitation of these characteristics. For example the use of a sliding mechanism will introduce friction to the sensor which will alter the sensor principle.

The differential voltage design of the sensor significantly reduces some uncertainty contributors such as change in input voltage and ambient light which is important for the discussion in this thesis.

The main design requirements of the sensor are:

i. Bi-directional frictionless motion.
ii. One degree of freedom (DOF) sensor movement.
iii. Easy manufacture, assembly and flexibility for integration in embedded applications.
iv. Reduced effects of temperature
v. Low uncertainty for a system that uses the developed sensor.

To achieve the above design requirements, a mechanical housing and framework for structural deformation monitoring was created taking the cost and uncertainty into consideration. The materials and the dimensions used in the design of the housing were carefully chosen to minimize thermal effects and allow for use in embedded applications. SPMs are generally ultra-low cost, hence the sensor design will be restricted by manufacturing cost. This reason influenced the adoption of a 3D printed solution which allows simplified assembly and eliminates the machining of small intricate parts. Furthermore, to achieve frictionless movement between two sensor parts of the sensor, flexures were used in the design. This also constrained the relative movements of the parts to 1 DOF.

This chapter summaries the principle of operation of the sensor, and describes the design improvements to achieve the above aims. The design of the sensor with novelties around the flexure, shutters, and the application of the sensor for strain measurement with CFRP rods is described, and the results of the system are presented. The test results show good correlation when compared with results from a laser interferometer.

3.1. Introduction

A major challenge of positioning sensing is achieving high resolution and accuracy over a useful range. The good qualities of high resolution, simplicity and low cost have been combined in many research work to create measuring systems. Previous research [48] has revealed that mass-produced small transmissive photomicrosensors can be used to carry out displacement measurement with good resolution and good accuracy when combined with differential outputs from several sensors. Their small size and ultra-low cost of typically less than 1GBP make them suitable to be considered for embedding into machinery. The low-cost infrared (IR) transmissive sensors are also known as photo-interrupters or slotted photo-microsensors (SPMs) and the latter will be used in this research.

This research will investigate the potential application of this novel sensing head for structural monitoring. No attempt has been made to create a strain measurement system using this sensor. This section describes a measurement system that uses the SPM array and suitable connecting rods to increase the spatial coverage and attachment to the structure for direct measurement of strain.

The size of the SPM (Kingbright KRB021) sensor used in the previous research is 3.4mm × 3mm × 3 mm and is typically used in applications for binary presence detection. Each sensor is comprised of an arrangement of a light emitting diode as light source (emitter) on one side, and a phototransistor as the light detector (receiver) on opposite sides and facing each other. A small gap separates the emitter and

the receiver, and the mechanical shutter was positioned in this gap. The operation of the SPM sensing head is based on measuring the intensity of a light beam as a function of the position of an obstacle, in this case, the shutter placed in the optical path of the light beam. As the shutter prevents light coming from the emitter from reaching the receiver, its movement is proportional to the displacement (example by expansion or contraction) it encounters. When the shutter is fully positioned between the emitter and the detector (i.e., the gap between the emitter and detector is zero), the detector does not sense any light from the emitter. However, when the shutter moves or is displaced, the size of barrier to the photosensitive area between the emitter and detector is altered and light from the emitter reaches the detector. As the output voltage from the receiver is proportional to the intensity of light beam incident on it hence, the resultant movement of the shutter will be sensed.

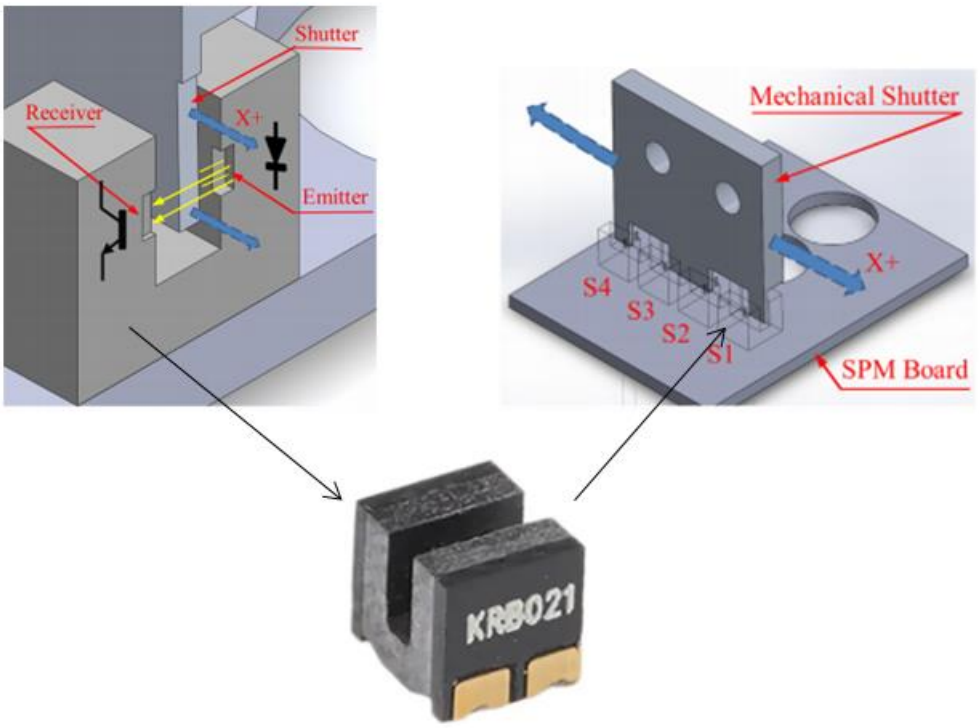

Figure 10: Cross section of single sensor and shutter [48]

The SPM sensors are normally used to detect binary presence in process control applications; therefore, the output voltage of a single SPM is sensitive to variations in the ambient light and supply voltage. To overcome the effect of these variations, four (4) SPMs (S1 – S4) are arranged in a way that they act together with the shutter to provide cancellation, Figure 10.

The shutters are designed to change the signal strength, of each pair of optical sensors linearly as they move with reference to each other. The transmittance of the shutter is symmetric at its centre and ranges from low to high from the outside edges. The shutter clusters the sensors in pairs such that sensor S1 and S2 form a pair, and S3 and S4 form another pair. When the light to one sensor is blocked by the shutter, the same proportion of light is allowed in the second sensor, as shown in Figure 11

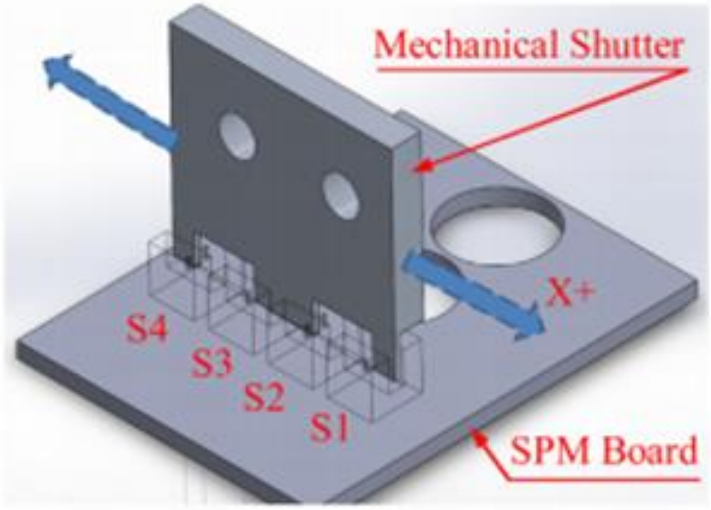

Figure 11: Shutter and SPM implementation for differential measurement

Thus, a differential measurement is produced for each pair and this redundant approach was shown to give a more stable signal for measurement. Taking an average of the two (2) differential outputs significantly reduces the impact of variations in ambient light and thermal expansion between the shutter and the sensor circuit. This arrangement is described in the equation (1) below and implemented using a LabView program.

$$D = K \times \frac{\left[\frac{(V1-V2)}{2}+\frac{(V3-V4)}{2}\right]}{2} \quad \ldots\ldots\ldots\

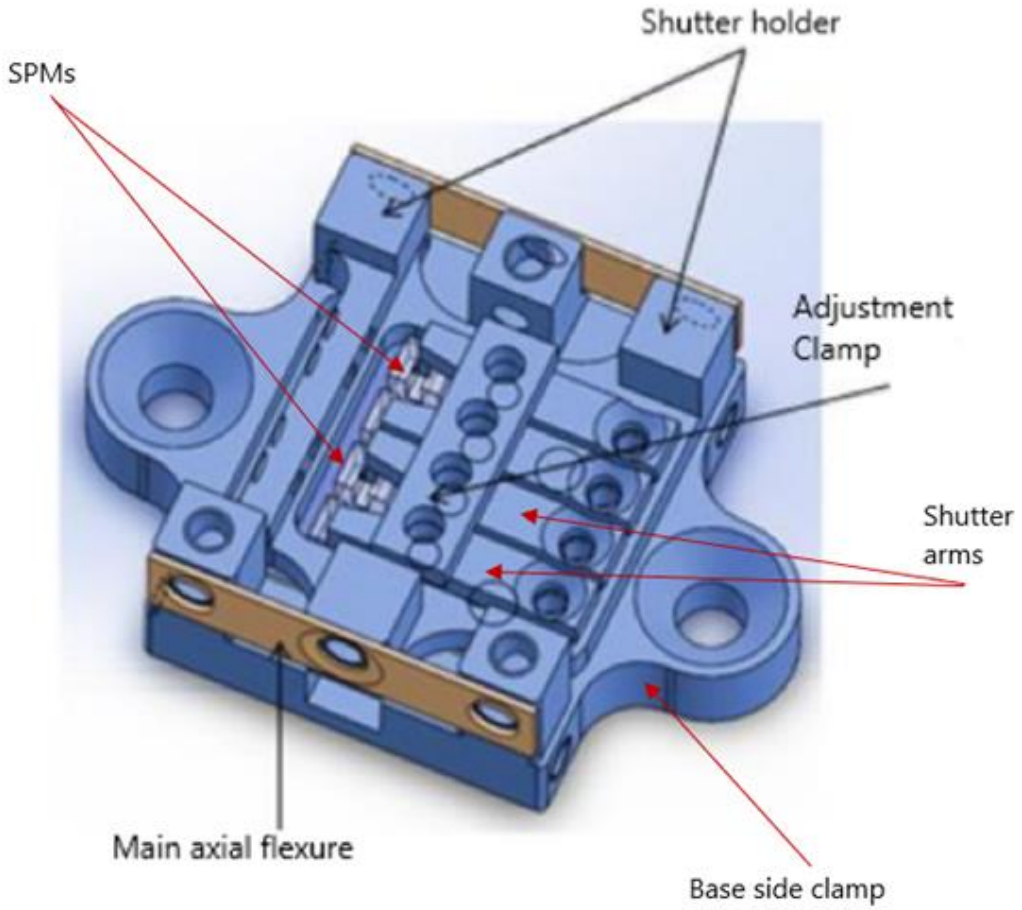

Figure 12: Description of SPM sensor

The SPMs are soldered on to the quad single slotted sensor (QSSS) circuit board which is then mounted on the base side clamp. The QSSS circuit board will be attached to an amplification device while the base side clamp will provide base for the sensor assembly. Four shutter arms that are supported by a shutter holder are then positioned on each SPM (between the emitter and detector). An adjustment clamp is fitted on the shutter arms using M3 countersunk head screws to ensure proper positioning of the shutters. This design comprises of two axial flexures that are used to hold the shutter holder on to the sensor base which is mounted on the reference structure. A novelty of the design of the flexures is to allow only one degree of movement of the sensor.

There is a massive selection of different SPM sensors available commercially. The slot type is selected for the prototype device because of its low cost, ease of setup and suitability for high precision position sensing, compact size (3.4 mm x 3 mm X 3 mm) and high resolution with a small aperture width of 150 µm. Furthermore, optimal transfer of light from the emitter to the detector is ensured by selecting

a unit with a small gap (1 mm). This reduces the effect of varying environmental light conditions as the shutter moves.

The parts of the sensor which includes the shutter arms, shutter holder and base side clamp are manufactured using aluminium. This is because of the light weight, low cost and machinability. Although aluminium has a high thermal expansion coefficient, the housing is very small and should change homogenously reducing gradients and distortion. The small size of the sensor will also facilitate machine integration.

The signal conditioning circuit used to establish proper operating conditions for the SPM consists of an arrangement of resistors and a capacitor. These components can cause increased temperature through local self-heating. Therefore, the circuit is located remotely from the SPM board.

A novelty of the sensor design is the flexure mechanism which uses a highly symmetric geometry to constrain 5 degrees of freedom (DOF) and allow movement in only one direction.

3.3. Flexure Mechanism

Precise movement of guides is needed in many nano/microelectromechanical systems (N/MEMS) need high precision motion guidance to attain efficient performance, examples include in MEMS sensors and actuators, micro manufacturing and micro assembly [70, 71]. To achieve the required performance in these applications, the movement of a particular block must be strictly controlled, magnified or limited in some defined directions. Traditional rigid link mechanisms can move by rolling or sliding but this is undesirable as they can induce hysteresis, wear, and backlash. Also, fabrication of traditional mechanisms with sliders is tedious task and quite impossible in nano scales.

To overcome the limitations of traditional positioning systems, researchers have developed flexure-based micro/nano-positioning units. Flexure mechanisms can provide guided movements with high repeatability which makes them attractive for high repeatability applications. Their motion is caused by the deformation of elastic components meaning that they are frictionless, do not exhibit backlash, and are void of stick-slip and wear, which results to low hysteresis [72-74], and larger range of motion [75]. The lack of play and friction results in predictable behaviour that is essential for precision positioning. Flexures are designed to provide precise displacement when a specified force is applied, or to provide a known force upon the application of specified displacements. Different kinds of flexures such as trapezoidal flexures[76] and cartwheel flexures[77], have been used in recent studies. For a flexure system, the relative stiffness of the drive and flexure represents a measure of achievable precision. A major drawback of flexure joints is that at large displacements, the thickness of the support

systems decreases significantly. To overcome this drawback, the design of the flexure is optimised to obtain the required thickness.

The novelty of the SPM sensor design is the flexure mechanism which creates a symmetric geometry and the frictionless motion. In this case, spring steel was deemed a good choice for a widely available thin solution for the flexures. The sensor is made up of two (2) parts – a static part and a moving part. The base forms the static part while the shutters and shutter holder together make up the movable part.

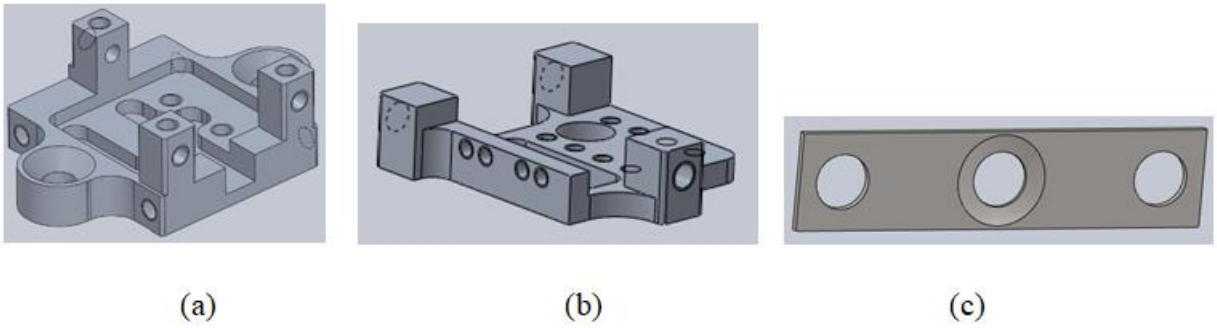

Figure 13: Component parts of sensor housing (a) sensor base (stationary part), (b) shutter holder, (c) main axial flexure

The shutters are designed to move in one direction and together with the SPMs, provide sensing. This unique arrangement of the static sensor part and flexure provides a very high degree of decoupling between the X and Y axis, which in turn allows unconstrained motion along one direction. A CAD design of the initial flexure joint design can be found in Figure A - 1. A limitation of the flexure is the addition of mechanical stiffness. Hence, the behavior of the flexure was evaluated using FEA to estimate its static stiffness. A fixed geometry is applied on the base side clamp as shown in Figure 15 to constrain any movement of the base. A force of 1 N was applied in the negative z-direction on the flexure that is connected to the shutter holder. A standard mesh is used in this simulation because it is not a complex part and the bending effect on the flexure is expected to be small. The material and mesh properties used in the simulation is shown in Table 4 and Figure 14.

Table 4: Material Properties used in the FEA evaluation of the axial flexure static stiffness

Property	Value	Units
Elastic Modulus	2.1×10^{11}	N/m^2
Poisson's Ratio	0.28	N/A
Shear Modulus	7.9×10^{10}	N/m^2
Mass Density	7800	Kg/m^3
Tensile Strength	3.998×10^{8}	N/m^2
Yield Strength	2.21×10^{-5}	N/m^2
Thermal Expansion Coefficient	1.3×10^{10}	
Thermal Conductivity	43	W/(m.K)

Study name	Static 1 (-Default-)
Mesh type	Solid Mesh
Mesher Used	Standard mesh
Automatic Transition	Off
Include Mesh Auto Loops	Off
Jacobian points for High quality mesh	16 points
Element size	1.27212 mm
Tolerance	0.0636059 mm
Mesh quality	High
Total nodes	93853
Total elements	53210
Maximum Aspect Ratio	14.706
Percentage of elements with Aspect Ratio < 3	96.3
Percentage of elements with Aspect Ratio > 10	0.38
Percentage of distorted elements	0
Number of distorted elements	0
Remesh failed parts with incompatible mesh	Off
Time to complete mesh(hh:mm:ss)	00:00:19

Figure 14: Mesh properties from FEA evaluation of flexure static stiffness

This section discusses a unique arrangement of a sensor and flexure system to achieve 1 DOF of motion and evaluates the stiffness and displacement characteristics of the flexure.

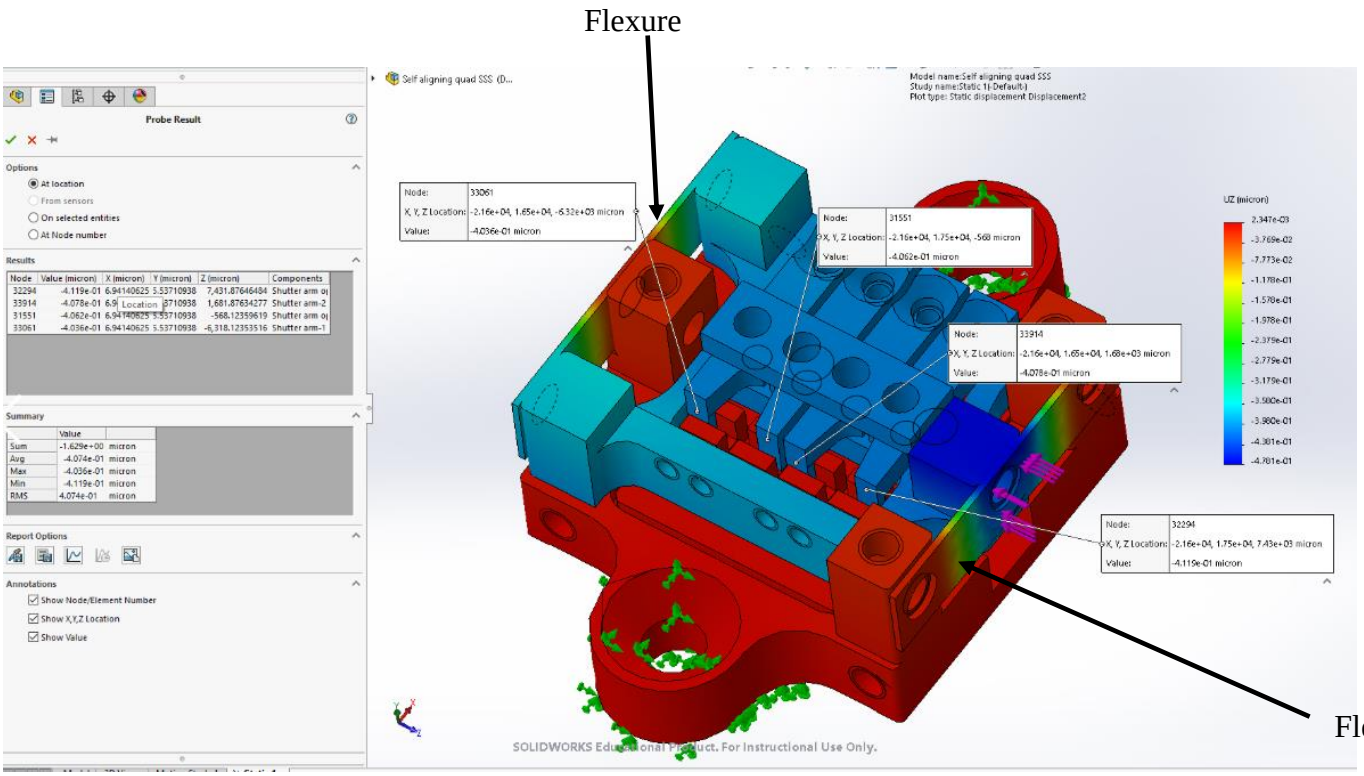

Figure 15: Static Test on Self Aligning Quad SSS to determine the stiffness of the flexure on the application of 1 N force

A static test was created to investigate the stiffness of a sensor module. The spring steel flexure thickness was set to 0.5 mm since this was available and seemed to be a good compromise between low stiffness and manufacturability. The simulation used a fixed constraint to represent rigid connection to a surface and application of a force on the main axial flexure as shown in Figure 15. Each sensor module consists of 4 SPMs to which shutters are attached. Nodes (points on the face of each shutter) were selected on each shutter, and the values of each node represents the movement of the individual shutter relative to the SPM. By applying a force in the negative Z-direction as shown, the movement of the shutters relative to the sensor surface can be measured.

The base is fixed hence there is no movement. The shutters move in the negative Z-direction relative to the KRB021 SPM sensors which are attached to the base. The node data on the surface of the shutter indicates the movement of the shutter relative to the SPM (Y1 from Table 5). For a force of 1 Newton, the 4 nodes move as shown in Table 5.

Table 5: Table showing movement of shutters on the application of 1 N force

Shutter Nodes	Y1 (UZ (micron))
32294	-0.411
33914	-0.408
31551	-0.406
33061	-0.404
Average Displacement	-0.407

From Table 5, the average displacement of the four (4) shutters is 0.407 µm for a 1 N force.
The stiffness of a body is the degree to which it can resist deformation at the application of a force and is measured in Newton per metre (N/m).
It is defined mathematically as $stiffness\ k = \frac{Force}{Extension}$
From the study, a force of 1N, results in an average displacement of 0.4074 µm.
Hence, $stiffness\ k = \frac{1}{0.4074 \times 10^{-6}} = 2454590.083 \frac{N}{m} = 2.45 N/\mu m$

This force required to deflect the flexures will have an impact on the mechanism used to join multiple sensor modules together but will be a systematic effect that can be corrected.
The standard deviation in the displacement measured by the face of each shutter is negligible at 0.008 µm. As it is practically impossible to perfectly align all four shutters, the variation is very small compared to the sensor measuring range, thus will have no significant impact on the measurement result. This confirms that the 1 DoF motion of the shutter which will reduce uncertainty from cross-talk or unwanted lateral movements of the shutter.

It should be noted that the single sensor was evaluated before its application for strain measurement. However, it was reported later in this thesis because it seemed to lead well to the discussion on uncertainty analysis and the chapter on the 3D printed sensor.

A framework that uses the developed sensor and suitable connecting rods for structural monitoring was evaluated through FEA simulations before machining the sensor. This is because it did not require complex machining which was not to be done before bench testing the idea. In this way, cost and time of machining a faulty design is avoided.

3.4. Dual sensor on example structure

Three sensor modules were set up to measure the strain on a fixed structure. The first module is just a fixation direct to the structure i.e. the first rod is connected to the static part of the module. Only two are module subject to the strain effect. The sensor modules were fixed on to the structure being monitored and connected using short unidirectional carbon fibre rods. A thermal force was applied on the structure to generate elongation and the effect of this force on the sensor setup was investigated using FEA. The setup is shown in Figure 16.

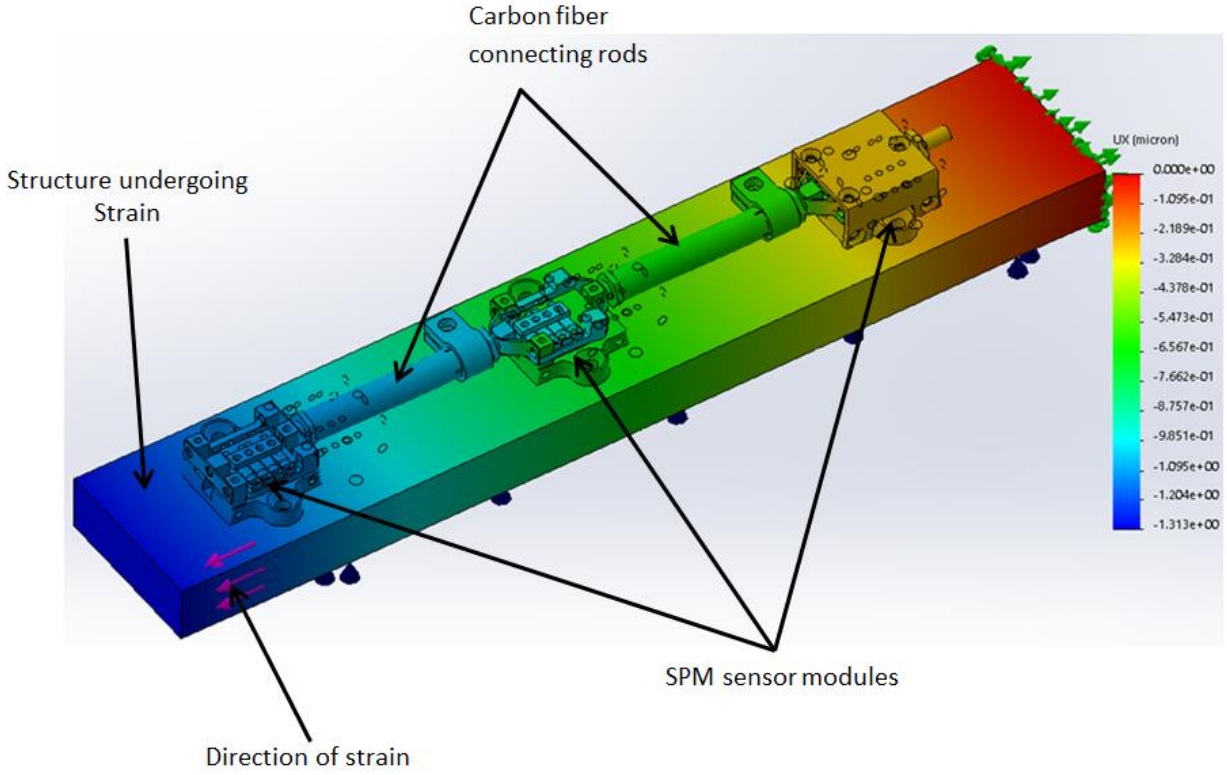

Figure 16: Multi sensor setup to measure the strain on a structure using the SPM sensors and carbon fiber connecting rods

Thermal stress analysis was performed on the structure to measure the strains, stresses and deformations that occur within the structure with changes in temperature. A thermal study was performed on the structure and the result was imported to a transient analysis. The reference temperature at zero strain was 20°C.

For the transient thermal study, a convection coefficient of 6 W/m/°C was defined on the entire structure. Two (2) metal ceramic heater elements (Figure A – 2), 24 W from Thorlabs (HT24S2) were used to increase the temperature of the structure. Each heat pad was attached to the bottom of the

structure, and located 20 mm from both ends. The temperature of the heat pad was specified as 25°C for 3600 seconds to simulate heating of the structure. The transient study showed a steady temperature of 25.00°C on the bottom of the structure and a maximum temperature was attained within 5 minutes. The heat transfer in the contact region was defined using a bonded type of contact resistance of 0 °C/W.

To evaluate the stresses in the structure due to thermal loading, a linear static study was created. The result of the last step of the transient thermal study was imported into the static study while one end of the structure was fixed.

The strain due to the expansion of the structure was measured as shown in Figure 17.

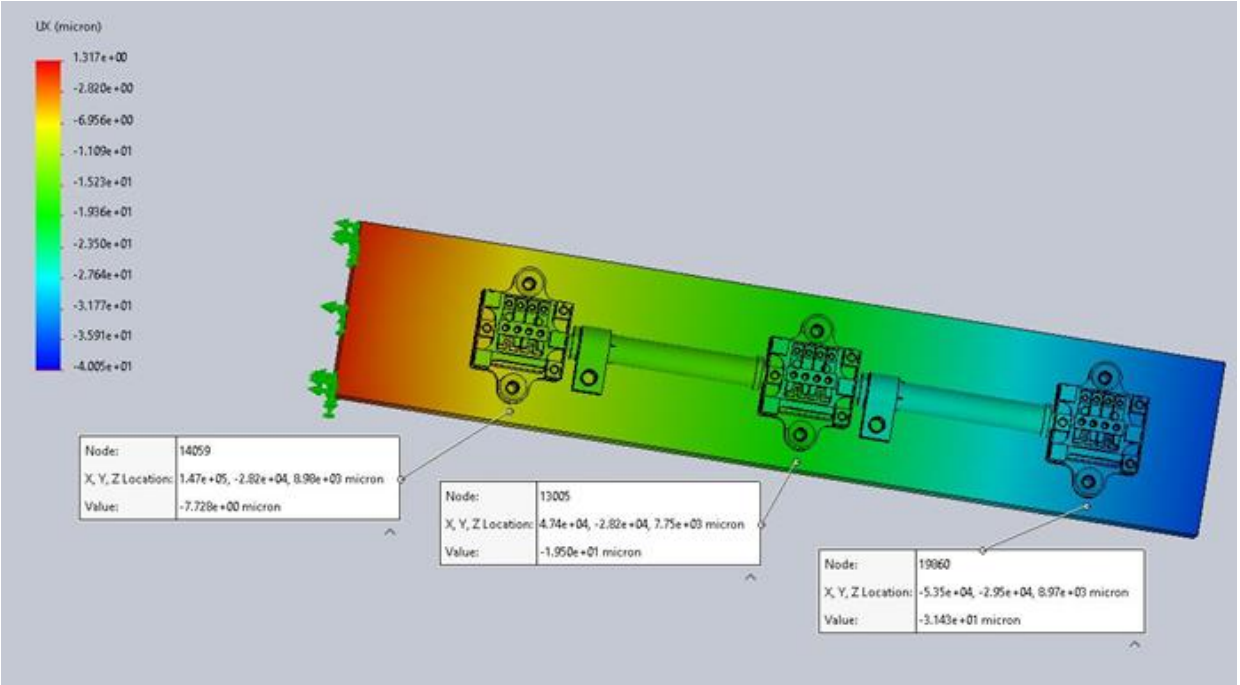

Figure 17: Multi sensor setup - strain measurement

Directly extrapolating the deformation of the structure from strains is a complex process.

An approach was adopted in [18], where in order to detect the total extension of point-point dimensions of a machine tool, an FBG was used as a displacement sensor. A similar approach is used in this research.

In this case, the sensors are measuring the deviation between two nodes on the surface of a structure. Therefore, the results in Table 6, Table 7, Table 13 and Table 14, are displacements measured in micrometers resulting from the strain in the beam. In order to create a comparison of nodal displacements with sensor readings, which is a displacement reading, then all of the results are in microns.

The extension on the structure between the left sensor and middle sensor was measured as 11.77 µm while that between the middle sensor and right sensor was measured as 11.93 µm. The variance in the results is 6.4 nm due to the imperfect alignment of the shutters and the fixturing of the sensors. The results are presented in Table 6.

Table 6: Expansion of structure

	Structure at 25°C		
	Actual Strain from platform		
	Left sensor module (µm)	Middle Sensor Module (µm)	Right sensor module(µm)
Strain measured by sensor	-7.73	-19.50	-31.43
Actual extension on structure		-11.77	-11.93

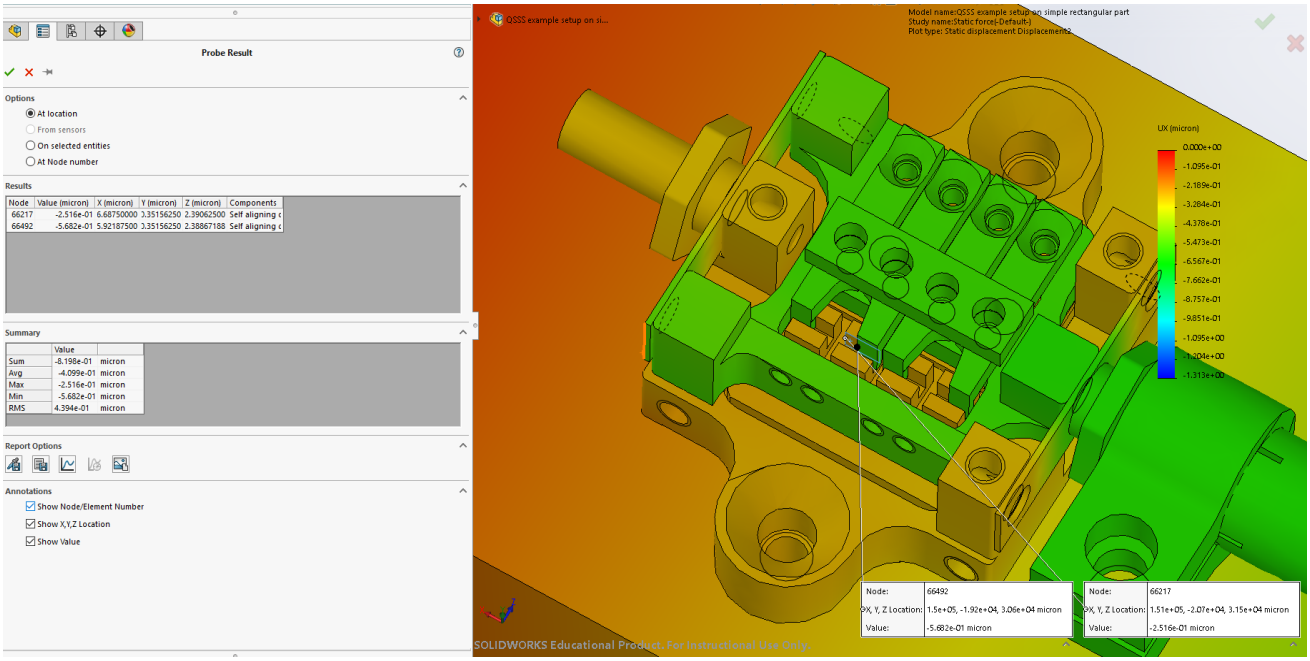

Figure 18: Shutter displacement on left sensor

Figure 18 shows the node data from the surface of a sensor and shutter of an individual sensor module. The difference between the node data on a sensor and the node data on its shutter gives the displacement of the shutter when the sensor module is subjected to a force or strain.

The results of the movement of the shutter relative to the SPM obtained from FEA simulation of the multi sensor module setup as shown in Figure 17 is shown in Table A - 1 and Table A - 2.

Table 7: Static displacement results for multi sensor setup showing measurement of each sensor module

Actual Strain from platform				
	Left Sensor Module (µm)	Middle Sensor Module (µm)	Right Sensor Module (µm)	
|Extension measured by sensor	-7.73	-19.5	-31.43	
Actual strain on structure		11.77	11.93	
Left sensor - Shutter data (µm)				
	Shutter 1	Shutter 2	Shutter 3	Shutter 4
Individual shutter node data	-12.08	-12.52	-12.71	-13.13
Average shutter node data	-12.61			
Left sensor - Sensor data (µm)				
	SPM 1	SPM 2	SPM 3	SPM 4
SPM node data	-6.61	-7.3	-9.57	-9.83
Average node data	-8.33			
Average displacement measured by sensor	-4.28			
Middle sensor - Shutter data (µm)				
	Shutter 1	Shutter 2	Shutter 3	Shutter 4
Individual Shutter node data	-23.13	-23.57	-23.76	-24.19
Average shutter node data	-23.66			
Middle sensor - Sensor data (µm)				
	SPM 1	SPM 2	SPM 3	SPM 4
SPM node data	-18.13	-18.86	-21.13	-21.7
Average node data	-19.955			
Average displacement measured by sensor	-3.71			

From Table 7, the strain on the structure obtained by taking the average displacement measured by the middle sensor module and right sensor module is 11.85 µm.

The average position of the shutters relative to the sensors is calculated. The displacement measured by a sensor is then the difference between the node values of a shutter and node values of the SPM surface to which it is attached. The displacement measured by the left sensor module and middle sensor module is 4.28 µm, and 3.71 µm respectively. The main axial flexure of the left sensor is not connected to a rod hence not measuring displacement in the setup. Therefore, the average strain measured by the left and middle sensor is estimated as 4 µm. This result confirms the application of the sensor for monitoring structural deformation.

The stiffness of a single module has been calculated as $2.45\ N/\mu m$.

When force is applied to a setup consisting of connecting rods as shown in the multi sensor setup, the rod is deformed. This deformation is expected and results from the tensile or compressive stress depending on the direction of the applied force. This deformation results in some systematic losses in the total displacement measured by the sensors. The losses caused by deformation of the CFRP rod in the multi sensor setup were further investigated using FEA. This investigation was performed using a setup of two SPM sensor modules and one CFRP rod. Both sensors were constrained by applying a fixed geometry, and the right module forced to move 1 µm in X negative direction.

The simulation result is shown in Figure 19.

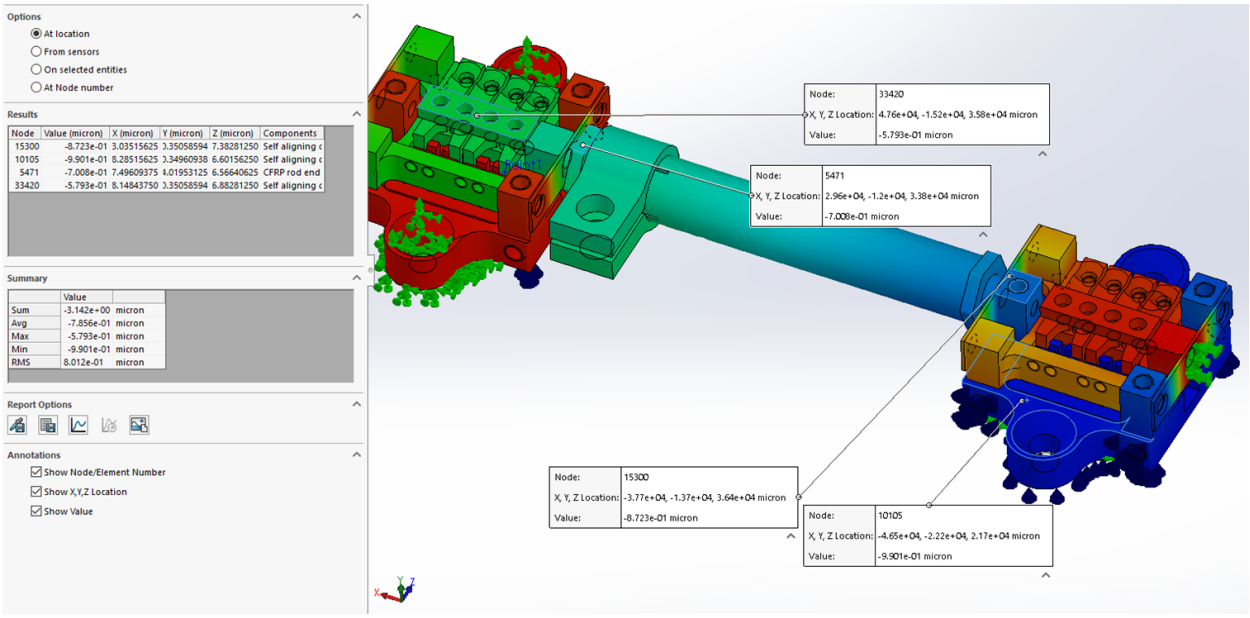

Figure 19: Dual sensor with short CFRP rod

From the result, a loss of 0.87 µm was observed at the rod interface, may be reduced with a lid. Loss due to the strain in the rod results in 0.7 µm at the left module, resulting in shutter displacement of 0.58 µm.
The application of the SPM sensor with carbon fiber connecting rods was validated in an application for monitoring deformation of a structure on the application of heat. The result of the experiments is discussed in section 3.5, and validates the FEA simulation results.

3.5. Strain Measurement System

The existence of various sources of heat on a machine tool creates complex temperature gradients across the machine tool structure and this result in inherent thermal hysteresis. When a structural element bends non-uniformly due to non-linear weight distribution or localised heating, overall strain measurement of the structure does not provide correct results. More accurate results can be obtained by measuring the temperature and strain at multiple locations of the machine tool structure. Multi-strain measurement could be a promising method to achieve the best detection results. Most high precision, high resolution displacement transducers would be too expensive in most applications due to this sort of sensing.

The application of the sensor method for monitoring structural deformations will be investigated by using a suitable connecting rod to create a strain measurement system that can perform direct measurement of the deformation within the structure of a machine tool.
The proposed arrangement consists of a frame made of carbon fibre reinforced plastic (CFRP) rod and the SPM based sensor module to perform real-time structural deformation monitoring. The very good qualities of the sensor reported in [48]include:

- Excellent resolution
- Small size, even with quad sensor set-up
- Ultra-low cost
- Simple signal conditioning

These features make it a unique sensor and suggest its suitability for machinery with relatively rigid structure such as CNC machine tools.
It should be noted that the new sensor design took a long time to manufacture therefore a much-simplified holder and shutter, that could be made using manual tools, was used for testing the strain measurement idea. This used a simple piece of aluminium with edges of the shutter filed until the

signal from the four SPMs was similar. This arrangement, including the bracket to mount to the test rig described in the next section, is shown in Figure 20.

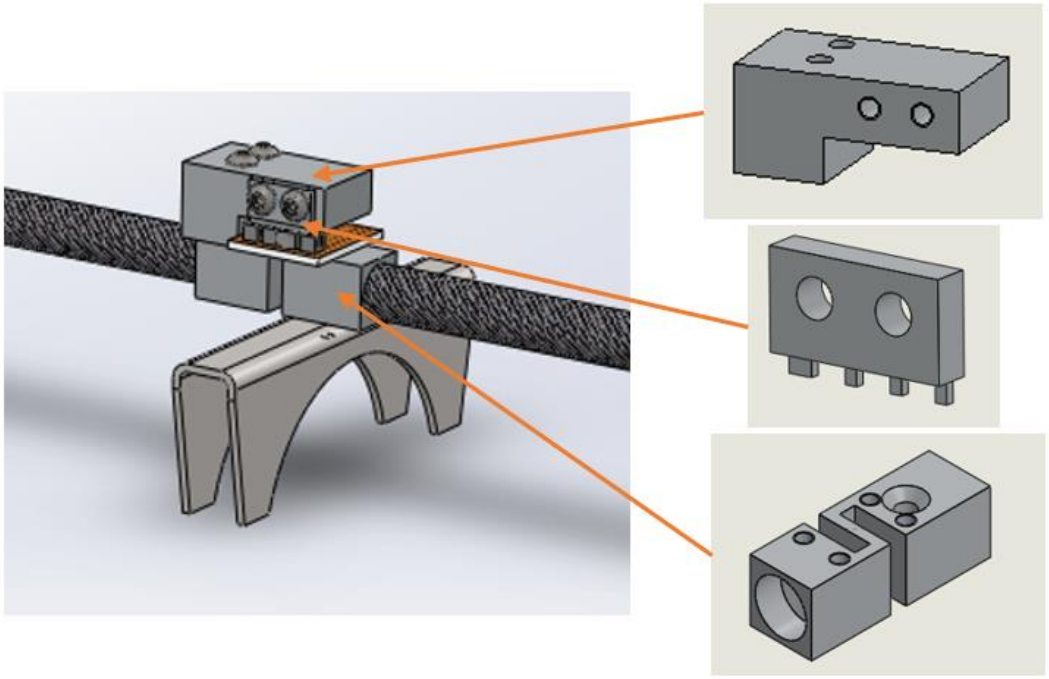

Figure 20: Preliminary bench testing sensor housing

3.5.1. Multistrain Experimental Setup

Deformation of a structural element such as elongation or bending needs to be measured using the new displacement sensor with suitable reference rods fixed to the structure as shown in Figure 21. This forms a rectilinear strain sensing frame the size and spatial resolution of which depends on the lengths of the connecting rods and the number of sensors. The structure being measured consists of three steel bars; a top bar and two side bars, all joined together to create a strong triangular section frame. This test rig enables controlled excitation of either thermal effects or mechanical bending and mounting of additional sensors (laser interferometer) for comparison/validation.

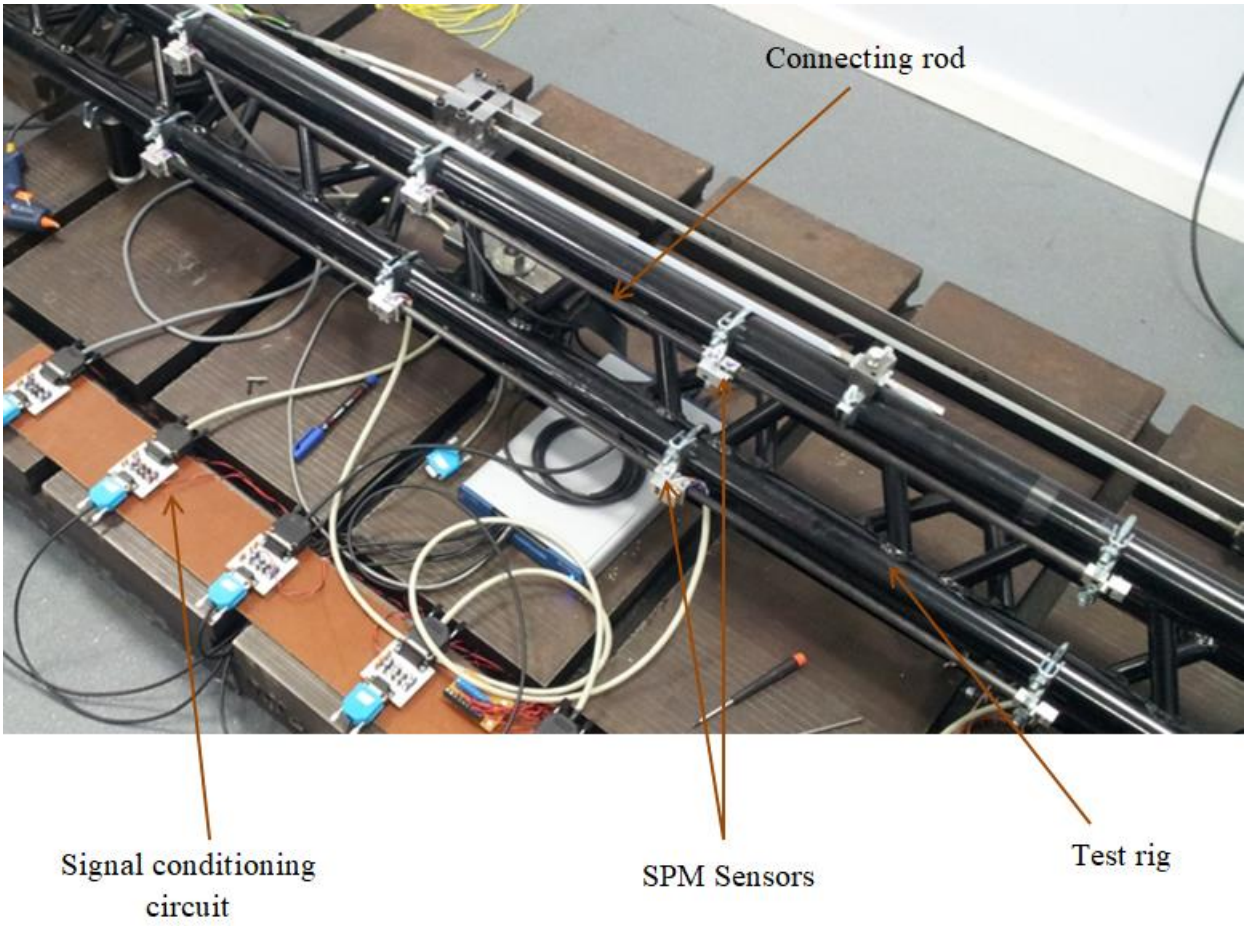

Figure 21: Rectilinear strain sensing frame

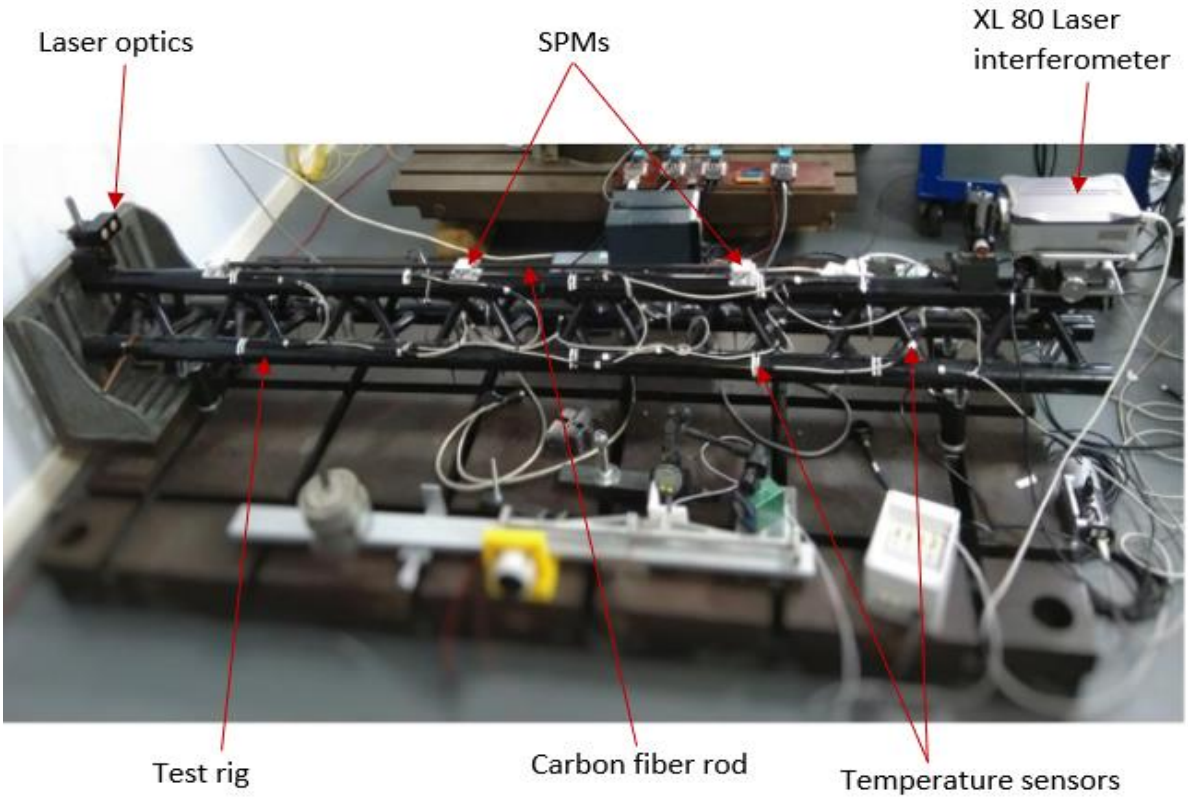

Figure 22: Rectilinear strain sensing frame with interferometer

The CFRP rod is used to transfer the small distortion between the two anchoring points of the rod and the sensor head. The range of the sensor therefore only needs to be sufficiently large to measure this displacement caused by the strain between the two points. The measurement range of the sensor from [48] is stated as 20 micrometres in the linear range and 60 micrometres full-scale, which can be used if calibrated. By applying the sensors on a structural member in stages to detect localised distortion, the magnitude of the localised elongation will be within the range of the sensor. For this experiment, the sensor was used only in the linear range.

The test setup comprises of four (4) SPM sensors mounted on the test rig, a Renishaw XL 80 laser interferometer as reference, and unidirectional CFRP rods (10mm diameters) used as the point-to-point connector.

The test rig covers a length of 2 metres, and the SPM sensors were mounted to cover 1.8m (3 sets of 600 mm rods). To monitor the temperature of the structure, fifteen (15) DS18B20 temperature sensors were attached to the structure at equal distances. The temperature sensors were attached in such a way as to cover the length of the test bed. The key performance parameters of the DS18B20 temperature sensors include:

- 9 bits to 12 bits programmable resolution
- Temperature range of -55 ºC to +125 ºC

- Communicates over a 1-wire interface which allows it to communicate with a microprocessor using only one data line.
- Each sensor has a unique serial code making it possible to connect several DS18B20 sensors on one 1-Wire bus.
- Does not require any external components e.g external power supply

It should however be noted that the data from the temperature sensors in Figure 22 was not used as part of the strain sensing framework. It was only used as informative data to monitor how the structure deformed in response to temperature change. It was not used for drift compensation. Throughout the thesis, the laser interferometer was the reference for all measurements.

The electric circuit is powered by a stabilized Farnell L30-2 power supply, while the output from the sensing head is fed into an analogue to digital converter. A snapshot of an in-house developed visualization software [78] created in LABVIEW is shown in Figure 23.

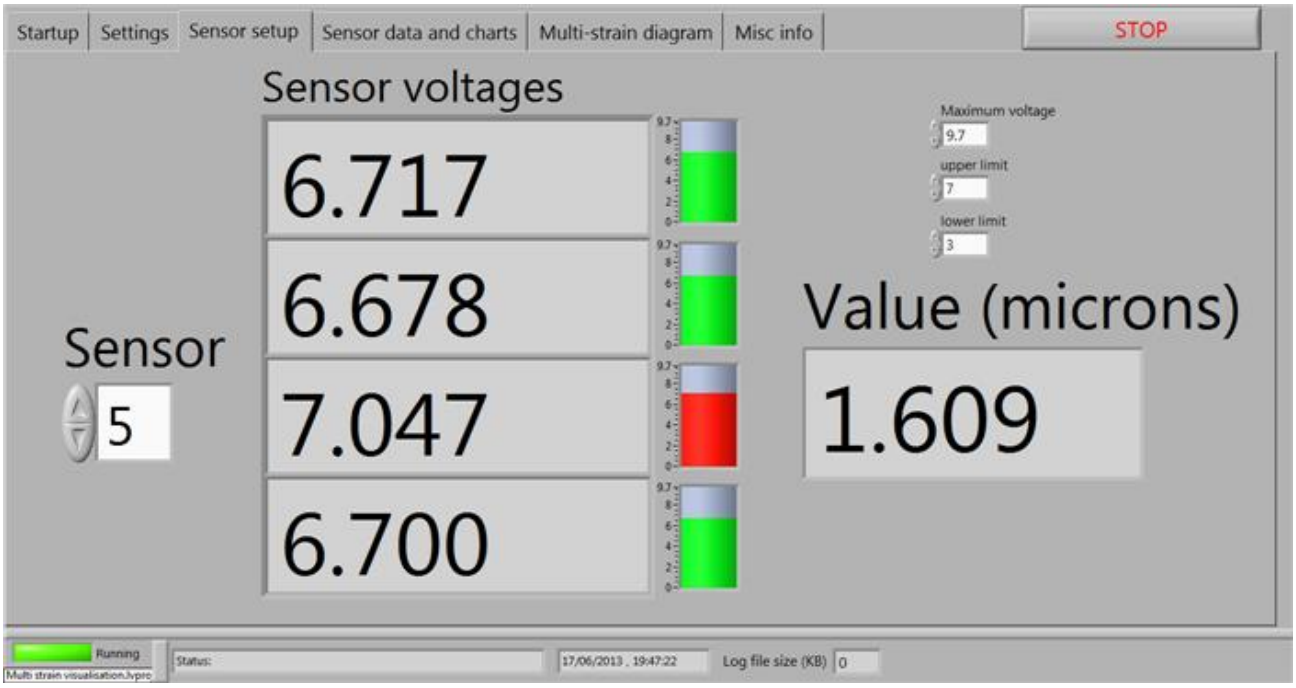

Figure 23: LabView visualization software for strain framework setup

3.6. Experimental Tests and Results

The first test used a modified soldering iron and copper ring around the top bar of the frame to induce localised bending. Figure 24 shows a thermal image of the heat distribution after about 30 minutes of heating. There was no target temperature, just a significant gradient between the top and bottom structural members to cause measurable bending. The heater was turned on for 30 minutes, turned off for 20 minutes then turned on again for 20 minutes before finally cooling for the remainder of the test. The SPM sensors were only active on the top bar to be co-located with the laser interferometer reference. The laser reading and the resultant strain from the SPM frame, scaled to account for the rod stiffness, are shown in Figure 25, with the difference being less than 3 µm. In this example, the scaling factor was an estimate based on the aluminium flexure on the clamps but these were manually produced so there is likely to have been variability in the dimensions and therefore the stiffness. A better correlation is used in the subsequent tests.

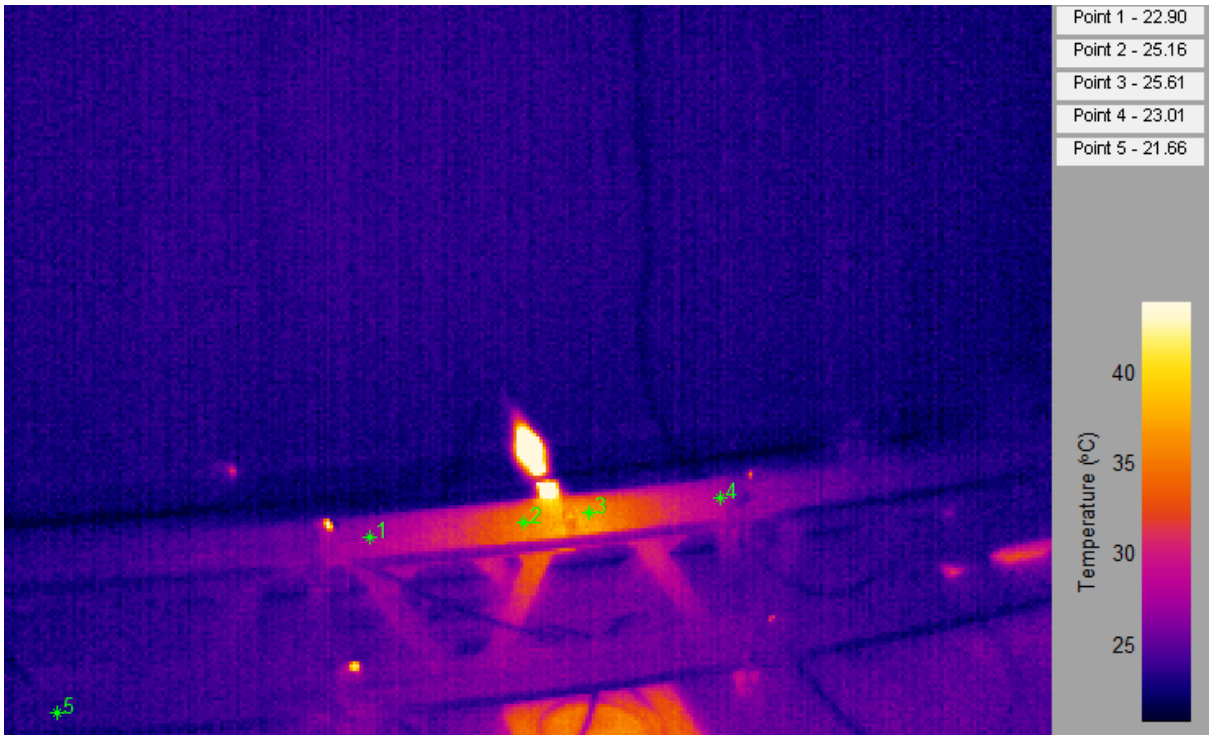

Figure 24: Thermal image of localised heating of the top bar of the test rig

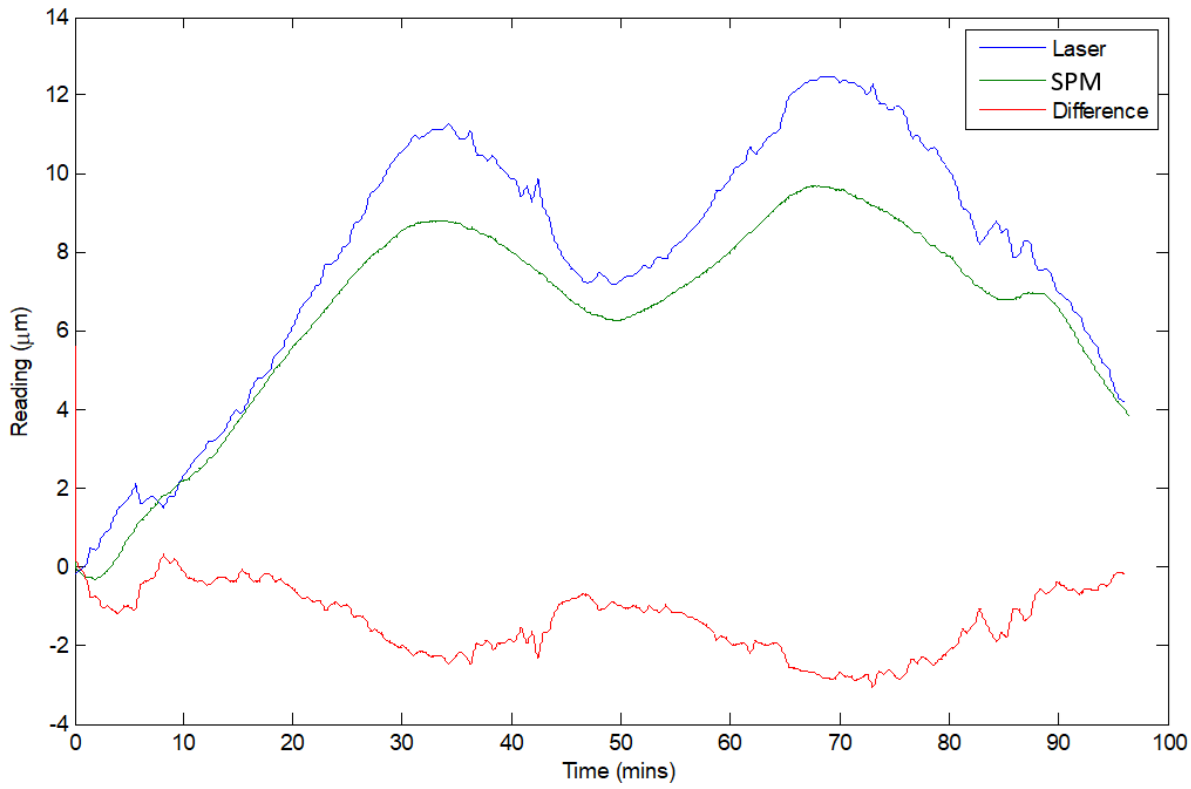

Figure 25: Laser and SPM framework comparison

The second test used a much more varied heating and cooling duty cycle, the results of which are presented in Figure 26. Localized heating of the left-hand bar and top bar of the tribar were investigated, and the result presented as section A and section B respectively. The results of the tests performed at an ambient temperature of 20°C for about 9 hours are shown as section C in Figure 26. The length change as a result of heating is measured by laser interferometer and SPM strain framework

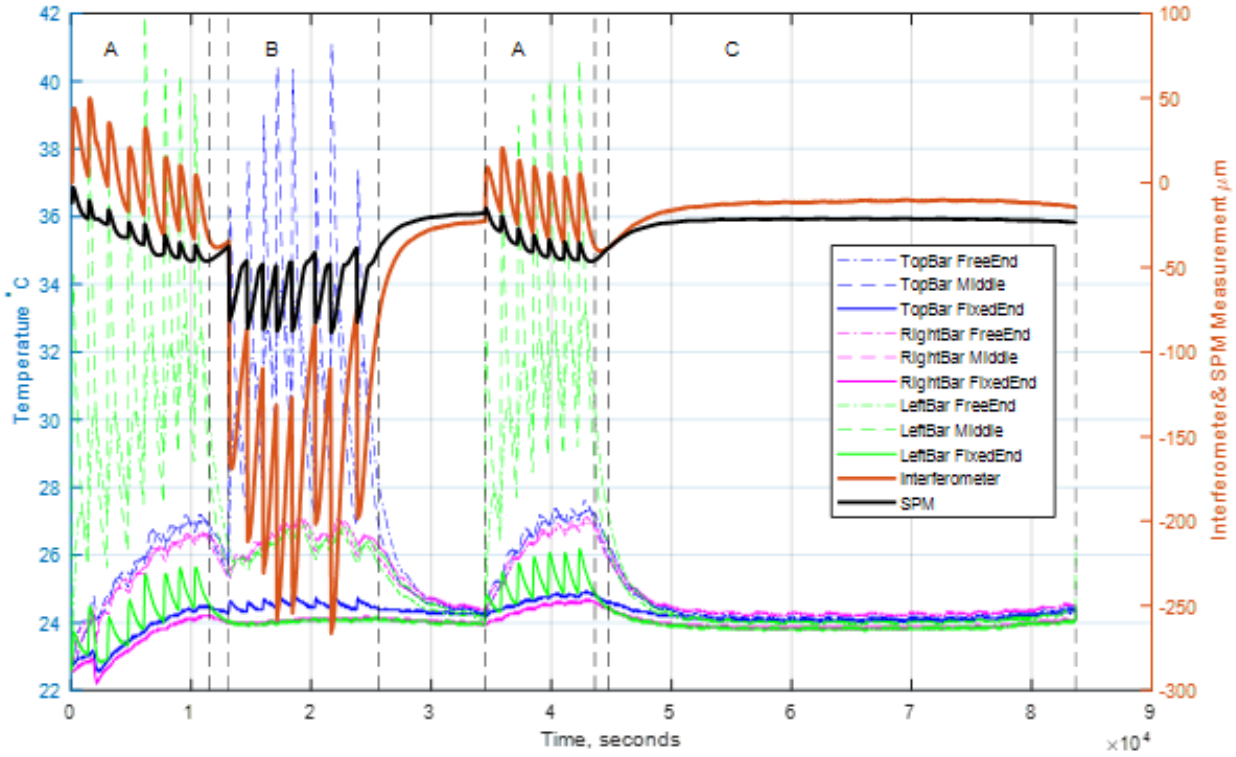

Figure 26: Strain measurement framework thermal test result

Strain on the structure was induced by localized heating of the Tribar using a 2000W heat gun with a pipe that takes the hot air to the middle section of the structure. This was used to increase energy input while maintaining control and preventing radiant heat affecting the sensors or rods. The hot air travels to the fixed end of the structure and as there is no way to exit, bounces back, hence the pronounced spikes. The middle section shows the greatest amplitude because it is the point of heating. The free end has the most interaction with the hot air as it dissipates from the structure. This will take some time hence the gradual increase in amplitude as observed on the plot. Heating of the left bar resulted in readings marked as A on the plot, heating the top bar resulted in section B of the plot and section C shows the plot when no heating was done.

Thermal expansion and bending effects of the Tri-bar structure were recorded by the SPM strain sensor as well as XL80 interferometer as before. Both readings were observed to have a similar relationship, with different magnitude because this is prior to adjusting for the tension/compression losses in the rods.

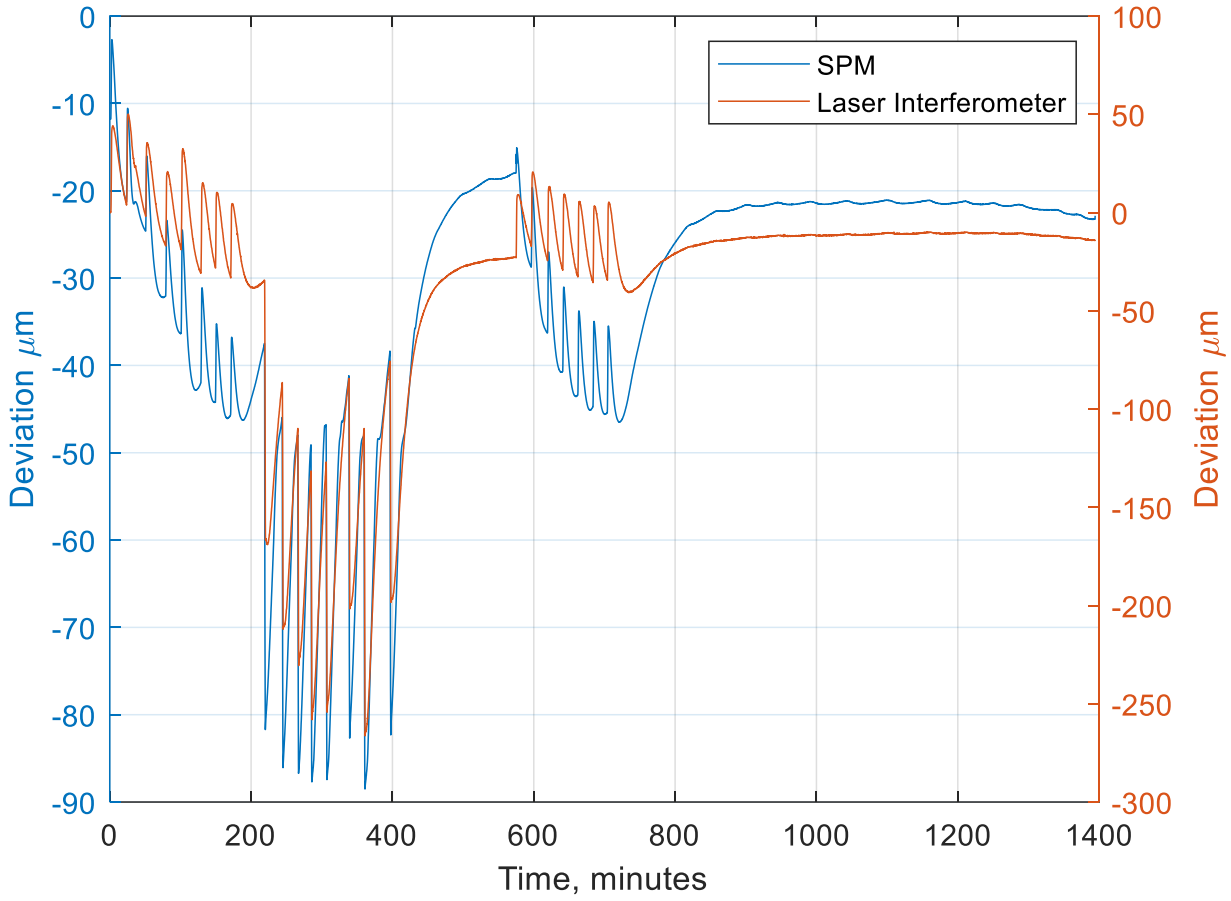

Figure 27: Comparison of SPM and Interferometer

A section of the plot in Figure 27 was selected for further investigation because of the close fit between the laser and interferometer results. This is presented as Figure 28 and shows result of heating of the top bar of the frame.

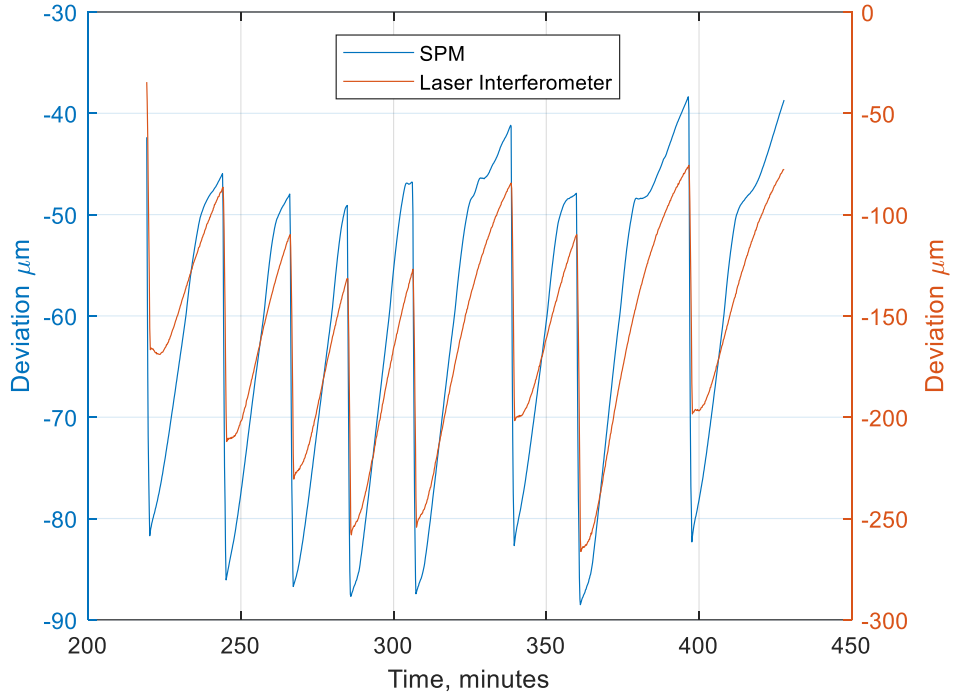

Figure 28: Results for heating of top bar

The difference observed between the SPM and interferometer measurements is caused by the losses in the connecting rods due to its stiffness. Also, the high stiffness of the flexure significantly reduced the amount of deflection on the application of a force, resulting in strain losses. Other sources of error include cosine error and Abbe error due to the difference in the measurement points of the laser interferometer and the SPM sensor.

Cross correlation analysis between the SPM and interferometer measurements was performed with the normalized cross correlation coefficient, $\hat{R}_{xy,coeff}$, given by:

$$\hat{R}_{xy}(l) = \begin{cases} \sum_{n=0}^{N-l-1} x_{n+l} y_n, & l \geq 0 \\ \hat{R}_{yx}(-l), & l < 0 \end{cases}$$

$$\hat{R}_{xy,coeff}(l) = \frac{1}{\sqrt{\hat{R}_{xx}(0)\,\hat{R}_{yy}(0)}} \hat{R}_{xy}(l)$$

where x represents the SPM measurements, y the interferometer measurements, l the lag in the readings. The results obtained can be represented by a Gaussian distribution and show a 90%

correlation coefficient at zero lag. This indicates a strong linear relationship between the SPM sensors and the laser interferometer.

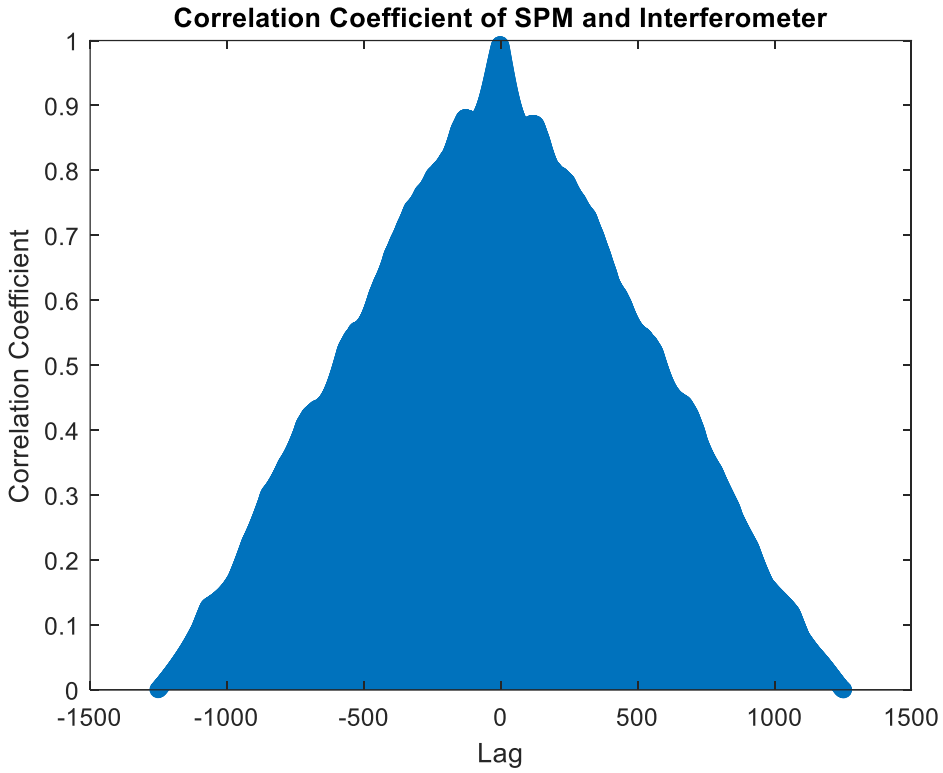

Figure 29: Correlation Analysis of SPM and Interferometer

A linear equation for the interferometer as a function of the SPM measurements was established from the data obtained using the Least Squares Method. This equation is given as:

$$y_{interf} = \theta_1 \times x_{spm} + \theta_2 = 3.046 \times x_{spm} + 26.94$$

Where the 95% confidence interval estimate of the parameters is given by:

$$\theta_1 = 3.046 \ \ (2.968, 3.124) \sim \mathcal{N}(\theta_1;\ 3.046, 0.039)$$

$$\theta_2 = 26.94 \ \ (22.04, 31.83) \sim \mathcal{N}(\theta_2;\ 26.94, 2.4475)$$

Figure 30 shows the plot of the linear estimate of the laser readings from the SPM readings. The results show a normal distribution with a mean value of 3.046 µm and standard deviation of 0.039 µm, with an offset of 26.94 and a residual error in prediction of 1.89 µm.

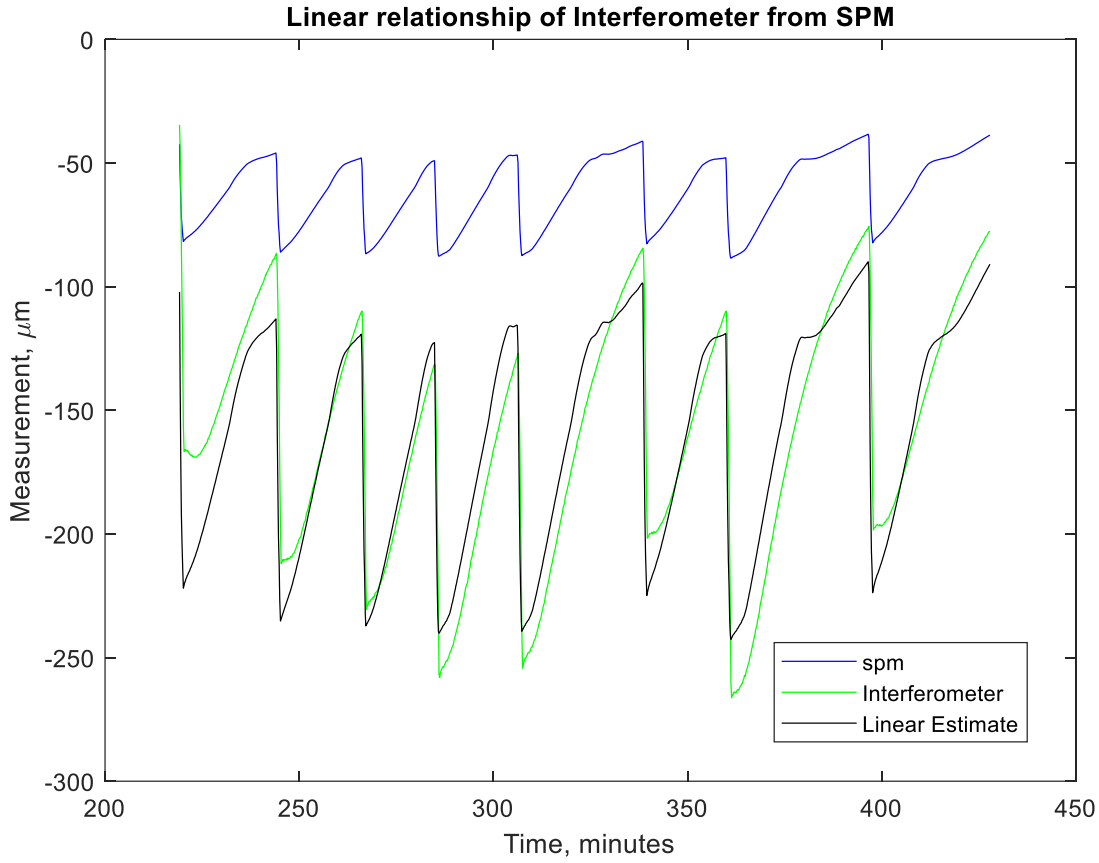

Figure 30: Linear Relationship between interferometer and SPM sensor

In addition to the error sources explained under Figure 28, the measurement results are impacted by the imperfect alignment of the shutters for pairwise clustering. However, this is practically impossible to achieve. All these error sources resulted in significant loss of the strain measured by the SPM sensor.

There is significant challenge during assembly to align all the sensors close to the center of their range to make the most of the linear regions in the outputs. The KRB011 SPM sensors are soldered onto the circuit board in a way that guarantees good alignment. However, it is not sufficiently accurate when combined with the shutter arms to get the equal voltage output at the nominal position. Given the high sensitivity of the sensor, individual adjustment is required with very fine control to achieve straight alignment.

3.7. Summary

For the strain sensing frame, the principle of the novel sensing head has been shown to be effective for measuring strain. The results from investigations reveal that 40% of the structural strain was captured by the sensor due to the stiffness of the preliminary flexure design used on the test rig, however the correlation is good at 90% and this is important to enable compensation of the systematic effect of using a flexure design. Furthermore, the tight tolerance of the shutter design makes it difficult and time-consuming to accurately position the shutters for pairwise clustering. This is an important part of the sensor working principle and the new sensor design evaluated in Chapter 4 improves this considerably.

Overall, principal of using a frame connecting the sensors with high sensitivity, small-size, practical configuration and cost-effectiveness were considered suitable for applications such as in distortion monitoring that requires sub-micron resolution. Drawing from the above, further work is focused on manufacturing and evaluating the new design introduced earlier in this chapter, to reduce the errors due to the positioning and movement of the shutter, as well as the flexure system. The proposed modifications and characterisation of the precision machined design is presented in chapter 4 of this thesis. During the detailed evaluation in this chapter, another new design was worked on based on the findings and consideration of the manufacturing challenges. This is described in Chapter 6.

Chapter 4 - Measurement System Uncertainty Evaluation

In this chapter, the apparatus and procedures to determine the key metrological characteristics and performance of the precision machined design of the new sensor introduced in chapter 3 of this thesis is described. Tests were performed to access the accuracy and repeatability of the sensor, and a technique to identify and quantify uncertainties in the sensor based on GUM is presented and used to create an uncertainty budget.

4.1. Introduction

Techniques for reducing and compensating errors are targeted at improving the system accuracy [79]. The error sources are identified, measured, and then their effect in the measurement is reduced. The result obtained is then compared to the result of a more accurate system to guarantee traceability through the process of calibration.

It is important to understand and clearly define the functional and performance specifications of the measurement system being developed when comparing and selecting solutions. However, differences in the understanding of such characteristics result in errors.

Although conventional procedures to determine the performance of optical-based sensors have been reported in [80, 81],

. it is vital to address the reliability of the measurement process and define which measurement results are affected by systematic errors and those affected by random errors.

Calibration is useful to compensate the errors inherent in a system, but not random errors. This means that the measurement result is only an approximation of the exact value of the quantity being measured, and the sensor response should comprise a measurement of these random errors and the uncertainty in the measurement result. As a result, the accuracy of a measurement result depends on detecting and assessing the sources of errors and considering their effects on the sensor output.

While assessment of uncertainty is important, the process is not well standardized, and this makes estimation of the measurements from reference standards difficult. The technique for uncertainty assessment can be summarised as follows.

In the initial stages of the development of a measuring system, a budget of uncertainties can be employed to detect, calculate, and reduce the individual contributions to measurement error. In some cases, as the one presented in this report, the application of innovative design principles can reduce some of the sources of errors and is essential to satisfying the requirements for accurate and precise measurement results.

After the error sources have been identified and quantified, the cause-and-effect relationship is established by the system theoretical model. Then, the positioning task can be optimized, and the measurement accuracy improved through innovative solutions in relation to the verified principal error sources to achieve the most practical and cost-effective solution.[79]. [82].

A general procedure for assessing and reporting measurement uncertainty is available in The Guide to the Expression of Uncertainty in Measurement (GUM) [83]. This has been referred to in several publications such as in [84, 85] but many do not include an uncertainty budget of the detailed evaluation process.

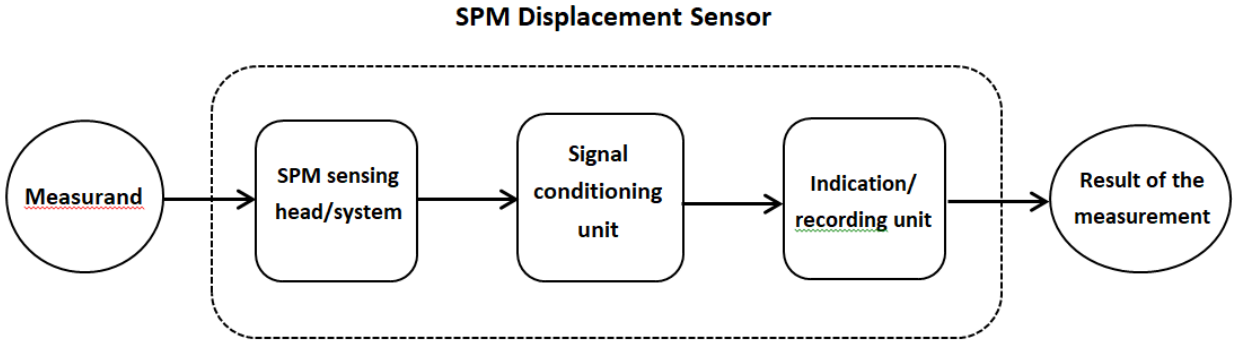

Figure 31: Measurement procedure with SPM displacement sensor

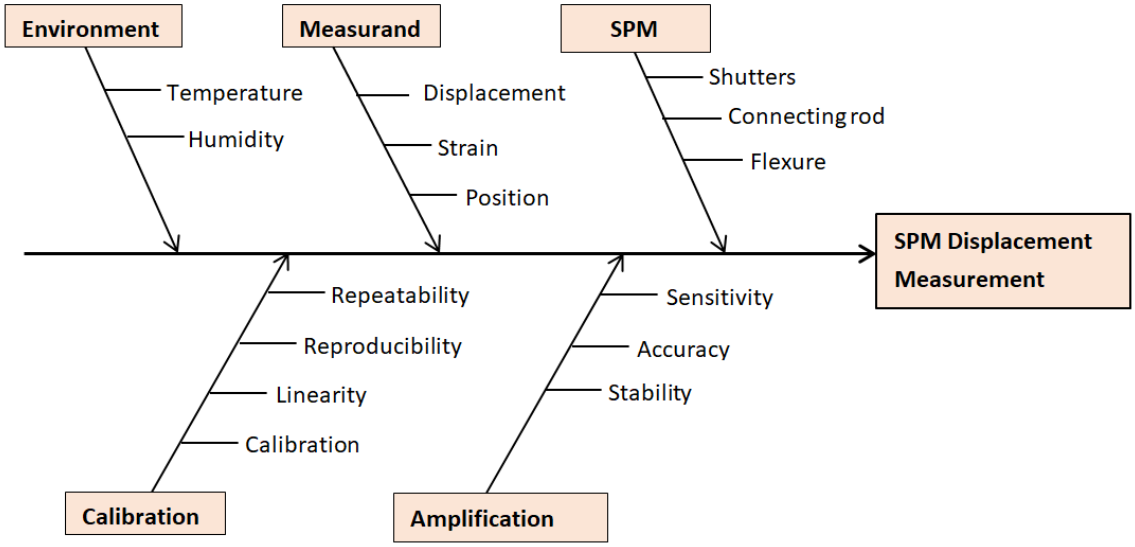

Figure 32: Cause-and effect diagram for SPM sensor

4.2. Characterisation of the Measurement System

A schematic of the setup used to perform a run of experiments to characterise the sensor performance is shown in Figure 33. A photograph of the actual setup is shown in Figure 35. This setup was used to perform experiments to evaluate the repeatability, linearity, and stability of the newly designed SPM sensing head. A comparison experiment between the SPM sensor with a resolution of 21 nm obtained in [48] and the laser interferometer with a resolution of 1 nm was carried out, and the performance of the proposed measurement system was evaluated by analysing the maximum standard deviation.

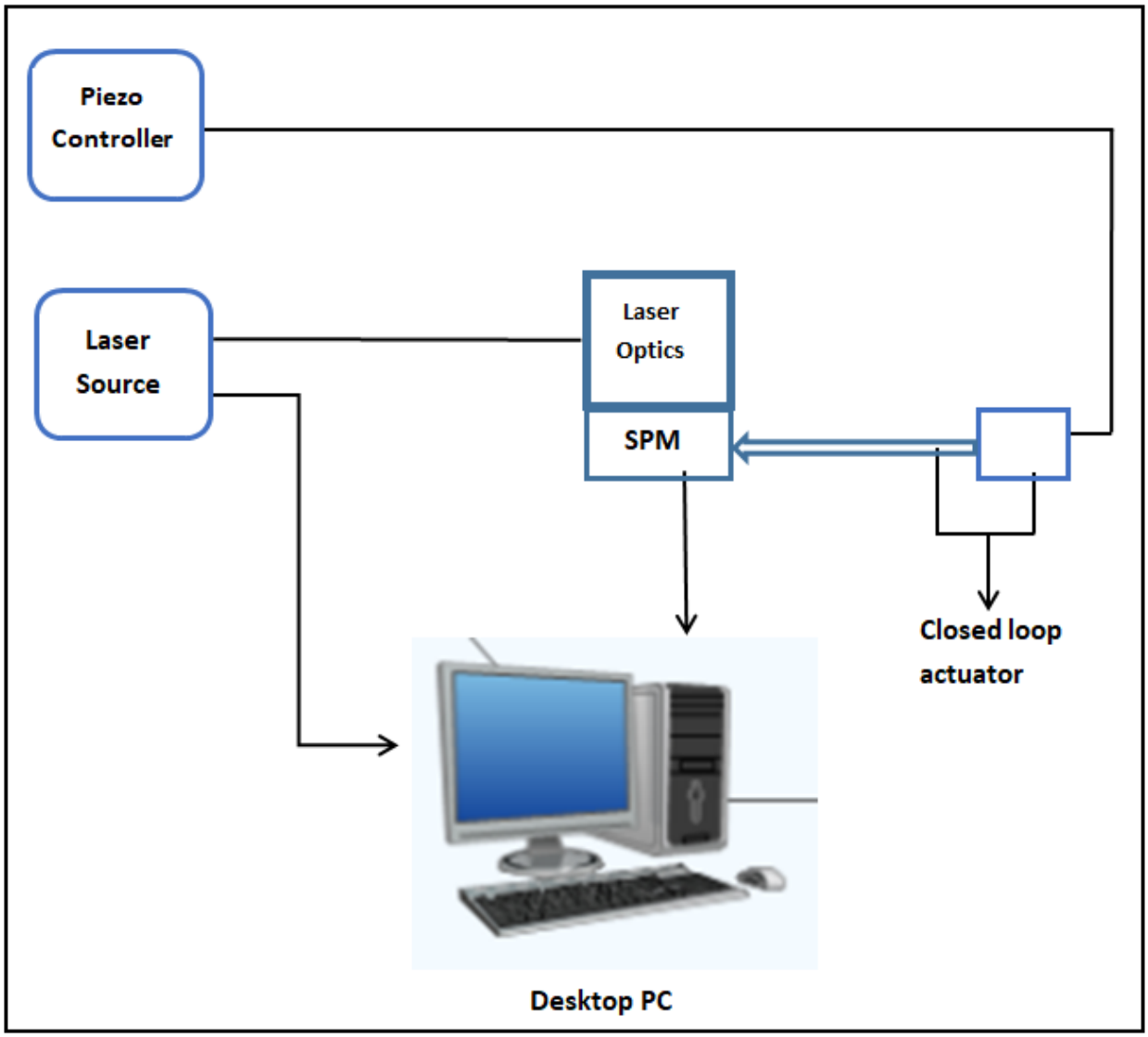

Figure 33: Schematic of setup for sensor calibration

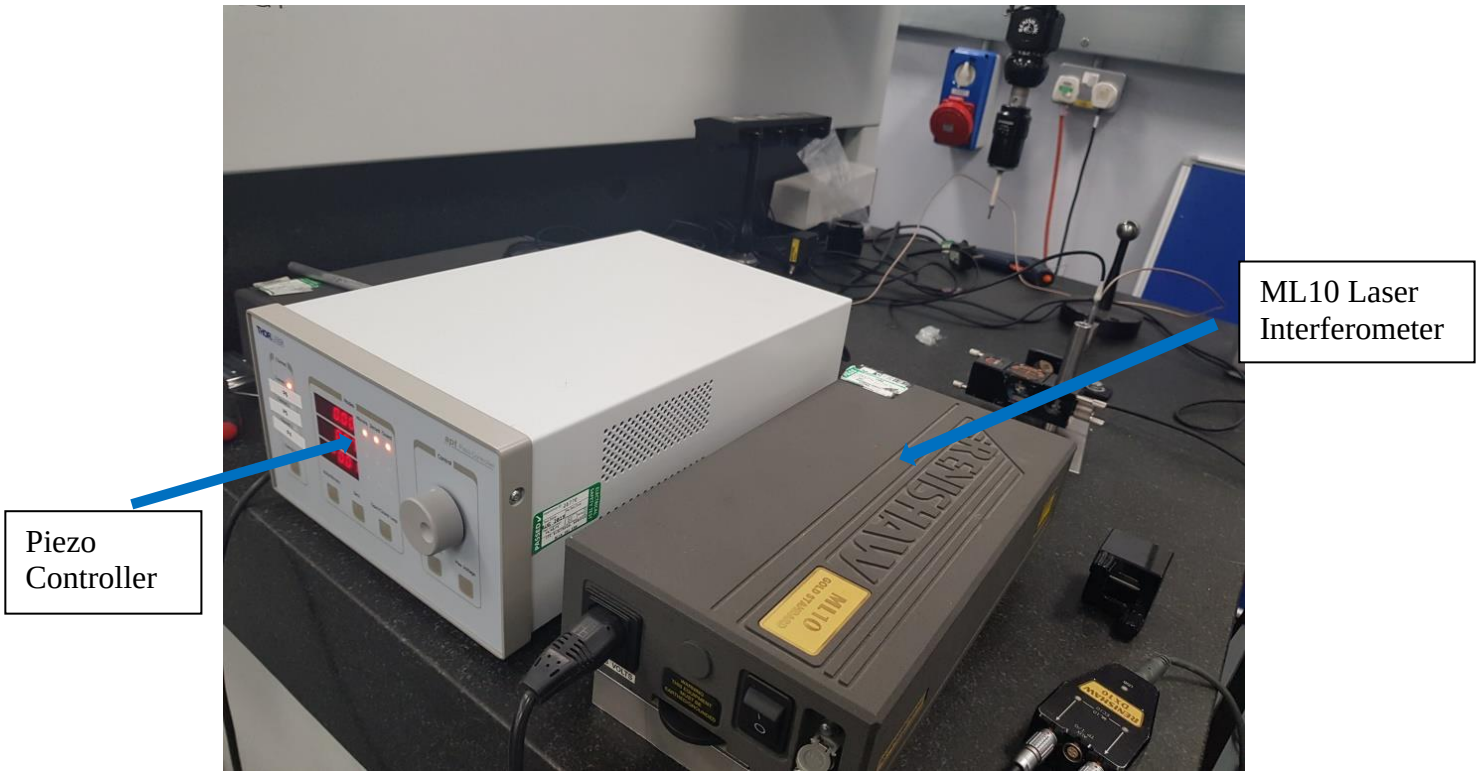

Figure 35: Voltage Self-Calibration Setup

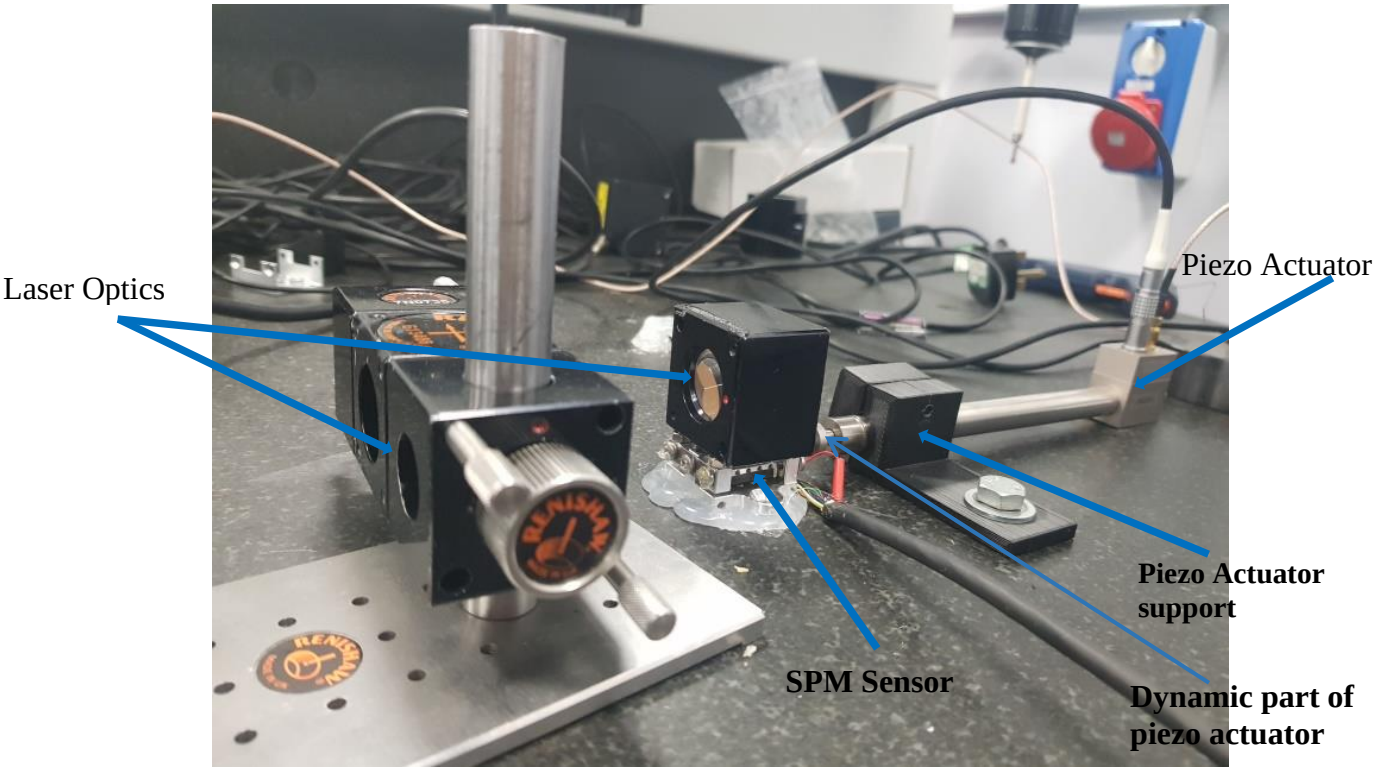

Figure 36: Close-up of setup showing attachment of laser optics to SPM sensor

The test equipment was placed on the granite bed of a Coordinate Measuring Machine (CMM) (Eley Toccata) to provide a reference that is both mechanically and thermally stable. SPM sensing head was mounted on the granite bed and a piezo-transducer (PAZ015) was attached to one end of the SPM. The piezo was used as a driving mechanism to move the SPM module over its calibration range. As the displacements being measured are small displacements, a piezo-transducer is sufficient to make the necessary displacements [86]. The PAZ015 has a feed-back control loop which provided good control for small displacements. The entire setup was located in a temperature regulated room which was measured to be 21 ± 1 °C, for the total period of the tests.

A Renishaw ML10 laser interferometer system was used as the independent reference displacement measurement.

Table 8: Renishaw ML 10 Specification **[87]**

Measurement	0.335m × 0.176m × 0.075m
Linear measurement accuracy	±0.7 µm (with EC10 Gold Standard)
Resolution	0.001 µm
Operating temperature range	0ºC - 40ºC
Frequency Accuracy	±0.05µm (over 1 year period)
Standard measuring range	0-40 metres
Source of Laser	633nm HeNe
Power supply	100-240 VAC, 50/60 Hz
Weight	4.5 Kg

The laser retroreflector optics was attached to the SPM sensing head while one end of the sensor module was attached to the Piezo actuator, thus ensuring that the SPM head experiences the same displacements as the laser optics. To ensure stability of the piezo actuator, a support system was designed in SolidWorks and made from 3D printed material. This minimised the return movement of the actuator as it is attached to the sensor module. Although, the laser system and optics were carefully mounted in a straight line to reduce Abbe and cosine errors, their impact was estimated and included in the uncertainty budget. Also, the movement of the probe was ensured to be normal to the surface of

the CMM bed hence avoiding cosine errors and alignment problems. This is because the piezo actuator probe travels over the surface as it is calibrated, hence the flatness of the surface is important.
Tests were performed by moving the piezo controller over the entire linear range of the sensor head in increments of 3 μm. The result of the tests conducted is discussed in the subsequent sections. The laser interferometer was used in this setup to verify the reliability of the proposed system.

Calibration of the Measurement System

The accuracy of the calibration setup and calibration model is fundamental because it has significant impact on the calibration accuracy. Sensors can be characterized by a particular response function that relates the measured (input) parameters defined as X, with the output parameter defined as Y.

This is expressed as$Y = f(\beta,\ X)$, where β is the coefficient of calibration.
An appropriate response function is fitted to a set of measurement data which consists of the measured signal relative to a reference signal to obtain the calibration curve.
Most temperature and displacement applications show a linear response where the reference value *y* is a linear function of the measured values *x*, given by the expression:

$$y \sim f(\beta, x) = \beta_0 + \beta_1 x,$$

where β_0 represents the offset and β_1 the gradient or gain.

The suitability of the piezo controller for this experiment was verified by comparing the actual readings indicated on the piezo controller digital display with the readings recorded by the laser interferometer. The actuator was displaced in increments of 4 μm. This results in the displacement of the SPM sensor module and the laser optic. Thus, the actual reading displayed on the controller can be compared to the readings of the laser interferometer.
The calibration results are presented in Figure 37.

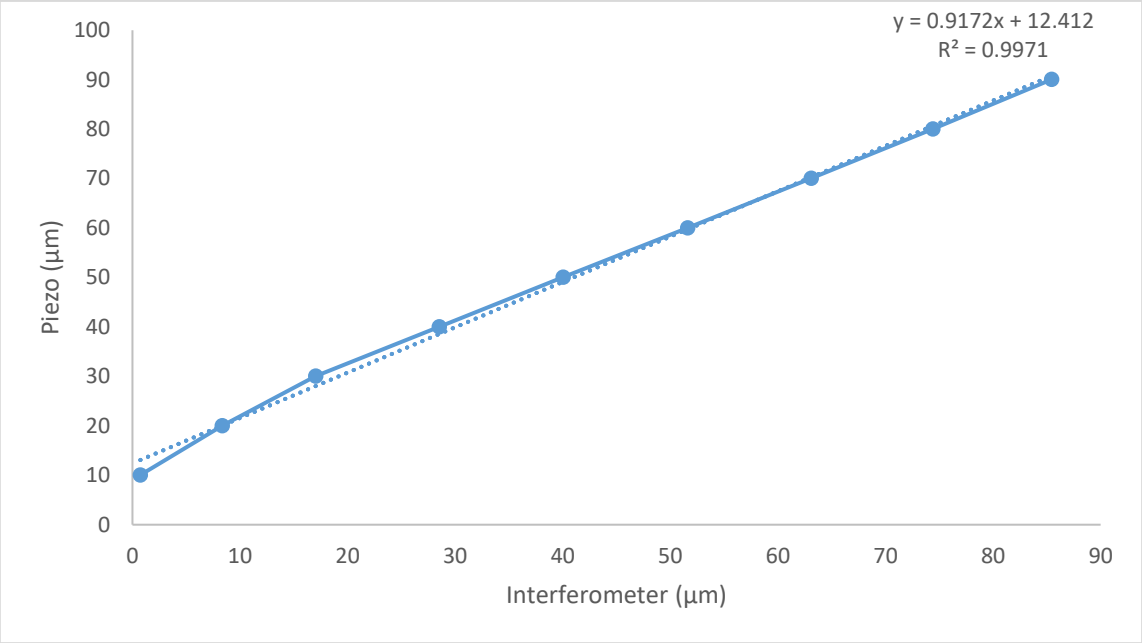

Figure 37: Piezo calibration

From the graph, it can be observed that there is a high correlation between the readings from the piezo controller and the laser interferometer. However, the relationship between the measured results is not perfectly linear in nature and the gradient of the curve is inconsistent over the measured range. This means that the displacements measured by the SPM sensor module and laser do not represent the exact displacements from the piezo controller.

The laser interferometer was used to calibrate the piezo controller and the result is presented in Figure 38.

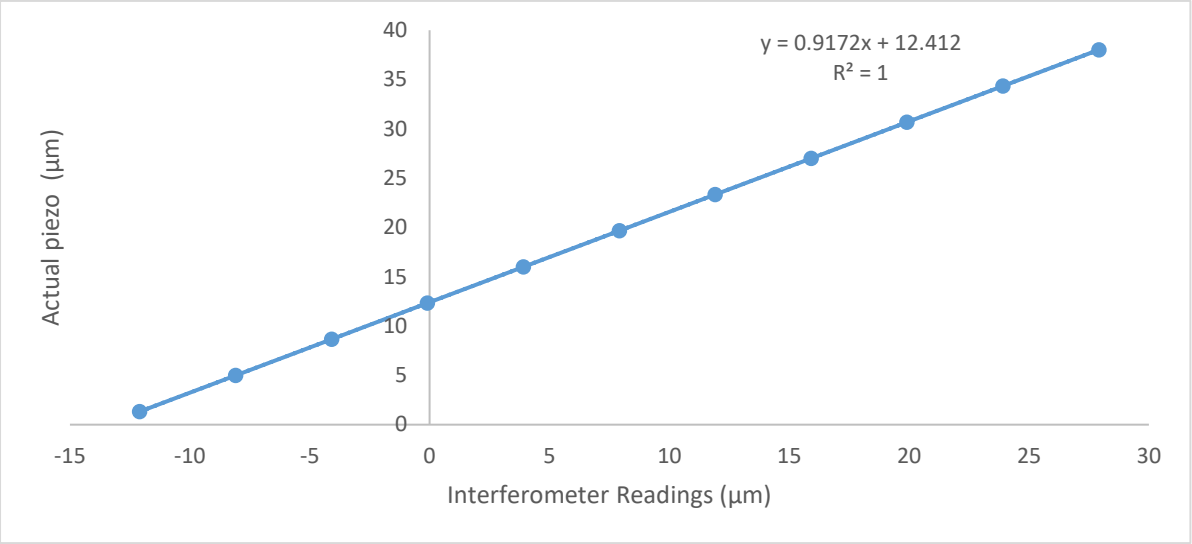

Figure 38: Calibrated Piezo Controller

The calibrated results show a perfect relationship (correlation coefficient, $R^2 = 1$) between the controller and interferometer readings. This gives more confidence in the movements generated by the actuator and the displacements experienced by the SPM sensor module.

4.3 Identification of Error Sources

A. Uncertainties Identification

In each unit shown in Figure 31 systematic and random errors can occur altering the measurement result. Hence, it is important to identify the sources of error and compensate their effects and/or express them in terms of uncertainty. Cause-and-effect diagram is a useful tool to identify and represent the error sources to ensure full coverage and avoid over inclusion of uncertainty components [88-91]. The diagram illustrates the sources (causes) that introduce systematic or random errors in a measurement process which bring about uncertainties in the measurement result (effect). Figure 32 shows a typical cause-and-effect diagram for the SPM sensor.

The design of the SPM sensor module is an important source of uncertainty. In this sense, the type of materials, alignment of the sensors and shutters for pairwise clustering and the flexure design must be considered. For instance, the CTE of the materials used in the fabrication is important as it is sensitive to temperature. Also, misalignment of the shutters can introduce an imbalance in the differential voltage schema, thus introducing errors in the sensor readings. However, the effect of the CTE of the materials was reduced by fabricating the sensor using the same material, aluminium. The connecting

rod can also introduce errors in the sensor response when used to connect a number of sensors to evaluate the displacement of structural parts with varying lengths. Stress on the connecting rod can displace the shutters thus resulting in a false sensor reading.

Another error source is the amplification circuit. The circuit components example resistors can change over time due to usage and aging effects. The sensitivity of the sensor to these must be evaluated. Also, the input to the sensor is a voltage source and any variations in the voltage can significantly affect the performance of the amplification circuit, hence introducing errors to the sensor measurement. Furthermore, calibration processes provide some quantitative information about error sources. The linearity, repeatability and reproducibility of the SPM sensor as well as the calibration standard system are also sources of errors. Finally, the measurand and the environmental conditions can also influence the result of measurement of the SPM sensor. Vibration, temperature, humidity and pressure are factors that must be controlled, and/or measured.

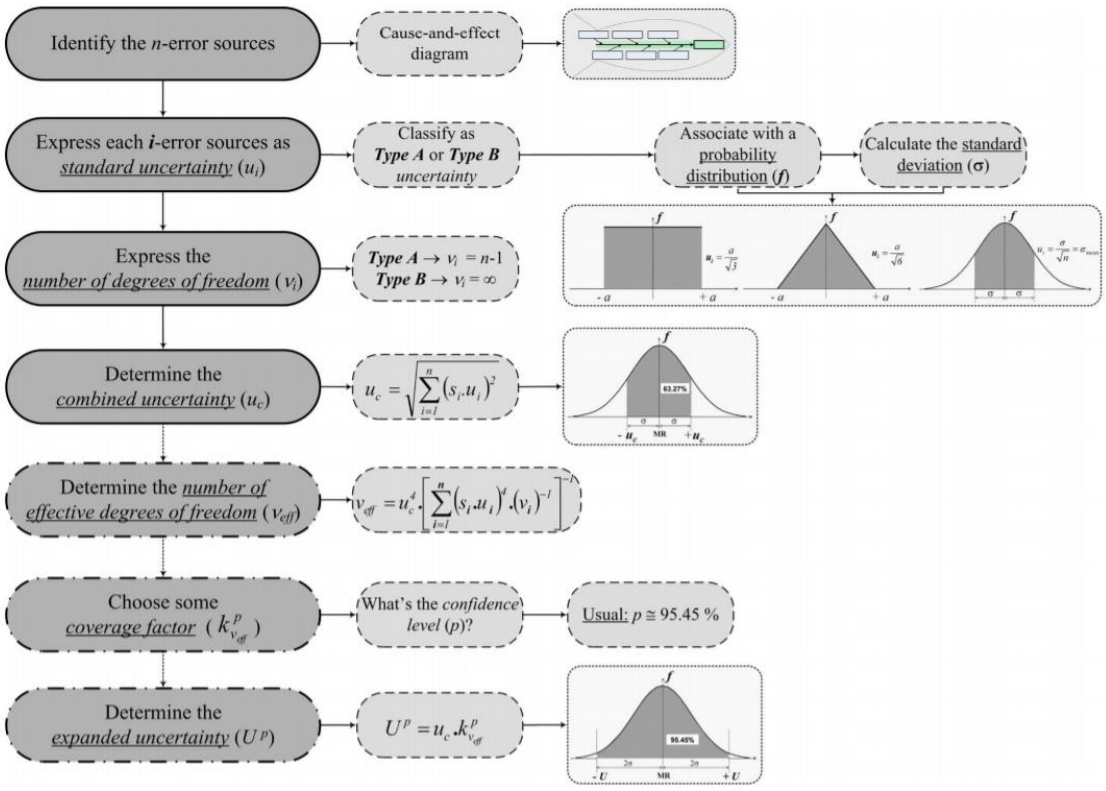

Figure 39: Method to compute uncertainties based on GUM [92]

4.4 Method for Evaluating Uncertainties

General Procedure for Uncertainties Quantification

The impact of each detected source of error must be measured independently from either experimental or published data, and stated in terms of standard uncertainty and its appropriate number of degrees of freedom, according to the GUM [14]. The standard uncertainty, expressed as a standard deviation, shows the measurement result's uncertainty. Type A uncertainty is established by statistical analysis of a collection of data, and Type B uncertainty is derived by any other approach, including subjective or judgement.

Type A standard uncertainty is evaluated using the experimental standard deviation of the mean, whereas Type B standard uncertainty is calculated using the standard deviation of an assumed probability distribution based on scientific judgement, prior test results, specification from manufacturers, information presented in calibration certificates, and expertise or basic understanding. The standard uncertainty is typically a limit value divided by a coefficient in this case. If minimal information regarding Type B uncertainties regarding the probability distribution is available, a rectangular distribution is assumed (the worst case) and the number of degrees of freedom is assumed to be infinite. All identified standard uncertainties are combined to obtain the combined standard uncertainty and evaluated in terms of the variances and covariances of the measured quantities.

An uncertainty budget for the SPM sensor was also established by first identifying the significant contributing elements of the measurement procedure, and thereafter quantifying their individual contributions to the overall uncertainty of the measurement. Informed judgements were made to consider what elements contribute significantly to the total error budget and which are insignificant.

The SPM sensor being studied is expected to have the following characteristics:

Linear Range: 20 μm

Resolution: 21 nm

Sensitivity: 0.1648 V/ μm

The following components are identified as significant contributors to the total uncertainty of measurement. These factors were evaluated using a setup consisting of a laser interferometer, piezo controller, and the SPM sensor.

i. Linearity
ii. Uncertainty of repeatability

iii. Uncertainty of stability
iv. Uncertainty due to shutter misalignment
v. Uncertainty in Coefficient of Thermal Expansion (CTE)
vi. Uncertainty due to light contamination
vii. Uncertainty of signal conditioning circuit
viii. Abbe Error
ix. Cosine Error

4.4.1. Linearity

Ideally, sensors for estimating the position of a target are generally designed to give an output that is directly comparable to the measured position. However, in the actual sense, all position sensors are characterised by an undefined offset, nonlinearity and sensitivity which must be measured [93]. Therefore, linearity uncertainty describes the uncertainty associated with non-linear behaviour observed across the range of an assumed linear function.

The Figure 40 shows the characteristic output voltage plot for a capacitive position sensor.

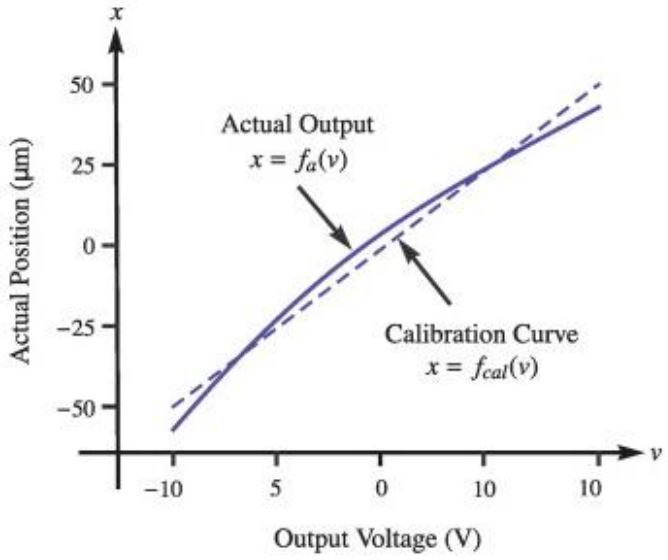

Figure 40: Plot of actual position versus output voltage of a displacement sensor

Experimental results of the relationship between measured voltage and displacement has been shown to be non-linear in nature [48, 63]. The linearity of the improved sensor design (estimated as a percentage error, where a smaller value indicates a better linear response) was evaluated over the linear range of its characteristic curve. This range was chosen because it can be compared to the range of the

original design. A plot of the measured output voltage against displacement was then fit to a linear equation of the form

$$y = mx + c$$

where m and c are constants and will be obtained by using the method of Least Square Regression. By comparing the output voltage with its linear fit, the linearity error can be obtained.

The uncertainty in linearity $U_{linearity}$ is obtained by using the function

$$U_{linearity}(V) = Max\left|y_{observed}(V) - y_{fitted}(V)\right|$$

where $U_{linearity}(V)$ is the linearity error, $y_{observed}(V)$ is the actual output obtained experimentally, and $y_{fitted}(V)$ is the predicted output derived from the calibration equation.

From the data obtained, the maximum deviation (linearity error) obtained from regression analysis is 0.002422 (V), which equates to 0.015 µm. According to [94], it is reasonable to assume a rectangular distribution. Therefore, the standard linearity uncertainty is

$$S_{linearity} = \frac{Max\left|y_{observed}(V) - y_{fitted}(V)\right|}{\sqrt{3}} = \frac{0.015}{\sqrt{3}} = 8.66\ nm$$

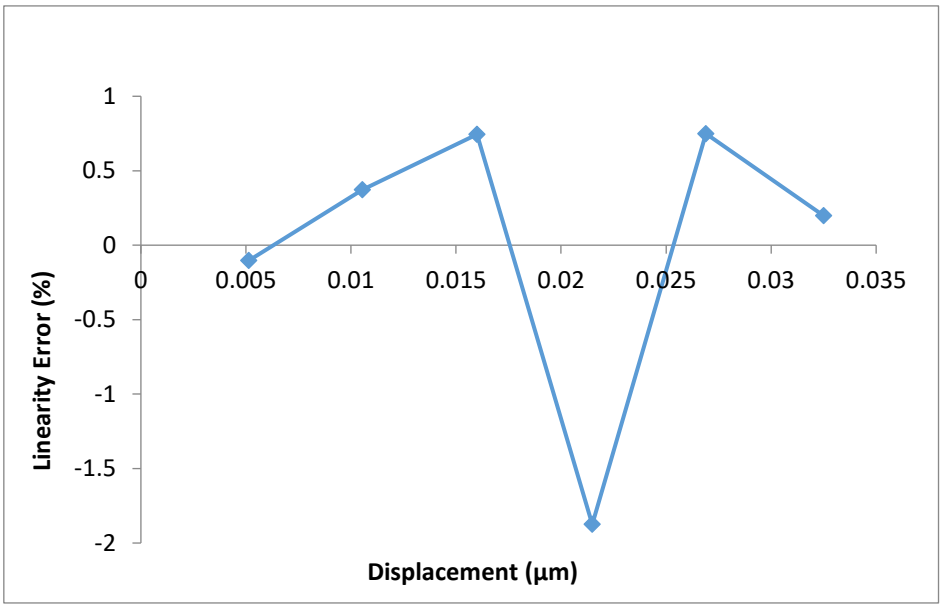

Figure 41: Linearity Error

4.4.2. Repeatability

A repeatability test is performed to evaluate how repeatable the results of a measurement are under a set of similar conditions. That is, it is done using the same method, with the same equipment, unit under test and operator, and in the same location and environmental conditions [95].

To evaluate the repeatability of the measurement procedure, bi-directional displacement experiments were repeated five times in the measuring range of 20 µm, conducted with a step interval of 3 µm. The output value of the SPM head and the corresponding ML 10 laser interferometer reading was logged for targets every 3 µm of piezo actuator displacement.
The standard deviation of the five run of tests was calculated to obtain the repeatability according to ISO 5725. The results, show for an average standard deviation of 18.5 mV for the 7 displacement positions. For a sensitivity of 0.1648 V/µm, this equates to 0.11 µm. This is a Type A uncertainty with four degrees of freedom. The expanded uncertainty for a 95% confidence interval is estimated as 0.22 µm.

4.4.3. Resolution

In [48], the resolution was quantified by measurement of the noise floor and comparing with the sensor sensitivity. The static performance of the sensor was quantified at ten (10) points in its linear range. The standard deviation was reported as 21 nm for a 99.7% confidence level (k = 3). This value for resolution is quoted in this research work because no change was made to the differential principle of the sensor created in [48].
This has a rectangular distribution, and the divisor is $\sqrt{3}$.

4.4.4. Reproducibility

Reproducibility is an evaluation of the variability in a measurement process under different conditions. The reproducibility uncertainty of the measurement process was evaluated by performing a repeatability test and finding the mean. A variable was then changed, in this case, a shutter was adjusted, and a repeatability test was performed on the adjusted setup. It would be time-consuming to teach another operator to perform the tests for reproducibility, and there were no alternative equipment to perform the test the time of this report. Hence, it was easier to change a variable to simulate a different setup and test for reproducibility. The standard deviation of the averages of the two tests gives the reproducibility of the measurement process.

From the tests, the standard deviation for reproducibility was estimated as 0.135 V which equates to 0.81 µm for a 95% confidence level (k = 2). This is a Type A uncertainty with four (4) degrees of freedom.

4.4.5. Light Contamination

Variation in ambient light can also cause misreading of optical systems. In the SPM sensor, the peak spectral sensitivity wavelength of the receiver (phototransistor) is 920 nm in the spectral range of approximately 850–975 nm with 90% relative sensitivity. The peak emission of the emitter is 940 nm, which is close to the peak spectral sensitivity wavelength of the receiver. This means that any variation in ambient light will be detected at the receiver end. To minimize this effect, the gap between the emitter and receiver is designed to be small (1 mm).

To investigate the uncertainty due to ambient light variation on the SPM sensor, tests were performed with the factory lights ON, and OFF. This is necessary to simulate realistic factory conditions as the sensor can be used during the day, and at night or in the dark. The result of the tests for both conditions is shown in Figure 42.

a

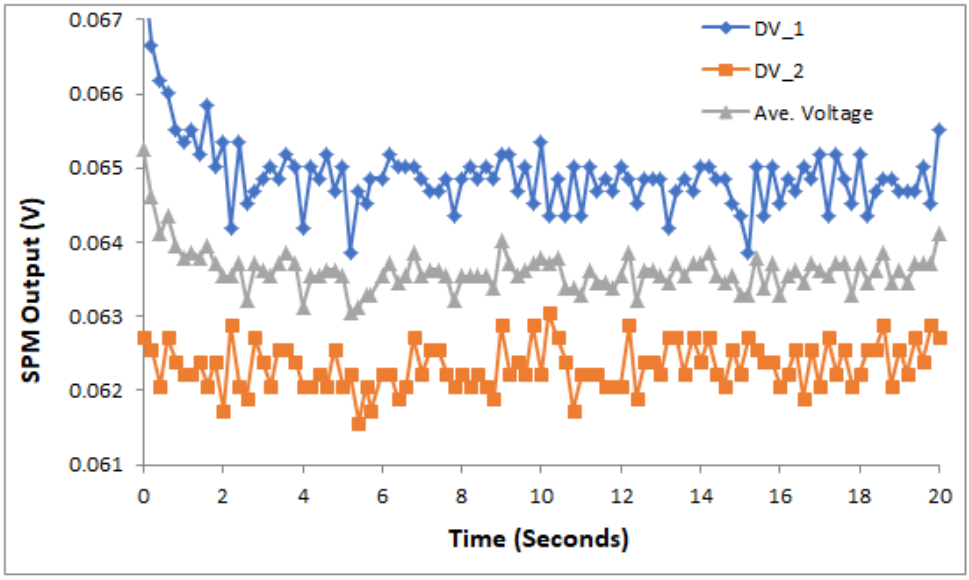

b

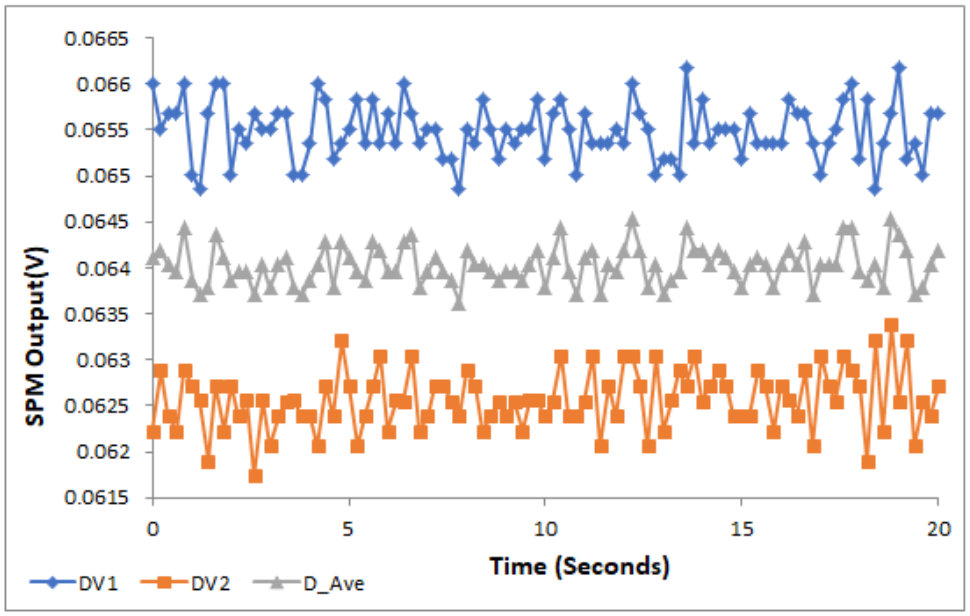

Figure 42: Variation in ambient light conditions; (a) with the lights OFF (b) with the lights ON

A comparison of the results for both conditions reveals that the influence of changes in ambient light is 1 mV which equates to within ± 6 nm. This is a Type A uncertainty with infinite degrees of freedom and an assumed rectangular distribution.

4.4.6. Uncertainty of Temperature Control

The laboratory was maintained at 20 °C ± 1 °C for the duration of the tests. This means that the temperature control is not exact, and the uncertainty associated with the variability needs to be examined. It is expected that the thermometer is accurate to +/- 0.5 °C. The laboratory temperature range is therefore 20 °C ± 1.5 °C.

The SPM is made of aluminium and the commonly stated value for CTE is 23.6 µm/m °C. The following equation will be used to estimate the resultant uncertainty associated with the inaccuracy of the temperature control.

$$\Delta L = L\Delta T\alpha$$

ΔL = the error in length

$L =$ the nominal length of the SPM

$\Delta T =$ the expected error of the thermometer in °C

$\alpha =$ Coefficient of Thermal Expansion

Substituting the values: $\Delta L = 0.046 \times 0.5 \times 23.6\ \mu m = 0.54\ \mu m$

This is a Type B uncertainty with an expanded uncertainty of 0.54 µm. It is considered to have a rectangular distribution because the nature of the data distribution is unknown. The divisor for rectangular distribution is √3. Hence the standard uncertainty is 0.31 µm.

4.4.7. Drift and Stability

The accuracy of a displacement sensor is greatly affected by drift in the sensor output. Hence, to perform measurements at the nanometre level, it is required that the mechanical and thermal stabilities of the sensing system are unchanging at a similar level.

The thermal expansion of a mechanical structure can be described by the relation:

$$L(T) = L_o(1 + \alpha\Delta T)$$

Where ΔT is the change in temperature, α is the coefficient of thermal expansion, L_o is the initial length (before temperature change), and $L(T)$ is the final length (after temperature change).

To investigate the long-term stability of the sensing head, the shutter was kept stationary in a temperature-controlled environment for 6 hours. The DS18B20 digital temperature sensors (±0.5°C accuracy) were used to measure the setup temperature, while the Renishaw XL-80 was used to validate the experimental setup and test results. As temperature is a significant cause of measurement errors, the influence of temperature variation on the sensing head was investigated by increasing the environmental temperature using a heat source for example, a heating coil. The result of the SPM head were compared to the XL-80 readings to estimate the thermal stability of the SPM head as shown in Figure 43.

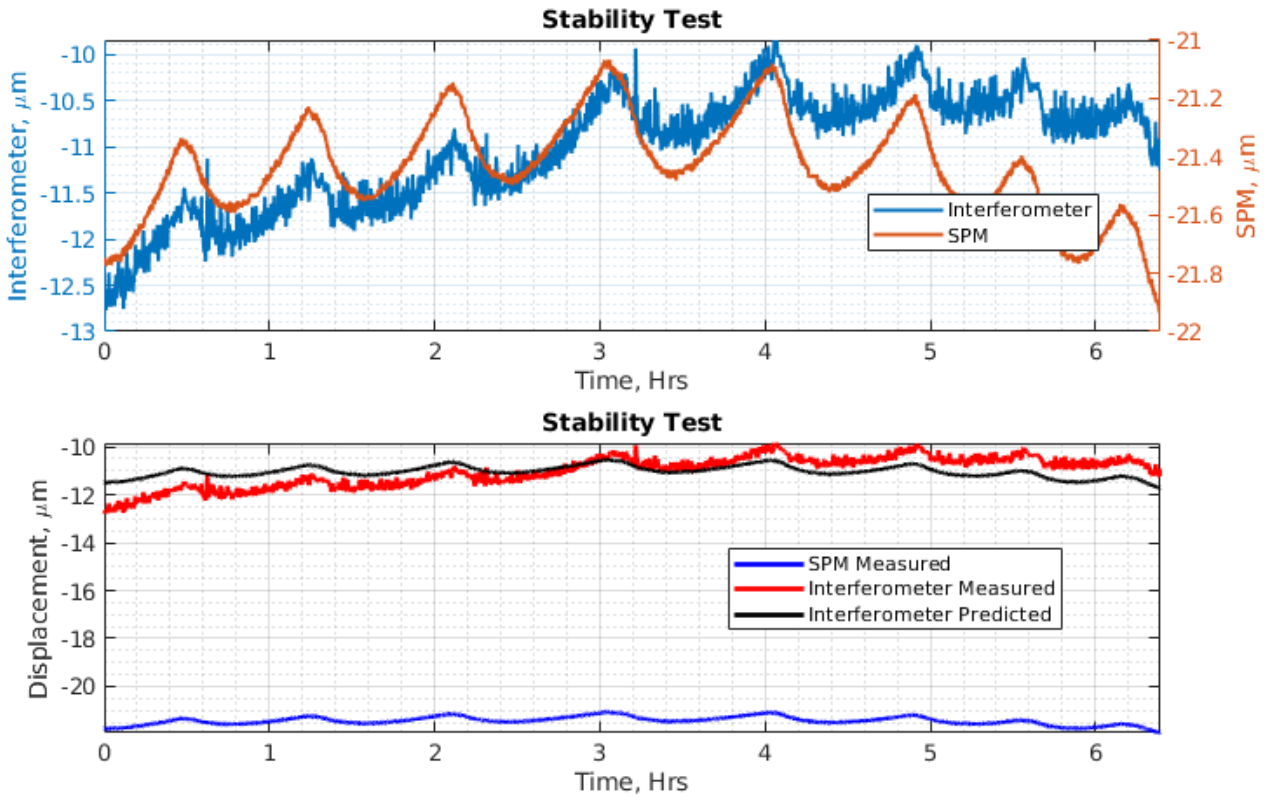

Figure 43: Single SPM sensor stability test

The temperature variations in the environment were measured to be within 0.5 °C. During this time, the SPM head output changes by 0.17 µm, while the XL-80 reading changes by 0.62 µm. The difference in displacement between the SPM head and the XL-80 reading is within 0.5 µm.

4.4.8. Uncertainty of CTE (Coefficient of Thermal Expansion)

The mechanical shutter, sensor base, and shutter head were made using aluminium. The commonly quoted CTE value for aluminium is 23.6 µm/m °C. Even though this value is satisfactory for most engineering calculations, it is not an exact value. When the aim is precise measurements, it is essential to consider the uncertainty associated with the CTE value. We can reasonably assume that this value can vary by as much as 10% or 2.36μm.

We can estimate the uncertainty associated with the CTE using the equation $\Delta L = L * \Delta T * \Delta \alpha$.

ΔL = the error in length

$L =$ the nominal length of the SPM

$\Delta T =$ the deviation from standard temperature in the lab

$\Delta\alpha =$ difference in Coefficient of Thermal Expansion of SPM parts.

$$\Delta L = L * \Delta T * \Delta\alpha = 0.02 * 1.5 * 2.36\ \mu m = 0.071\ \ \mu m$$

This is a type B uncertainty, with an expanded uncertainty of $0.071\ \mu m$ and has infinite degrees of freedom. This calculation is a worst-case scenario, and it is unlikely to happen. Hence, a rectangular distribution is assumed, for which the divisor is √3. The standard uncertainty is thus $0.041\ \ \mu m$.

Coefficient of Thermal Expansion (CTE) of Carbon Fiber (CFRP) rod

The CTE is not a property that is generally available for cured carbon fibre components. However, information about the composition of the CFRP rods could be used to infer the CTE accurately. The rods used in this report are about a 65% fibre fraction [96]. Since carbon fibre has near-zero CTE [97, 98]then the resulting CTE is very low.

The reported CTE which was obtained from [98] and used for the simulation in this thesis is $1.9 \times 10^{-6}\left(\frac{1}{^{\circ}C}\right)$. This is assumed to have a rectangular distribution.

4.4.9. Shutter Misalignment

The misalignment of the shutters may result in error in the calibration accuracy. To study the effect of the shutter misalignment, all four shutters are kept in the adjusted position, and using the interferometer, the sensor is displaced in steps of 4 within its measurement range. The output voltages for the four sensors are recorded and their resulting sensitivities are observed using the method of least square regression. The results of the observations are recorded in Table 9.

Table 9: Uncertainty of shutter misalignment

Sensors	Sensitivity (V/µm)
S1	9.0781
S2	8.3371
S3	5.3256
S4	6.6608

The results show that the average change of sensitivity due to shutter misalignment from principal axis is 0.604 V/µm.

4.4.10. Signal Conditioning Circuit

The signal conditioning circuit components example resistors can change over time due to usage and aging effects. The sensitivity of the sensor to these changes must be evaluated. The circuit used to investigate how the current flow of the phototransistor incorporated by a photomicrosensor is varied by the LED with or without an appropriate forward current (I_F) flow, provided that the ambient illumination of the photomicrosensor is ideal (i.e., 0 lx) is shown in Figure 44.

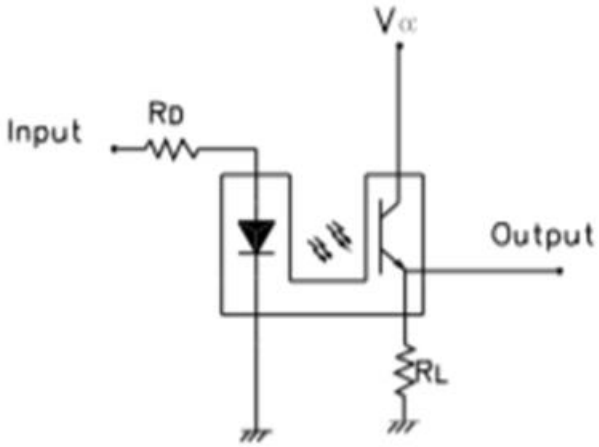

Figure 44: Measuring Circuit for investigating effect of changing limiting resistor

In Figure 44, R_D is a limiting resistor, and R_L is a load resistor. The calculations for the values of the resistors are explained in Section 2.3.2. Photomicrosensors

A variable resistor was used in place of R_D and the resistor value was varied to 410 Ω to simulate a worst case scenario. The output voltage was measured across the resistor R_L for each resistance value and recorded. No significant effect was observed on the output up to 410 Ω. However, the variable resistor burnt out at a resistance value of 450 Ω.

The standard deviation obtained by changing the resistor value using a variable resistor was obtained as 0.11 mV which corresponds to 0.66 nm. The distribution is assumed to be rectangular.

4.4.11 Abbe Error

Abbe error is present in a measuring system when the point of measurement is separate from the actual axis of measurement. In the calibration test setup, the laser optics is placed on the SPM. Thus the SPM measurement is displaced from the laser axis. Therefore, any angular error of the shutter motion will amplify the error of the laser resulting in an error in the measured displacement. The Abbe error must be accounted for in an uncertainty analysis. To do this, the Abbe offset and size of the angular errors in the positioning system must be known. Figure 45 is a sketch of the setup for estimating the Abbe error in the SPM measurement.

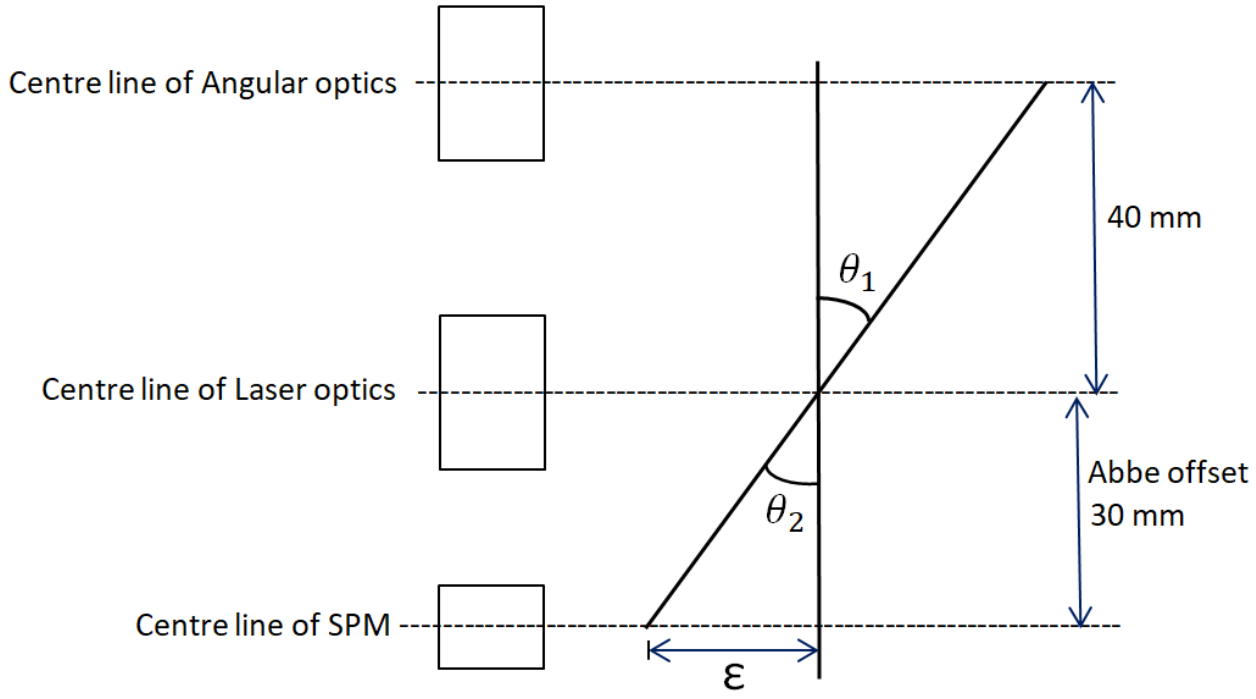

Figure 45: Effect of Abbe Error on SPM displacement measurement

θ_1 is the angular error measured by the angular optics, θ_2 is the corresponding angular error on the SPM shutter motion, ε is the Abbe error, The Abbe offset is the distance from the SPM centre line to the centre line of the laser optics which is placed on the SPM.

Using the piezo controller, the shutters were displaced a total of 20 µm, and the error measured by the angular optics of the laser interferometer, θ_1 was recorded. From the results, $\theta_1 = 0.00163°$. From Figure 45, θ_1 and θ_2 are equal because they are vertically opposite angles.

Using trigonometry, Abbe error $\varepsilon = \mathrm{d}\tan\theta_2$

where *d* is the Abbe offset

$$Abbe\ error\ \varepsilon = 0.03\ \times\ \tan 0.00163$$
$$= 0.85\ \mu m$$

The propagation of the error is assumed to have a rectangular distribution. The standard uncertainty of this value is therefore 0.49 μm.

4.4.12 Cosine Error

Cosine error is the result of an angular displacement between the axis of motion and the axis reference measurement instrument (e.g. laser interferometer). This usually results in smaller displacement measurements.

For the experiment in Figure 36, the cosine error is over the length of the measurement (20 µm), and the alignment of the laser optics. The misalignment angle was measured as 0.216 degrees using an angular laser optics. A schematic of the realization is shown in Figure 46.

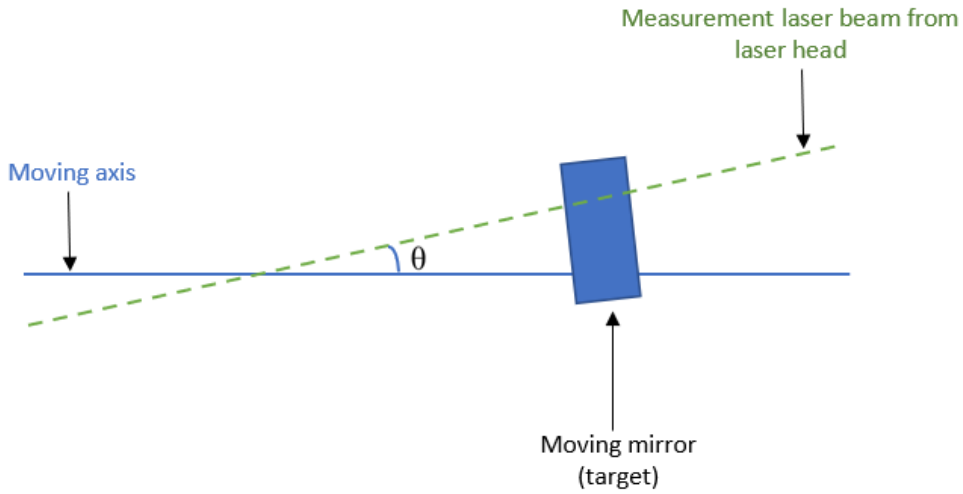

Figure 46: Effect of Cosine Error

The cosine error (Δl_c) can be evaluated using the relation

$$\Delta l_c = l_{opt} - l$$

Where $l_{opt} = \cos\theta \times l$

For θ = 0.216°, $l = 20\ \mu m$, the cosine error is estimated as -0.142 nm.

4.5. Uncertainty Budget

The uncertainty of the measurement system will depend on various factors such as the supply voltage of the circuit, tolerance of the fixed resistors and photomicrosensors.
The combined uncertainty of the measurement system was calculated by estimating the uncertainties of the individual uncertainty components. For a rectangular distribution function, the calibration range of each device is divided by '√3' to convert every rectangular distribution in standard uncertainty. All standard uncertainty components are combined to calculate the combined uncertainty as follows.

$$U_c = \sqrt{(U^2_{(e_{repeatability})} + U^2_{(e_{reproducibility})} + U^2_{(e_{resolution})} + U^2_{(e_{linearity\ error})} + U^2_{(e_{misalignment})} + U^2_{(e_{temperature\ error})} + U^2_{(e_{light\ contamination})} + \dots}$$

Using the above relation, the combined uncertainty was calculated as 2 µm. For a coverage factor of k =2, the expanded uncertainty U is calculated by multiplying the combined standard uncertainty by 2. This results to an expanded uncertainty U = 2 µm * 2 = 4 µm (95% confidence).

The individual standard uncertainties of various components and combined standard uncertainty is presented as the uncertainty of measurement budget and is given in Figure 47.

Uncertainy component	Sensitivity Coefficient	Uncertainty Value	Unit of Measure	Uncertainty Type	Probability Distribution	Divisor	Standard Uncertainty	Variances	Degrees of Freedom (n-1)
Sensor Properties									
Repeatability	1	1.1E-07	meters	A	Normal (k=2)	2	2.2E-07	4.8E-14	4
Reproducibility	1	8.1E-07	meters	A	Normal (k=2)	2	1.62E-06	2.6E-12	4
Resolution of SPM	1	2.1E-08	metres	B	Rectangular	√3	1.212E-08	1.5E-16	∞
Linearity Error	1	1.5E-08	meters	A	Rectangular	√3	8.661E-09	7.5E-17	∞
CTE of carbon fibre rod	1	1.9E-06	meters	B	Rectangular	√3	1.097E-06	1.2E-12	∞
Misalignment of Sensors	1	2.3E-08	meters	A	Rectangular	√3	1.328E-08	1.8E-16	∞
External Influences									
Temperature Error	1	1.63E-07	metres	B	Rectangular	√3	9.41E-08	8.9E-15	∞
Cosine Error	1	1.42E-10	metres	A	Rectangular	√3	8.20E-11	6.7E-21	-
Abbe Error	1	8.50E-07	metres	A	Rectangular	√3	4.91E-07	2.4E-13	-
Drift in resistor values	1	6.60E-10	metres	A	Rectangular	√3	3.81E-10	1.5E-19	-
Reference Standard	1	1E-08	meters	B	Normal (k=2)	2	5.00E-09	2.50E-17	∞
Influence of Measured Object Time Effects									
Drift of SPM	1	2E-07	meters	A	Normal (k=2)	2	0.0000001	1E-14	-
Light Contamination	1	6E-09	meters	B	Rectangular	√3	3.464E-09	1.2E-17	-
							Sum of variances		4.14E-12
							Combined uncertainty		2E-06
							K		2
							Expanded Uncertainty		4.07E-06

Figure 47: Uncertainty budget for measurement system

From the uncertainty budget, the most significant contributors are uncertainty due to CTE of connecting rod which in this case is a carbon fiber rod and uncertainty of temperature control. The contribution to uncertainty of the connecting rod can be reduced by using ultra-stable materials. Thermal effects have been reported to be a major source of errors in a measurement system. The total uncertainty can be reduced by performing the experiments in a stable environment.

4.6. Summary

In this chapter, a strain measurement system is described and the level of uncertainty is determined. Evaluation of uncertainty contributors shows that the developed measurement system can measure strain in the micrometre range with an uncertainty of 4 µm.

The calibration is carried out using a simple and reliable procedure that may be set up in a laboratory setting. The performance of the proposed measurement system was evaluated by analysing the maximum standard deviation of a comparison experiment between the SPM sensor with a resolution of 21 nm and the laser interferometer with a resolution of 1 nm. Small displacements to the sensor and laser optics were well controlled by a PAZ015 piezo controller and actuator with a feed-back control loop.

A strong correlation (R-squared of 0.98) was observed between the predicted and observed results. The standard error of the results is 0.88. The repeatability of the sensor is 0.22 µm. The sensor performance is affected by ambient conditions, but the small gap between the emitter and receiver, a differential voltage cancellation method, and the introduction of a lid reduces the effect of light contamination to within ± 6 nm. The significant contributors to uncertainty of the measurement system are due to thermal effects. However, these can be compensated.

The performance of the sensor can be affected by changes in signal conditioning circuit, and power supply variations. Individual movements of the shutters due to vibrations for example can cause false sensor readings. Thus, a technique for in-situ detection and calibration for the effect of improper shutter movements, for example is described in chapter 5. This is important especially for embedded applications where it is difficult or costly to access the sensors.

Chapter 5 – In-situ Voltage Calibration Technique

5.1 Introduction

This chapter describes the development of a calibration technique that reduces the impact of the errors sources in the newly designed and manufactured sensor after preliminary frame testing in chapter 3. When the sensors are installed for structural monitoring, vibrations can result to individual shutter movements. Also, aging of circuit components like resistors, and variations in supply voltage can cause false sensor readings. This can impact the calibration accuracy and affect downstream circuitry, especially in embedded applications. The proposed technique is capable of detecting and correcting the effects of these error sources on the sensor performance.

Displacement is a fundamental variable in many industrial applications which must be measured and controlled. There is a direct relationship between displacement and other related parameters such as distance, strain, distortion, vibration, deformation and thermal expansion. Hence displacement sensors can be used to measure several measurand [51].

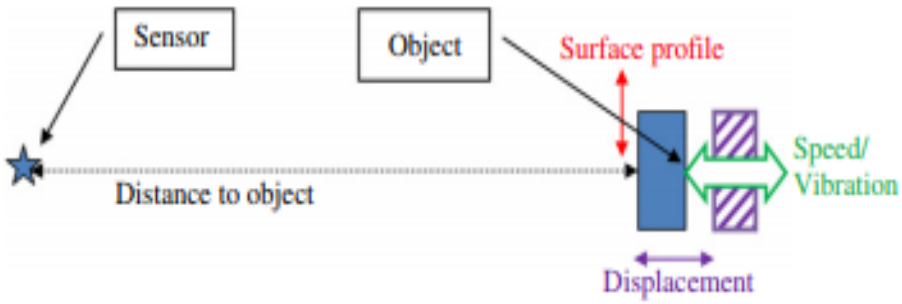

Figure 48: Relationship between distance, displacement and related parameters [51]

Displacement measurements are extremely important in dimensional metrology and could be conducted using various sensors. Various types of displacement sensors measure different physical properties [99]. High accuracy measuring instruments such as those described in [99] are required to accurately measure a workpiece. The accuracy of such a measuring instrument can be enhanced through improved design consideration and by placing it in a temperature-controlled environment. This approach is known as error avoidance. However, error avoidance techniques do not fully guarantee accuracy of measuring instruments, and even where it is feasible to implement, it increases the cost of the measuring instrument. Error compensation techniques can overcome this drawback. Several techniques are available for compensating different types of errors. These include averaging, multi-step methods, multipoint methods, closed-loop methods and calibration.

The importance of calibration to the accuracy of a measuring instrument cannot be overemphasized. The International Vocabulary of Metrology (VIM) [100] defines calibration in two (2) steps. Firstly, as a procedure which under stated conditions, establishes a link between the quantity values with measurement uncertainties provided by measurement standards and corresponding indications with associated measurement uncertainties. In the second step, the information obtained from the first step is used to establish a relation for obtaining a measurement result from an indication.

From the definition, without calibration the accuracy of a measurement cannot be guaranteed as it will be impossible to relate the traceability of measurements to reference standards. Calibration process does not only establish a relation between a measurement result and the measurement standard, but also identifies and allows for correction of systematic errors [101].

Manufacturers mostly provide some generic calibration values in the datasheets of the sensors that they sell. In most instances, the calibration of these devices is usually performed under favourable conditions. However, when these sensors are deployed in real life applications, some researchers have expressed significant differences from the reported calibration values. For example, in [102] the values of light sensors deployed in an application were calibrated based on manufacturer specifications. The calibration values were compared with the value obtained from a sensor calibrated in an environmentally controlled compartment. The authors expressed disappointments at the significant differences in the values obtained.

The calibration process is traditionally performed under controlled conditions. When such conditions are not available, or when sensors are in operation, the parameters of the sensors can be adjusted with reference to another sensor of the network that has been calibrated with a reference standard [103, 104], or with respect to an already calibrated sensor not on the network [105].

Single-sensor calibration often depends on the provision of a specific inducement with a known result, thus directly mapping sensor outputs and expected values. Accordingly, such calibration for a sensor is often restricted to operating conditions and particular ranges, and can be executed in the factory, at the manufacturing stage, manually in the field, or both.

Additionally, it is important to recalibrate sensors in order to ensure their proper operation as factors such as aging affect sensors and other measurement hardware over time. When a sensor is calibrated in the field, and with the lack of controlled environment, it is termed self-calibration in an uncontrolled environment [106].

When the response of a sensor cannot be measured in a monitored environment and the parameters of the sensor must be adjusted in relation to other sensor nodes in the network, significant errors in the sensor measurements can result from poor or incomplete calibration. Furthermore, even if the sensors are calibrated before they are deployed or embedded in an application, sensor drift may be unavoidable

after deployment, particularly when the lifespan of sensor systems can be as long as decades. In some cases, incorrect data can be produced by even high-accuracy and expensive sensors when aging. For that reason, it is essential to detect drifts, damage and miscalibration automatically in order to correct measurement from sensor after deployment so that the long-term trustworthiness of sensor systems can be ensured.

Although important, several challenges arise from the task of ensuring the quality of data in embedded systems [107]. In an embedded application, Boundanna et al observed in [102] that inaccurate data that lead to failures can occur in unexpected ways. Faulty data is described as data reported by a sensor that is not consistent with the phenomenon being investigated [108, 109]. Systematic and random errors, (inherent in every measurement due to environmental noise, the accuracy of the equipment, or defects in sensor manufacturing) can result in significant faults in measurement.

The error of a sensor can be defined as an unpredicted value from the sensor device after it has been deployed. This error could be due to degradation in accuracy, drift, reading bias, or sensor failure. Consequently, the measurement error can be defined as the difference between the values measured by a sensor and the true values provided by a reference model. These errors are usually referred to as gain, drift, bias and offset and have been described in [108] as the dominant forms of sensor calibration errors that occur in uncontrolled environments.

Several methods of calibrating a sensor have been discussed by researchers. Some of these involve calibrating a sensor in relation to sensors that have already been calibrated (e.g. distributed calibration)[105], or with respect to sensor nodes that are not calibrated (as in blind calibration) [110]. Reversal measurements as a method of self-calibration have been investigated by researchers. A survey of several reversal techniques for dimensional metrology is presented in [111]. Most of the methods presented involve physically manipulating some component, or components, of the measurement system. However, altering the contact conditions may introduce a change in the property being measured which can present uncertainties in the measurement result.

5.2. Effect of shutter movement

In [48] the effect of voltage variation on the SPM sensor was investigated. Stable output from the SPM is dependent on the stability of the voltage supply since the intensity of the light emitted by the LED is affected by change in supply voltage. The displacement measured by the SPM head is a function of the strength of an incident light on the receiver. A differential voltage schema was shown to reduce the influence of input voltage of a four-sensor configuration SPM. The differential voltage schema is not achieved mechanically. Rather, it is implemented on a LabVIEW program using equation (1).

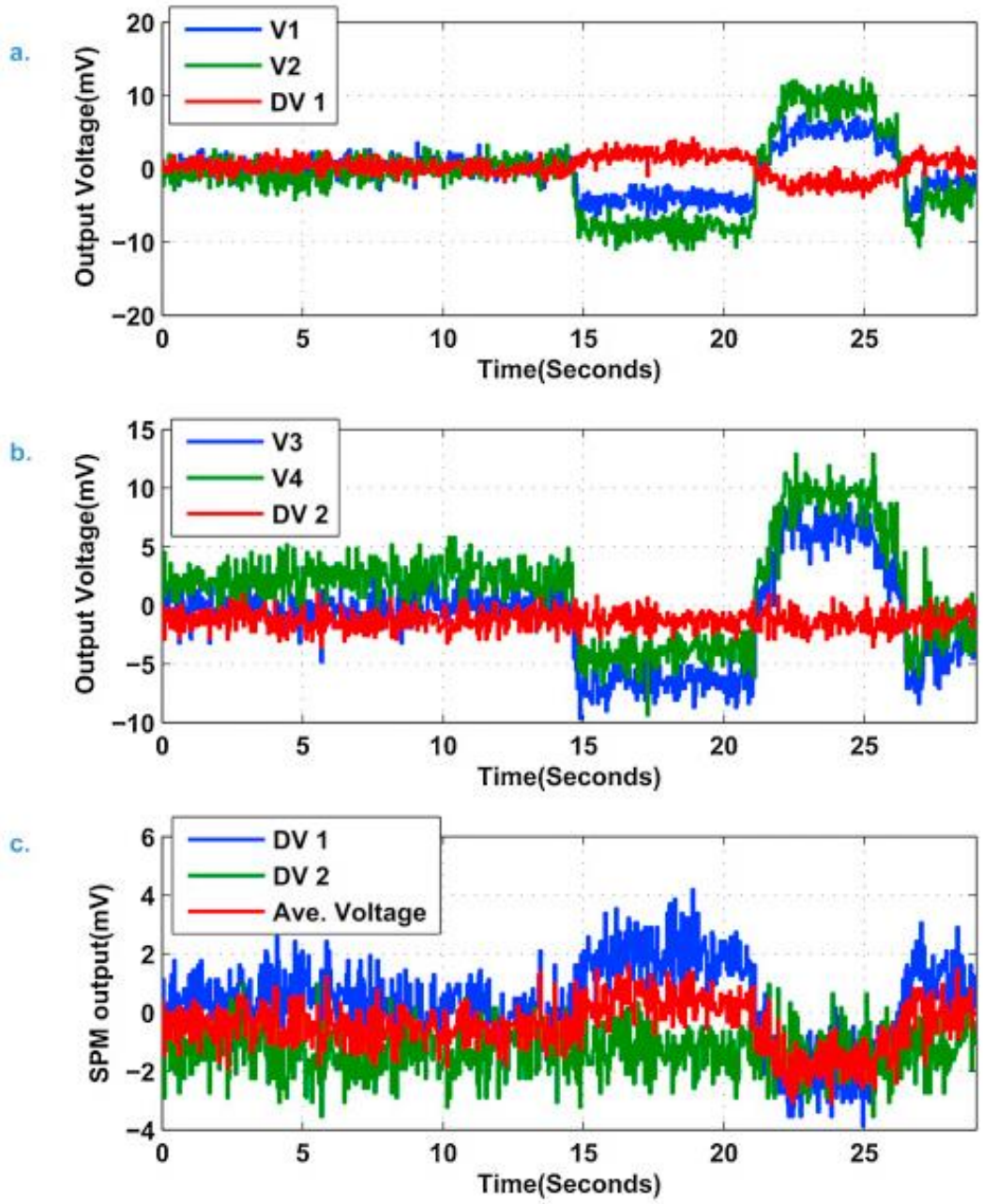

Figure 49: Insensitivity of sensor head to variation in power supply (a) Differential voltage between SPM 1 and SPM 2 (b) Differential voltage between SPM 3 and SPM 4 (c) Average of (a) and (b) [48]

When the sensors were first manufactured, they are calibrated, and the relationship between the four (4) voltages was determined as shown in equation [1]. In an ideal working condition, the voltages should cancel out due to the differential voltage arrangement. Thus, when the intensity of light is increased or reduced by adjusting the SPM input voltage, and if the shutters remained perfectly aligned, and then there should be no change or difference in the result.

However, when installed on a machine, the balance between the voltages can vary due to for example, individual movements or circuitry. Furthermore, due to aging or vibrations during machine operation the calibration can be jettisoned such that the reference will, in certain situations, produce a voltage that is not tolerable by the downstream circuitry. This means that voltage cancellation is not fully achieved, and this causes an error which can result to an increased functional risk to the downstream circuitry. In this instance, the relationship between the voltages is indicative of the error.
The effect of any movement of the shutters due to vibration during operation for example on the SPM sensor output was not investigated in Potdar et al [48]. In a manufacturing environment or when the sensor is embedded in a machine tool, the movement of an individual shutter is likely, so it is essential to investigate its impact on the output of the sensor.

An investigation of the influence of shutter movements on the SPM output is described in the following section. The technique applies input voltage calibration to detect the SPM shutter misalignment. The theory is to measure an uncalibrated sensor by varying the supply voltage at several positions within the working envelope of the measuring system. These are then compared with the results from a calibrated sensor, and from the repeated measurements deductions about the geometric imperfections of the measuring system can be made.
The proposed technique has the advantage that it can be tested continuously at any time throughout its life. A second advantage is that continuous testing can be complemented by repeated self-calibration.

5.3. Experiment Setup and System Description

The equipment and setup described in section 4.2 and shown in Figure 33 and Figure 35 was used to perform tests to test the proposed technique. The test equipment was placed on the granite bed of a Coordinate Measuring Machine (CMM) (Eley Toccata) to provide a reference that is both mechanically and thermally stable. SPM sensing head was mounted on the granite bed and a piezo-transducer PAZ015 was attached to one end of the SPM. The piezo was used as a driving mechanism to move the SPM module over its calibration range. The PAZ015 has a feed-back control loop which provided good control for small displacements. The entire setup was located in a temperature regulated room which was measured to be 21 ± 1 °C, for the total period of the tests.
A Renishaw ML10 laser interferometer system was used as the independent reference displacement measurement. The laser reflector optics was mounted on the SPM sensor to ensure that both the sensor and laser optics experience the same displacement from the piezo actuator. A Farnell L30B

stabilised power supply (Mains input: 110 V, 220 V a.c or 240 V a.c, ±10%, 50/60 Hz; Output: 0 – 30 V, 1 A) was used as a DC voltage source to excite the SPM sensor.

The proposed technique and a flowchart to represent the procedure are described in Figure 50.

In this thesis chapter, a ‘good’ or ‘perfect’ setup describes a setup where all four SPM shutters are properly aligned such that they all measure equal voltages. Although this is impractical to achieve, the variation in the voltage measured by the individual shutters is assumed negligible.

A ‘bad’ or ‘adjusted’ setup is a setup where at least one of the shutters is misaligned. This results to an imbalance in the sensor output.

The test procedure is as follows.

i. At a constant position of piezo actuator, vary the supply voltage within the voltage range.
ii. Record the results from the SPM sensor for each voltage variation.
iii. Change the actuator position under the same setup and repeat steps (i) and (ii).

A least squares fit for the sensor is performed using the measured data. The voltage is excited to investigate the pattern of the sensor response for each setup (i.e., good or bad setup) to provide a better informed decision-making process.

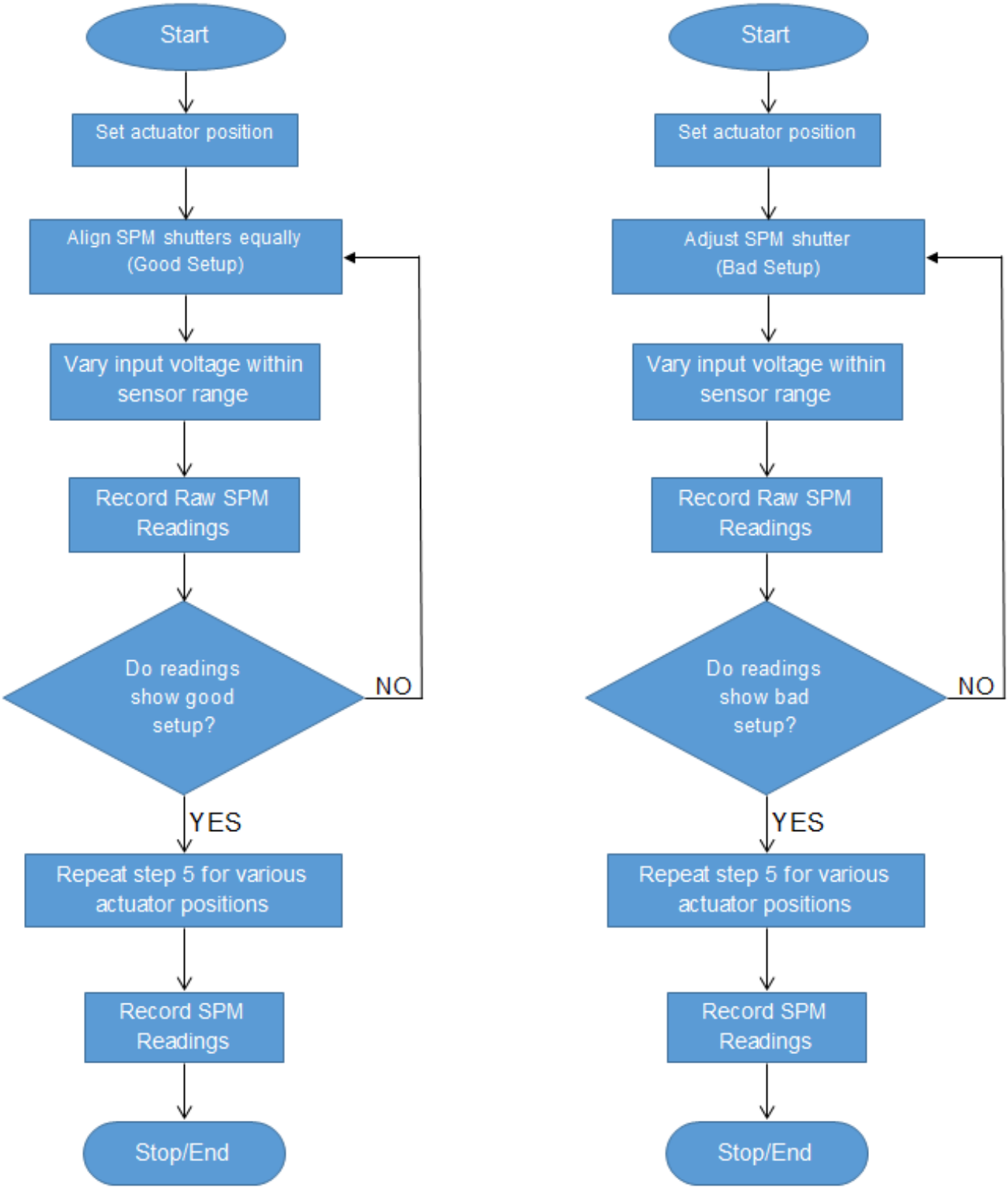

Figure 50: Flowchart for voltage calibration technique

5.4. Voltage Self-Calibration Method

When the sensor module is calibrated (i.e. the shutters are aligned perfectly), it is expected that the four sensors measure equal voltages (V1 – V4). The shutters are aligned by manual adjustment until all SPM sensors measure equal voltages. Assuming that one shutter is shifted during operation due to vibration for example, an error is observed in the result of the sensor. It is vital to estimate the amount by which the shutter has moved especially as the movement of one shutter could result in the movement of another shutter, or affect the overall performance of the sensor module.
To estimate this error, we recall that the sensor module is designed to operate in its linear range. In this region, the gradients should remain constant with changing input voltage. Tests were performed by varying the input voltage to the sensor module for a 'good' alignment of the shutters. One shutter is then mechanically moved to simulate a 'bad' setup, and the process is repeated for the 'bad' setup. The results for the good setup and bad setup are compared to estimate the effect of shutter adjustment on the sensor output.

Initially, at a voltage (9.5 V for example) and for a good setup, the sensor is calibrated against the laser by using the piezo to move the shutters. This results to a nominal relationship between the light current and physical movement of the shutters and this is compared against the laser. The excitation voltage to the sensor is then reduced (to 5.5 V for example), and the process is repeated. Measurements are taken over the sensor measuring range.

This results in two calibration curves, one for 5.5 V excitation voltage of the sensor, and for 9.5 V excitation of the sensor as shown in Figure 51. This provides an insight to the sensor behaviour over its measuring range.
At 5.5 V excitation voltage, a slight variation was observed at the lower range of the calibration curve. A similar trend was also observed in the piezo calibration curve shown in Figure 37 suggesting a slow response of the SPM to displacements at the lower range of the piezo controller used in this research. However, this was not further investigated.

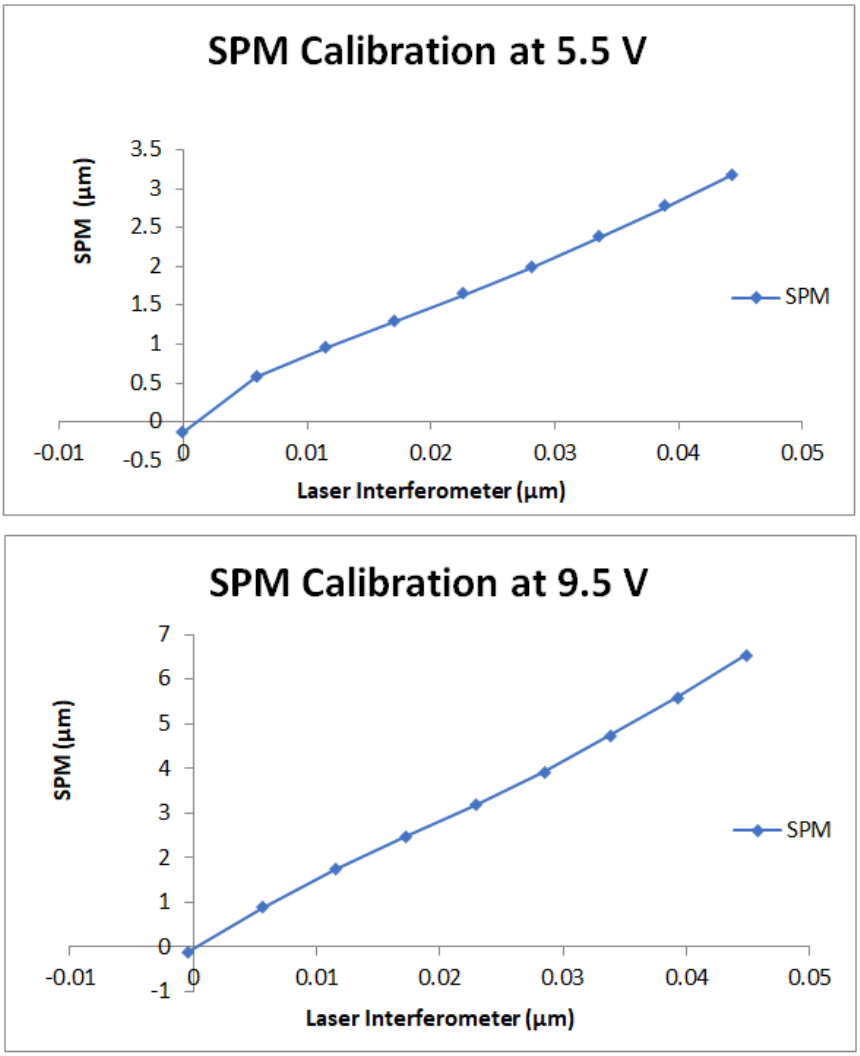

Figure 51: Relationship between light variation and shutter movement

When the sensor is installed, and the excitation voltage is varied, the output of the individual sensor can be compared to ascertain their behaviour in relation to the calibration curve. If the behaviour of the sensors is similar or consistent, it indicates that the shutters are in the same position as shown in Figure 52.

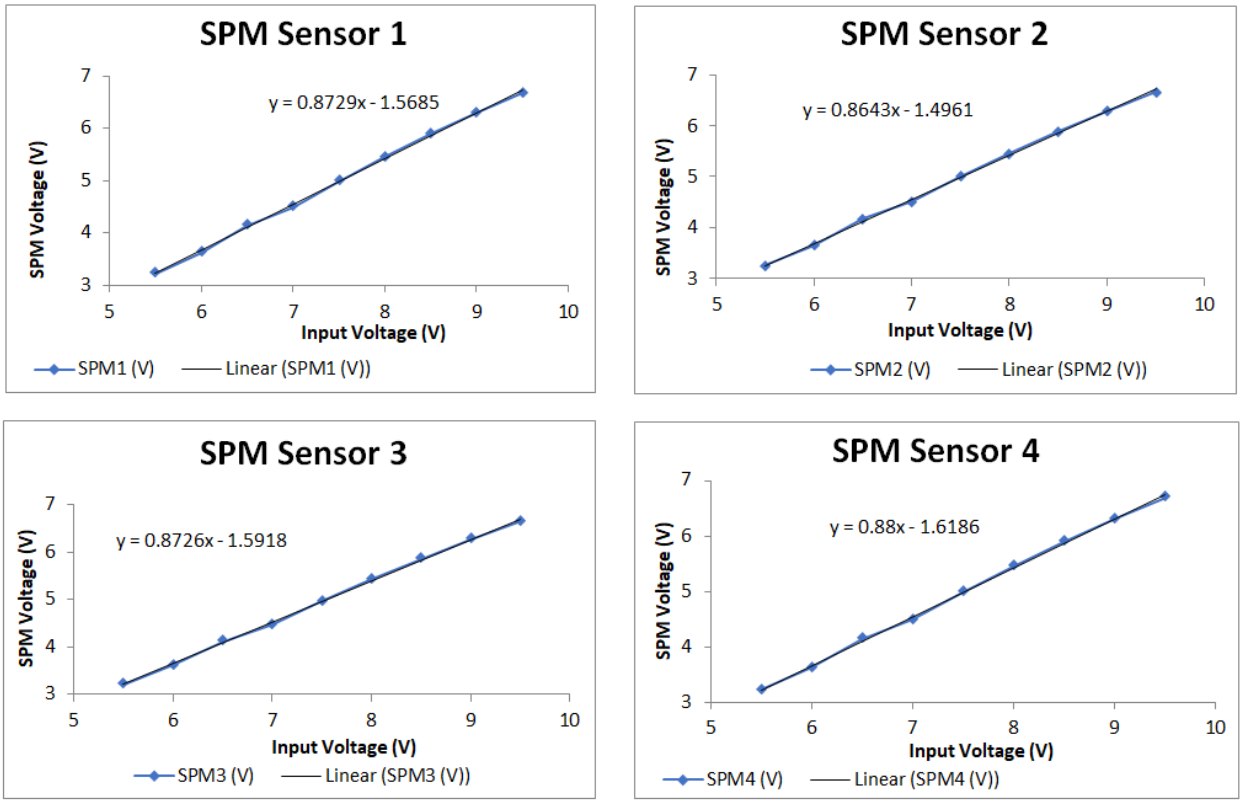

Figure 52: Comparison of sensors for a Good Setup

In Figure 52, it can be observed that the sensitivity of the graphs for the four (4) sensors is consistent. This indicates that the shutters are at the same position for all four sensors.

At some point, there is an unknown mechanical shift in one of the sensors (bad setup). The input voltage is again excited through the voltage range. The shifted sensor is expected to have a different output (slope) to the other sensors. This is shown in Figure 53.

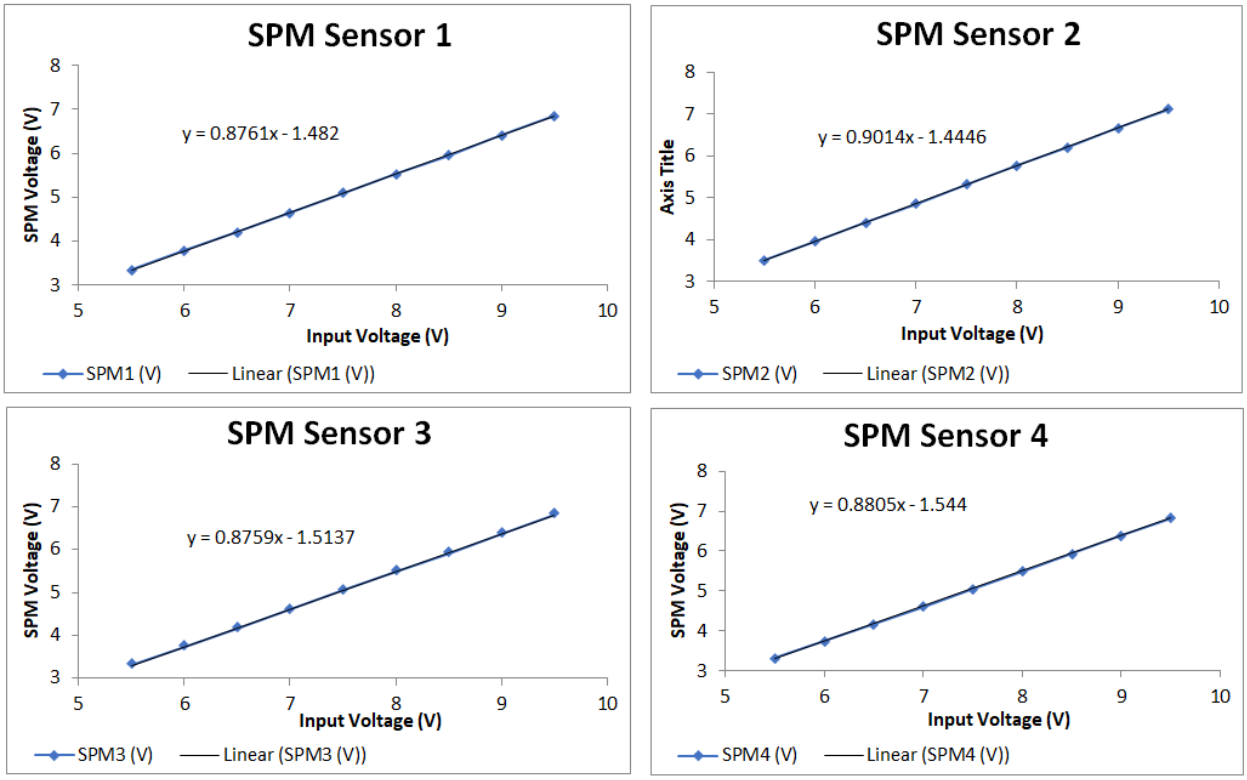

Figure 53: Comparison of sensors for a Bad Setup

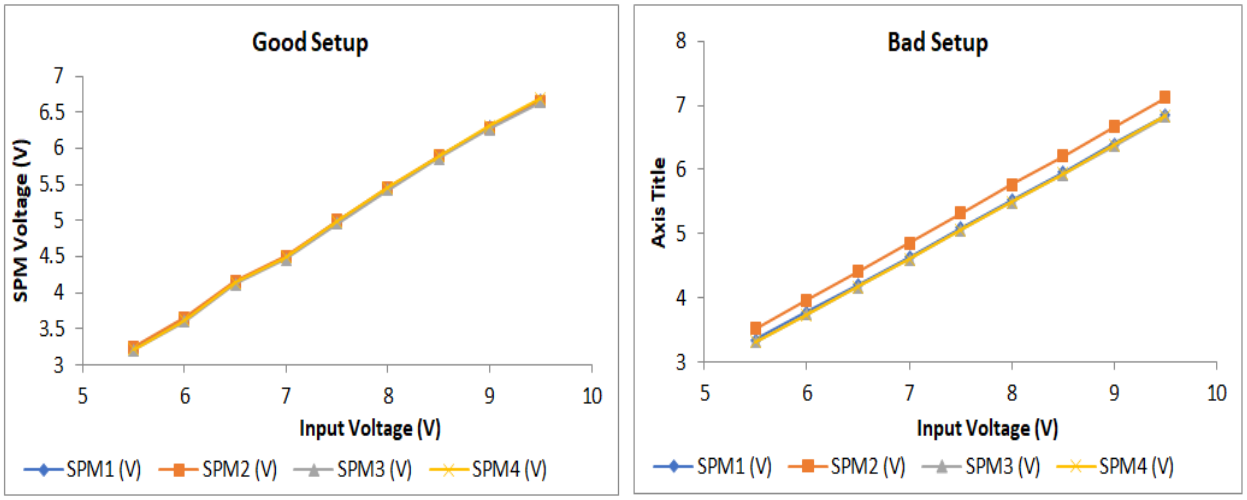

Figure 54: Graph for Good Setup and Bad Setup

In Figure 53, it can be observed that the sensitivity of the graph of sensor 2 is different from the sensitivity of the other three sensors. This indicates that the shutter in sensor 2 is at a different position from the three other sensors.

Figure 54 shows a plot of all four sensors for a good setup and bad setup. The variability in output can be observed between the good and bad setup, repeatable to within 6 mV.

This results in two possible outcomes.

In the first case, we can assume that only one sensor is bad, hence the other three (3) sensors can be used as a reference. This is observed when the voltage is varied, and it is observed that a sensor gives a different output to the three other sensors. This variation indicates an error as observed in Figure 54.

In the second instance, it is possible that more than one or all sensors have been displaced, and when the input voltage is changed, it becomes difficult to ascertain which sensors give the correct or wrong results. The voltage calibration procedure is applied in this scenario to detect and ascertain which sensors have been displaced, and to correct for the detected errors.

Over the measuring range of the sensor, measurements are performed at five points along the sensor measuring range. At the beginning when calibrating the sensor, we move the shutters using the piezo to these five (5) different positions. At each position, the excitation voltage is changed through its voltage range.

If an unknown movement of the sensor is observed at some point due to vibration or mechanical shift for example, the behaviour at that position can be examined by exciting the voltage through the measuring range and comparing with the result for a calibrated setup to correct for the observed error. Thus the sensor output at that position can be brought back to its nominal position.

The voltage calibration technique can be applied for the cases where one, two or all four shutters have been shifted. The results are presented in Figure 55.

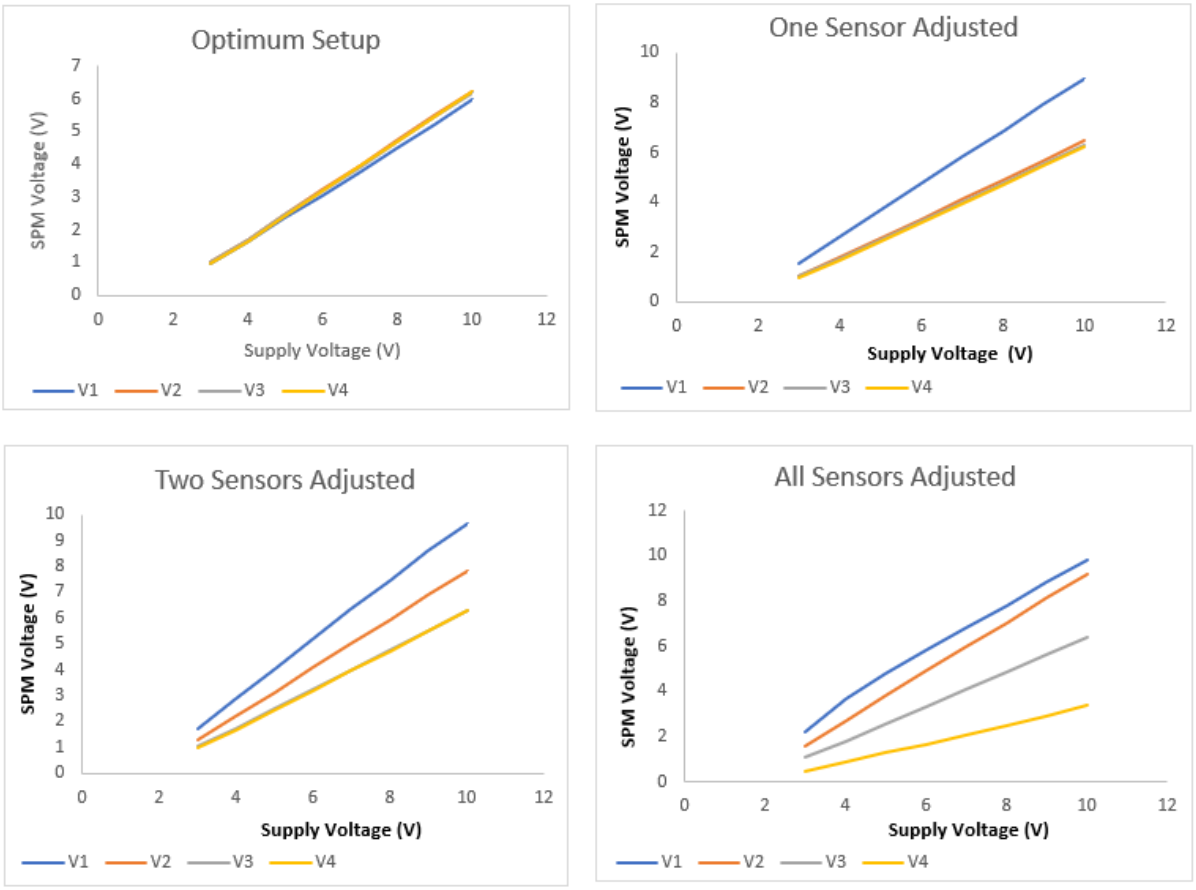

Figure 55: Shutter Misalignment

The Figure 55 shows the results for the various scenarios of shutter misalignment and it can be observed that the proposed technique can identify the sensor that is misaligned. This shows applicability of the proposed technique for detecting a misaligned sensor(s).

The SPM sensor was reported to operate on a differential voltage principle [48] in which the differential output of opposing shutters (one closing while one opens) reduces or cancels the effect of drift of the input voltage. However, it is possible that the misalignment of one or more shutters could create an imbalance which could annul the differential voltage principle. It is important to investigate that the sensor principle can be implemented on the proposed voltage self-calibration method. This was investigated by applying equation [1] to the test result presented in Figure 53.

The result of this implementation is shown in Figure 55.

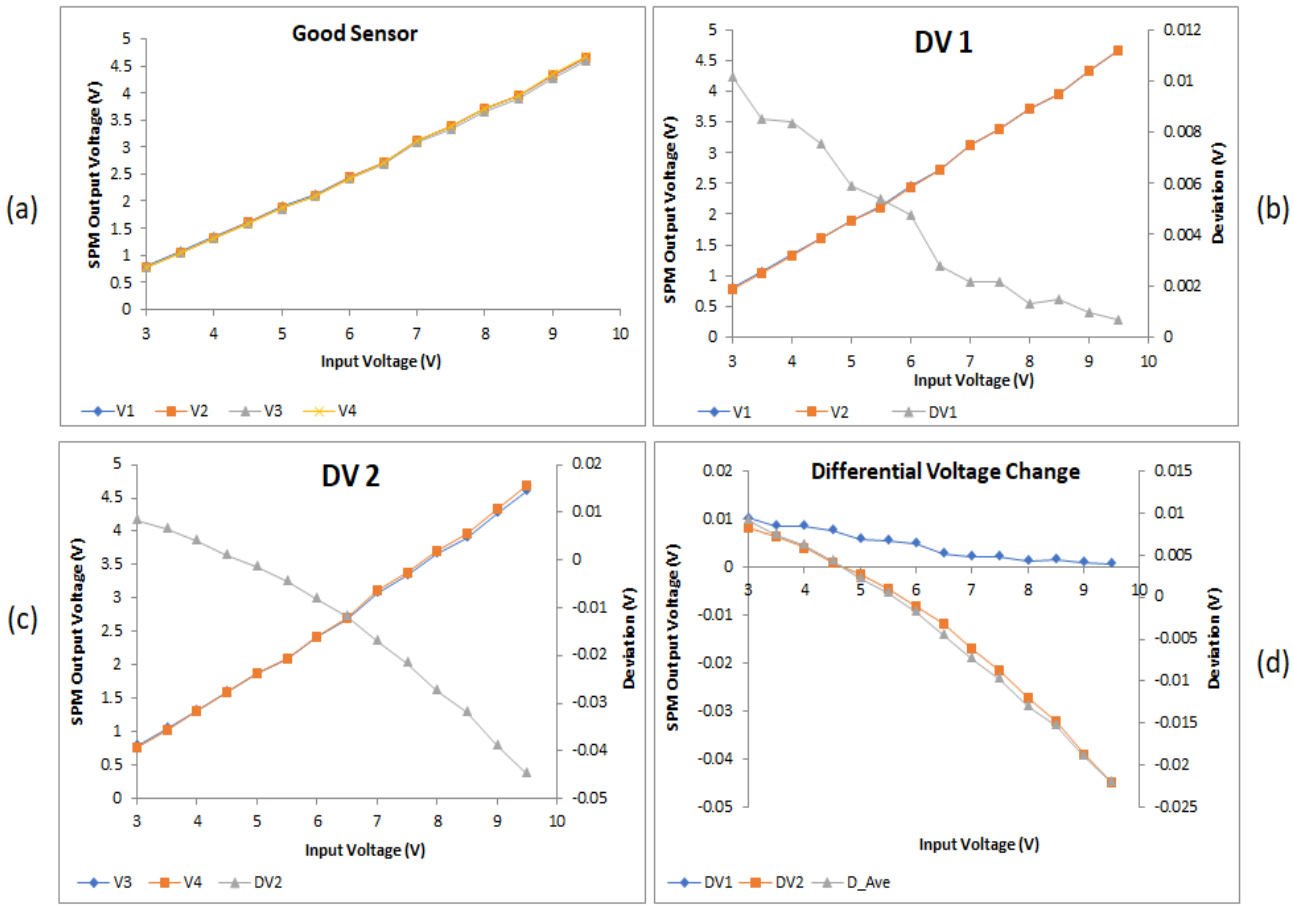

Figure 56: Differential voltage principle implementation on self-calibration technique for good setup (a) Good setup (b) Difference in voltage (DV1) between sensor S1 and S2, (c) Difference in voltage (DV2) between sensor S3 and S4, (d) Average of DV1 and DV2

Figure 56 shows the implementation of the differential voltage principle of the sensor on the self-calibration technique for a good setup. The differential voltage (DV1) between S1 and S2 is a maximum of 0.01 V, and 0.055 V between S3 and S4. It can be seen from Figure 56 that the differential voltage principle reduces the difference in the sensor voltages, and the final average SPM output voltage is 0.03 V which equates to 0.004 µm. For a bad setup, the final average SPM output voltage is 0.124 µm.

Thus, it can be seen that the self-calibration technique does not alter the four sensor configuration of the SPM sensor.

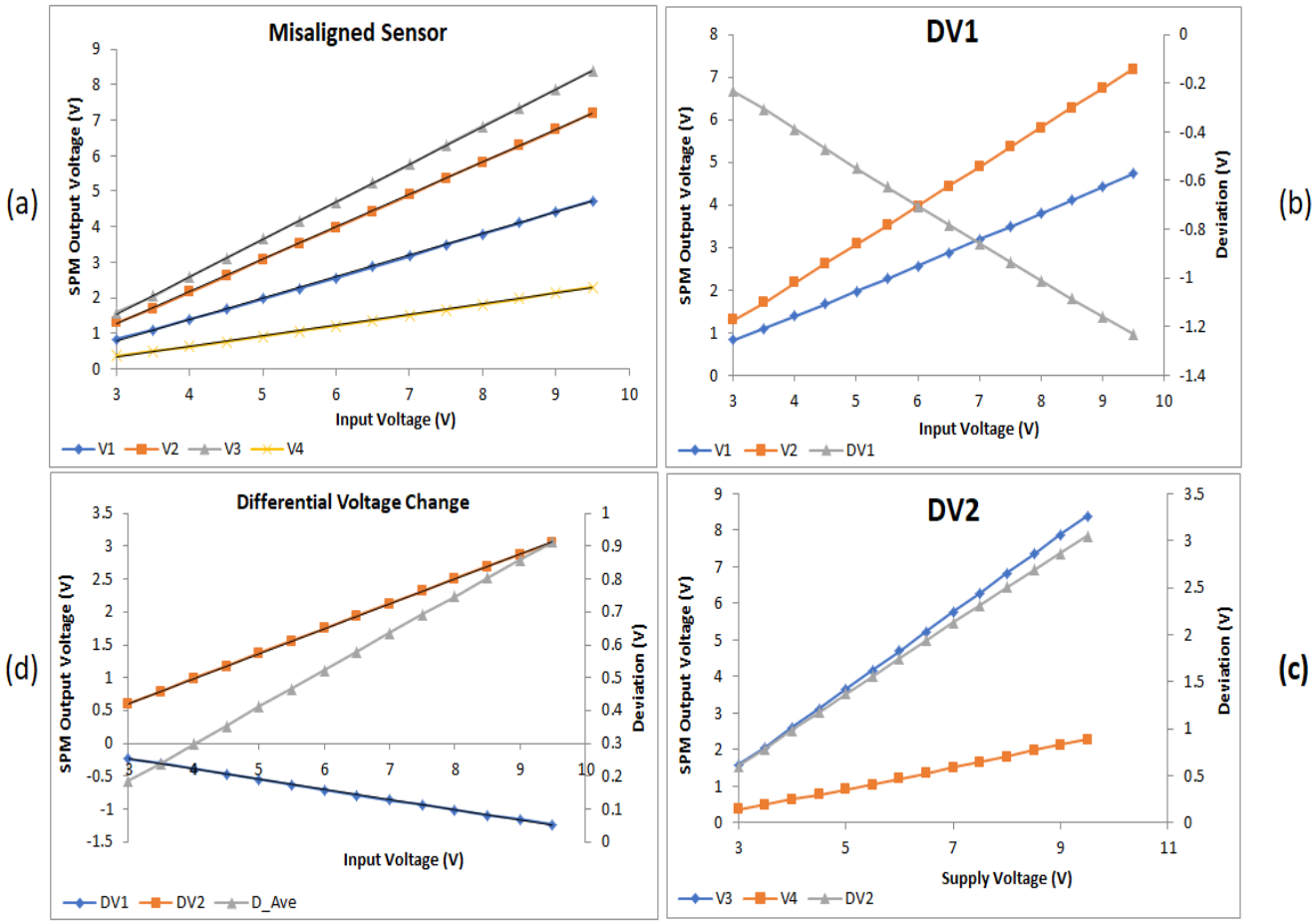

Figure 57: Differential voltage schema implementation on voltage self-calibration for bad setup (a) Bad setup (b) Difference in voltage (DV1) between sensor S1 and S2, (c) Difference in voltage (DV2) between sensor S3 and S4, (d) Average of DV1 and DV2

Figure 57 shows the implementation of the differential voltage principle of the sensor on the self-calibration technique for a bad setup. The differential voltage (DV1) between S1 and S2 is a maximum of 1.2 V, and 3.0 V between S3 and S4. It can be seen from Figure 57 that the differential voltage principle reduces the difference in the sensor voltages, and the final average SPM output voltage is 0.9 V which equates to 0.148 µm.

Again, the self-calibration technique does not alter the four-sensor configuration of the SPM sensor.

5.5 Alternative Voltage Self-calibration Method

A second method of the voltage calibration technique for detection of false sensor readings was investigated. This method uses a slightly different calibration procedure. The procedure is described as follows.

For an optimum alignment of the shutters, an input voltage of 4 V is selected. The piezo transducer is cycled a total of 20 µm in steps of 4 µm. The sensor readings are recorded at each displacement position. The input voltage is increased to 4.5 V and the piezo transducer is again cycled a total of 20 µm in steps of 4 µm. This is repeated for the entire input voltage range of the sensor.

One shutter is adjusted to simulate an error and the test procedure is repeated for this adjusted setup. The results are plotted and the sensitivities of the graphs for the different positions are compared. The data obtained is presented in Table 10 and Figure 58.

Table 10: Data obtained for second voltage calibration method

Sensitivity for Different Setups			
Positions	Nominal	0.9 µm Error	1.8 µm Error
0	0.0051	-0.0166	-0.0422
1	-0.0581	-0.0792	-0.1006
2	-0.096	-0.116	-0.1359
3	-0.1336	-0.1526	-0.1709
4	-0.171	-0.1889	-0.2059
5	-0.2081	-0.2249	-0.2404
6	-0.2445	-0.2604	-0.2749
5	-0.2104	-0.2274	-0.2429
4	-0.1737	-0.1918	-0.2087
3	-0.1364	-0.1554	-0.1739
2	-0.0987	-0.1186	-0.1388
1	-0.0606	-0.0818	-0.1036
0	0.0014	-0.0206	-0.0492

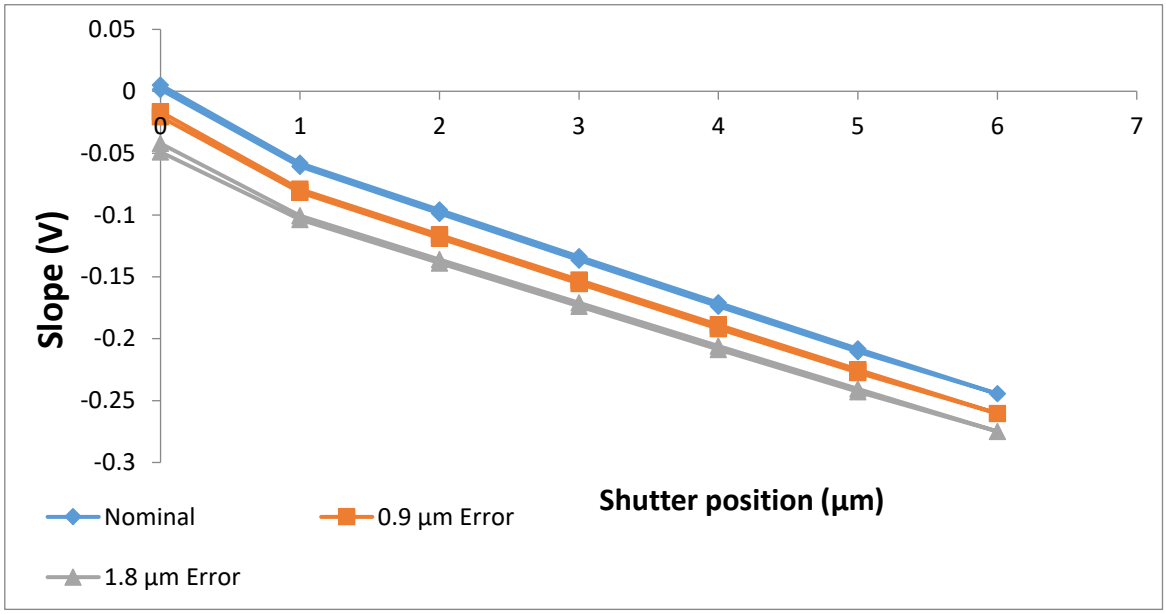

Figure 58: Plot showing the sensitivities for a misaligned sensor with shutter at nominal position, then displaced by 0.9 µm and 1.8 µm.

In Table 10 and Figure 58, '0.9 µm error' and '1.8 µm error' represent the sensitivities of the sensor when the shutter position has moved by 0.9 µm and 1.8 µm respectively.

The procedure was investigated for the case where only one sensor is adjusted. From Figure 58, a deviation from the nominal sensor position is observed. Thus, in an embedded application, an error due to the false readings from one sensor can be detected. The results show the applicability of the method for error detection.

5.6. Shutter Movement Error Correction

The variation in the final output voltage for both good and bad setups is the error introduced by the misalignment of one or more sensors. The voltage calibration technique can correct for the change in output of a sensor.

When the differential voltage output (DV1 & DV2) obtained for each pair of a good sensor setup and a bad sensor setup are compared, an error will be observed. This error value is then added to the measured value of the bad sensor to correct for the misalignment.

An example is illustrated using a measurement data to summarise the procedure.

Perfect Setup (V)						
V1	V2	V3	V4	D_Ave	DV1	DV2
3.24	3.25	3.21	3.23	-0.007	-0.005	-0.01

Adjusted Setup (V)						
V1	V2	V3	V4	D_Ave	DV1	DV2
3.35	3.52	3.32	3.31	-0.04	-0.085	0.005

CORRECTED (V)						
(DV1_Adjusted) - (DV1_Perfect)	V2_Corrected	V1	V2	V3	V4	D_Ave
0.012	3.33	3.35	3.44	3.32	3.31	-0.023

Figure 59: Correction procedure for an adjusted sensor

The mathematical representation of the procedure is given as.

$$V_{corrected} = (DV1_{Adjusted} - DV1_{Perfect}) + V2_{Adjusted}$$

Where $DV1_{Adjusted}$ = differential voltage (V1 – V2)*0.5 of sensor 1 and sensor 2

$DV_{Perfect}$ = differential voltage (V1 – V2)*0.5 of sensor 1 and sensor 2

shows the final output from the SPM sensor compared to a laser with and without compensation. For the linear displacement calibration, there are five measurement points in the range of 20 µm and the voltage calibration procedure is performed at each point. The procedure is performed for a good and bad setup (where one sensor is misaligned). For this experiment, sensor S2 was misaligned.

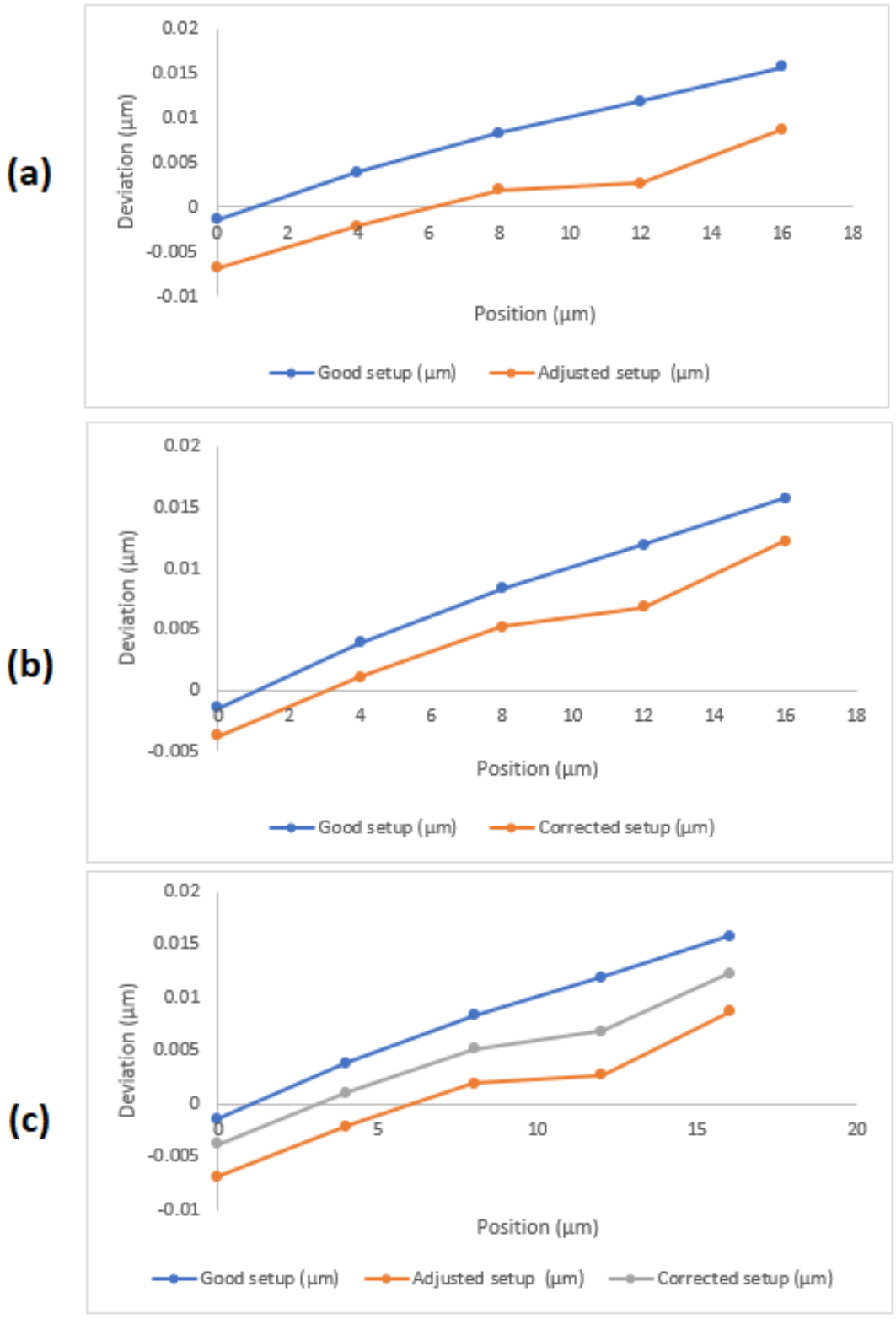

Figure 60: SPM final output (a) without compensation, (b) and (c) with compensation

The systematic positioning deviation was determined in accordance with ISO230-2. Without compensation, it is observed that the systematic positional deviation is 0.007 µm. With the compensation procedure, it is reduced to 0.0035 µm.
Minimal deviation was observed in the output of the three other sensors (S1, S3, and S4) due to instability during the physical shutter adjustment. This was not considered in the compensation procedure. Better compensation would be achieved if the shutters remain stable during the adjustment.

The voltage calibration technique is dependent on the following assumptions.

- The measurement system must be stable through the physical adjustment.
- The shutter remains stable for any given position. (I.e. the sensitivity and y-intercepts for both the good setup and bad setup remain constant).
- The shutter remains constant through the cycle of voltage excitation.

The voltage technique discussed here can be invoked in applications where high accuracy is required; thus the materials selected are unlikely to have dimensional instabilities that are measurable over the duration of the procedure used.
The main source of uncertainty arises from environmental effects. This was minimized by performing the tests in a temperature-controlled environment. In a controlled environment, the other sources of uncertainty arise from changes in the system due to the physical manipulations; and the uncertainties intrinsic in the procedure itself.

5.7. Summary

Two techniques have been presented to correct for sensor misalignment especially in embedded applications where it is impractical to physically adjust the shutters. Precise measurements of displacements for varying DC voltages were made using a 'optimum' configuration of the novel SPM sensor, and the results were analysed. These were then compared with the results for an 'adjusted' configuration of the SPM sensor.

The first technique involves changing the input voltage at constant shutter positions, while the second technique involves changing the shutter positions at constant input voltage. Both techniques use similar setup and are easy to implement. However, the first technique is more suitable when there is a stable voltage source. When a source of displacement such as a piezo controller is not available, then the second technique will be better suited for such an application. Furthermore, both techniques can be performed by manual or electronic adjustment of the voltage source and the displacement instrument. The necessary corrections can be done on a PC using a correction software. Thus in an embedded application both techniques will be realised without the need to remove the sensor.

A procedure was described to correct for the observed errors due to false sensor readings. The result of the analysis shows the capability of the technique to give a mathematically exact solution for the deviation of a sensor and correct for the observed deviation. Although the method introduced here can correct for a misaligned sensor, the contribution of ambient light cannot be totally eliminated. However, this contribution can be further reduced by using a lid.

Chapter 6 - Improved sensor module design

Some sections of this chapter have been published in [112].

6.1. Introduction

The original design confirms the basic functionality, repeatability, resolution and accuracy but the manufacture challenges add cost that is significant compared to the material costs of the components, particularly the SPMs. In addition, the stiffness of the flexure system was high which decreases the sensitivity due to losses in the connecting rods. Finally, there were two flaws in the design that revealed themselves when installing and using the sensor and relate to each other. When adjusting the individual shutters, a roll motion was permitted because only 5-DoF were controlled which affected the other sensors during installation.

In this chapter, an improved design of the sensor is described. Design modifications were implemented to reduce the errors due to the positioning and movement of the shutter, as well as the flexure system, thus improving the overall performance of the sensor for strain sensing applications. The need for fine structures in the shutters, flexures and some form of adjustment led to the idea of a 3D printable design which can provide high complexity and intricacy at a reduced manufacturing cost. A prototype has been designed and built using standard PLA material (used on the standard FDM printers available to the research) and preliminary functional tests completed. The simplicity and cost of the improved design are well-suited with embedding into machinery for long term structural monitoring.

6.2 Justification for the improved design

Design Limitations: The tight tolerance of the original design presented significant difficulty and time-constraints in accurately positioning the shutters for pairwise clustering which is an important part of the sensor working principle, and allows only a single degree of freedom.

Cost: Although the sensor design uses very low-cost slotted photomicrosensors, the machining of the sensor housing and components extends using traditional methods significantly extends its cost. An analysis of the cost of manufacturing including the programming cost obtained from a technician at the Center for Precision Technologies, University of Huddersfield is presented below.

The time for manufacturing the individual part on the CNC machine is detailed as follows.

Base - 40 minutes

Flexure - 25 minutes
Shutter arms - 30 minutes for all 4
Shutter holder – 35 minutes
Adjustment clamp – 20 minutes

This time is independent of the number of sensors that are being manufactured. This equates to 150 minutes for one sensor at a cost of £50/hr.

For a one-off, the programming and prove out costs probably of about 8 hrs @50/hr.
Other costs include tooling and material costs, and manual handling. The tooling cost that would cover everything from one to 100 parts was estimated at about £200.

Some of this could be reduced by using automation, but they are complex components.

The cost analysis is summarised in the Table 11.

Table 11: Cost analysis of SPM sensor housing

Item	Time (hours)	Cost (£)
Manufacture of parts (@ £50/hr)	2.5	125
Programming (@ £50/hr)	8	400
Tooling	-	200
Material & manual handling	-	70
Total		**795**

From the above, the cost of manufacturing a batch of 10 sensors outweighs the advantage of the sensor which is for a low-cost solution.

Performance: The geometry and material of the flexure system in the original design impacted its mechanical stiffness which increased the forces in the joining mechanisms, thus reducing the sensitivity. The improved design reduces the rigidity of the flexure thus minimizing the joining forces and allowing larger deflection of the flexure while maintaining control of the shutter movement.

6.3. The Physical Principle of the Improved 3D Printed Sensor

A 3D model was established using SolidWorks and the SPM displacement sensor is printed by the fused deposition modeling (FDM) method. FDM method was used because it is simple to use, budget-friendly, and allows a variety of material choice for use in printing. Also, an FDM printer was the available printer at the time of this research,

Several materials are available for 3D printing but Polylactic acid (PLA) was selected for this application because it has higher stiffness and strength than nylon and ABS for example. It is affordable, and can be easily printed on most available 3D printers without the need for a heated bed.

Three-dimensional (or 3D) printing is an additive manufacturing (AM) technique that makes it possible to manufacture a range of items by the addition of materials layer-by-layer based on a computer-aided design in a fast and cost-effective approach [113]. It is different from conventional manufacturing techniques that involve the removal of parts from a larger piece of material [5]. Several technologies are available for 3D printing, among which is fused deposition modelling (FDM). FDM is the most common method of 3D printing due to its low cost, extensive range of material choice and simplicity of use [114]. Owing to its advantages and adaptability, many researchers have used 3D printing to design and develop new prototypes, for example the manufacture of several medical devices [3, 6], components housing [7].

Figure 61: Fused deposition modelling 3DP process of a face shield. 3DP, three-dimensional printing

Although not a new technology, 3D printing has seen tremendous applications in the decade as a result of the 'democratization' of the technology [115]. Thus, 3D printing technologies have been used in the manufacture of various materials including metal, polymer, concrete, ceramics, and even biological tissues. Two of the most common materials for 3D printing are thermoplastics and photopolymers [116]. Thermoplastic 3D printers operate by heating thermoplastic-like acrylonitrile butadiene styrene (ABS) until it can be extruded from the printing nozzle while the photopolymer 3D printers extrude a

liquid photopolymer which is then cured by a light source during the printing process. The part is positioned with reference to the printing nozzle by a three-axes positioning system while the material is extruded in layers onto the printing surface.

3D printing offers several advantages over traditional manufacturing techniques. For example, it has excellent flexibility, which makes it suitable for production tasks to any degree. It can also be used in the production of molds for manufacturing. 3D printing also has the advantages of manufacturing complex objects and diversification of products at a low cost and short fabrication cycle time. Furthermore, it provides designers with limitless design space, thus overcoming the limitations of traditional manufacturing [117].

In recent years, 3D printing sensors technology has made remarkable development. For example, [116] used 3D to develop a catheter tip force sensor. 3D printed sensors offer several benefits over discrete general-purpose sensors. Firstly, 3D printed sensors can be tailor-made to the configuration of the overall system, which reduces or eliminates the need for a rigid mounting interface with the sensor. Secondly, 3D printing makes it possible and easy for a sensor to be quickly improved through iterative prototyping and redesign in a low-cost manner. This permits for fast transformation of a design from conception to a device that is useful. Thirdly, 3D printing allows for miniaturization which is supported by the ability to print small, lightweight and complicated structures. Finally, 3D printed sensors can easily be modified for dedicated applications, for example, for chemically harsh environment.

Based on findings from previous research on the 3D printing technology and its observed advantages, a novel SPM displacement sensor was fabricated using the 3D printing technology. A description of the design process, including the sensor parameters and structure of the design, the manufacturing and mounting is presented. Finally, the 3D printed sensor is tested, and the results analysed. The experimental setup comprising of the proposed design and Zerodur rods is described for strain monitoring is described. The main novelties of the design are based on its flexure arrangement which constrains the sensor movement and allows only one degree of freedom of movement. The design is intended to reduce variability in the results obtained across the four sensors in a sensor module, achieve lowest stiffness possible to allow maximum deflection while maintaining 3D printable and robust flexures.

Thermal analysis using FEA on SolidWorks was performed to estimate the effect of temperature on the design. The results were compared with results from a similar setup comprising of a sensor fabricated using traditional manufacturing techniques. A potential application of the sensor is machine tool thermal compensation.

6.4. Description of proposed design

An overview of the sensor module is presented in Figure 62. It is very similar to the original design but with a few key changes described in the following sections.

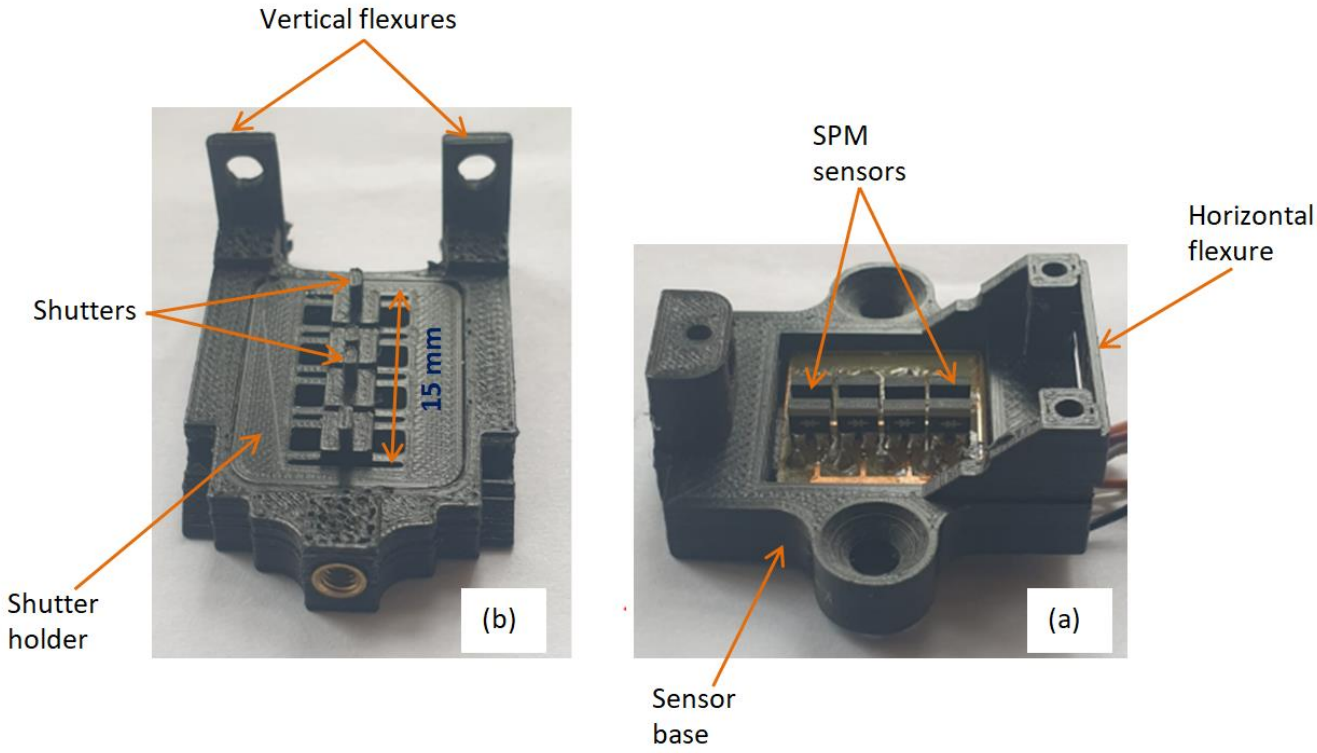

Figure 62: Component of sensor housing (a) Sensor Base (static part) (b) Shutters and shutter holder (movable part)

The Figure 62 shows the two main parts of the sensor frame. The frame is a plastic 3D printed solution adopted to eliminate difficult machining of small features and making assembly easier. Figure 62a shows the base of the sensor which is the stationary part with the circuit board and SPM sensors attached. The moving part of the housing comprises of the shutters and shutter holder. Fabricating the shutters and shutter holder as one part makes for easier assembly. Both components of the housing are joined together by the flexure mechanism to form a complete unit and all parts of the sensor housing are 3D printed without any structures for support.

6.4.1. Flexure System

The flexure system was designed and employed in such a way as to hold both component parts together and allow the movement of the parts relative to each other without friction. The design incorporates two flexures – a horizontal flexure element which constrains roll in the z-direction, and dual vertical elements which allows single degree of freedom (DOF) motion. The function of the flexure is best seen in the FEA result shown in Figure 65. For a flexure system, the relative stiffness of the drive and flexure represents a measure of achievable precision. The rigidity and thickness of the design of the flexure is optimised to obtain the required thickness, hence reducing its mechanical stiffness. The performance of a flexure system is usually a trade-off between its stiffness, deflection, precision, which profoundly affect their overall performance. The characteristics of the improved design were compared with the original design and the results show that the current implementation has a great improvement in precision, and stiffness for similar range of motion.

6.4.2. Sensor adjustment post installation

During assembly, the task of setting all four sensors close to the middle of their range to make the most of the linear part of the output provides a significant challenge. To minimize this challenge, the SPM sensors are bonded onto the circuit board using a fixture to achieve good uniformity. Although this design greatly reduces the assembly time and difficulty in getting the same voltage output at the nominal position, it is not sufficiently accurate when combined with the 3D printed housing. To achieve better accuracy, M2 grub screws, as shown in Figure 63, are used to adjust the shutters with very fine control considering that the sensor has a high sensitivity.

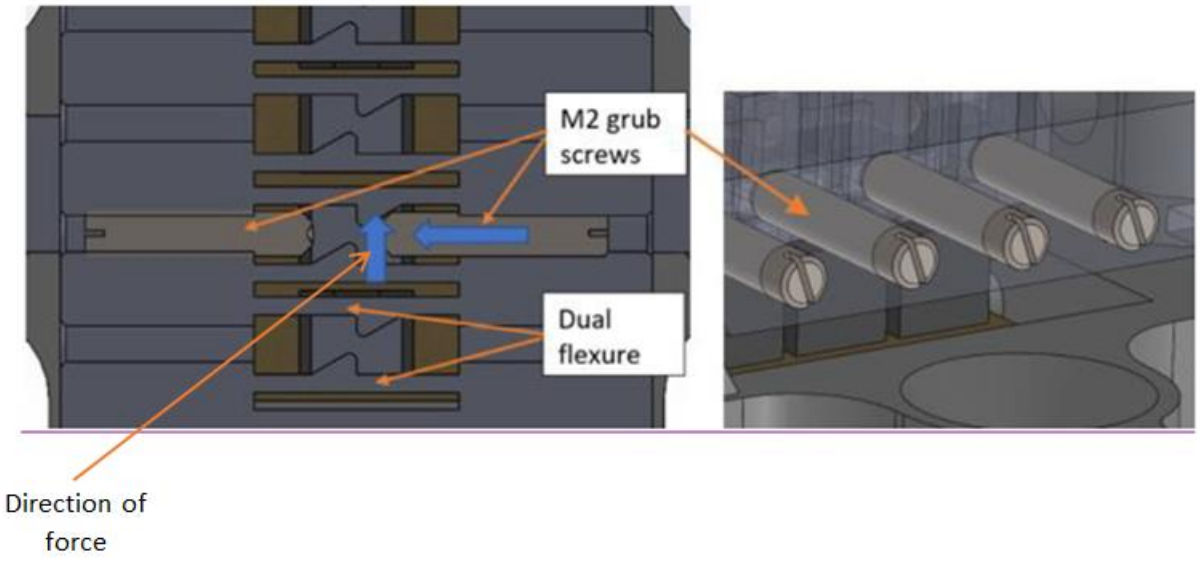

Figure 63: Shutter adjustment mechanism

The shutter is adjusted by moving the right or left screws. When the right screw is inserted, the shutter moves in the direction of the force while it moves in the opposite direction when the left grub screw is moved. Figure *64* shows the resultant movement of the shutter by application of a force through moving the grub screws.

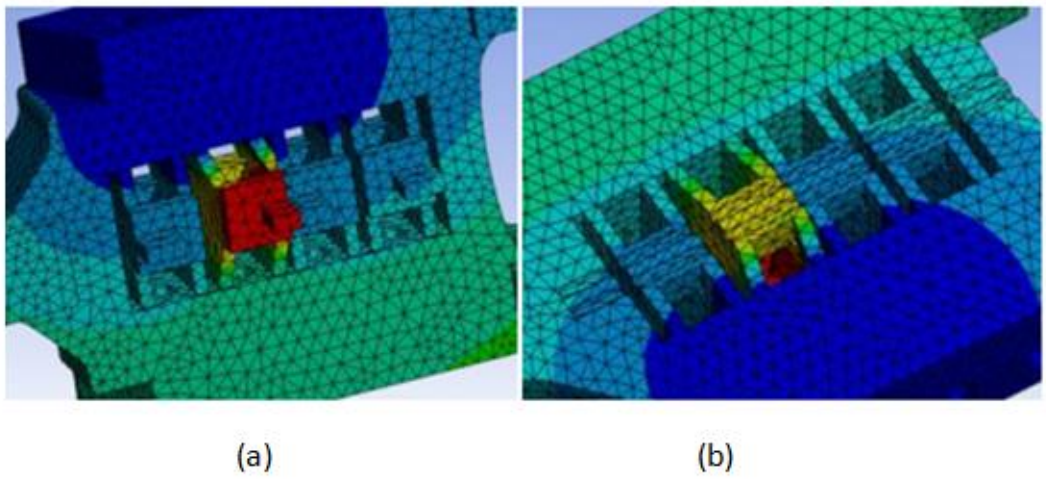

Figure 64: Resultant shutter movement after adjustment (a) Bottom of shutter holder showing the adjusted shutters (b) Top of shutter holder [112]

6.4.3. Model testing and evaluation

Preliminary evaluation of the model is through Finite Element Analysis (FEA). Characteristics such as stiffness, displacement, and contamination from transverse motion were investigated in a static test. The force-displacement relationship was determined applying an axial force of 1N to the moving part of the assembly. Figure 65 shows the amplified effect of the force. The thickness of the flexure is a concession between as small as possible to allow deflection and as large as possible to ensure low uncertainties of measurement or damage during installation. For this design, the front flexure has already been reduced to the minimum thickness possible through design and geometry modification using a typical 3D printer nozzle size of 0.4 mm. A deflection of 5.309 µm results from the 1N force which equates to a stiffness of 0.188 N/µm. The variation in displacement of the face of each shutter was 0.04 µm due to tension/compression in the housing. Although this is small, it is not negligible, but is a constant that can be removed through the calibration.

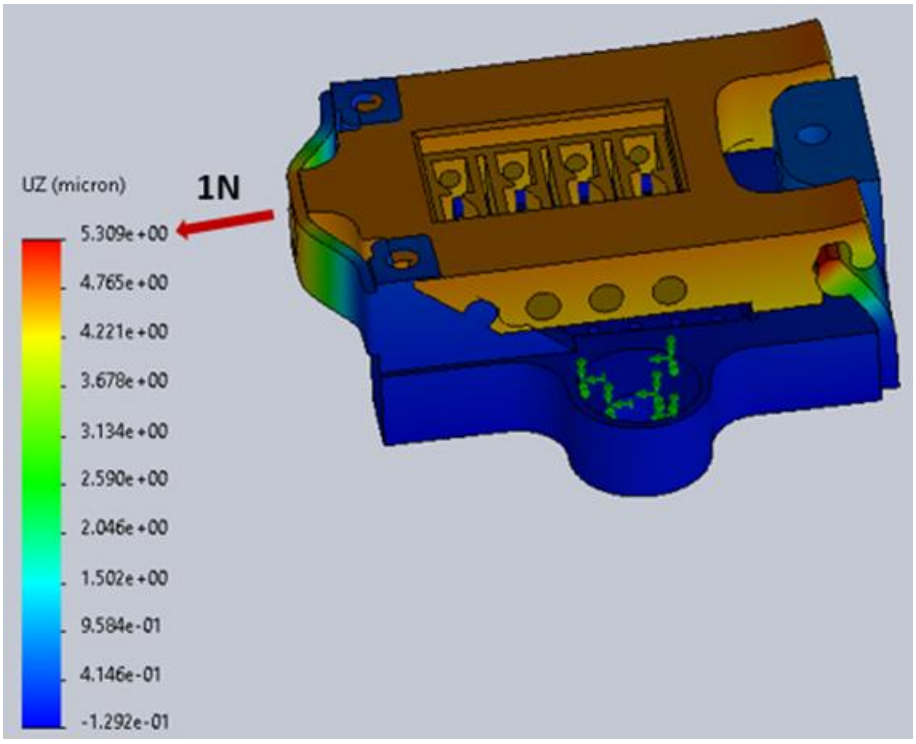

Figure 65: Stiffness Study on Self Aligning Quad SSS

From Figure 65, a fixed constraint was applied to the sensor base to constrain its movement. A standard mesh was used as this is a simple part, and a force of 1 N was applied to the vertical flexures to cause deflection of the shutters.

Nodes (points on the face of each shutter) were selected on each shutter, and the value of each node represents the movement of the individual shutter relative to its sensor.
The base is fixed hence there is no movement. For a force of 1 Newton, the 4 shutters move as shown in Table 12.

Table 12: Movement of shutters on the application of 1 N force

Shutter Nodes	Y1 (UZ (micron))
1	4.34
2	4.33
3	4.32
4	4.36
Range	0.04

6.5. Multi-sensor strain setup

The main application of the novel sensor is for strain monitoring. This can be achieved using the sensor modules and connecting rods as joining members in the same way as the previous design. The joining members provide flexibility over the range of the structure being monitored but are also most prone to thermal error given that environmental temperature variability may be high in embedded machine monitoring applications. To reduce the effect of environmental temperature variability, thermally stable materials are used as the joining members. Invar, Uni-directional CFRP and Zerodur bars are all relatively thermally stable options, but improved performance increases the cost.

To investigate the application of the sensor module for strain measurement, three sensor modules were set up to measure the strain on a fixed structure. The sensor modules were fixed on to the structure being monitored and connected using 200mm long, 10mm square section Zerodur bars because cylindrical rods were not available at the time of the tests. These were used instead of the CFRP rods used previously in order to remove the uncertainty of the thermal expansion from the thermal evaluation of the new sensor module. Two heat pads measuring 28.0 mm by 28.00 mm were inserted at the bottom of the structure to change the temperature of the structure. The heat pads were located 200 mm from both ends of the beam, and the distance between both heat pads was 355 mm. The

structure was caused to expand by heating and the effect of this heat on the triple sensor setup was investigated using finite element analysis (FEA). The model is shown in Figure 66.

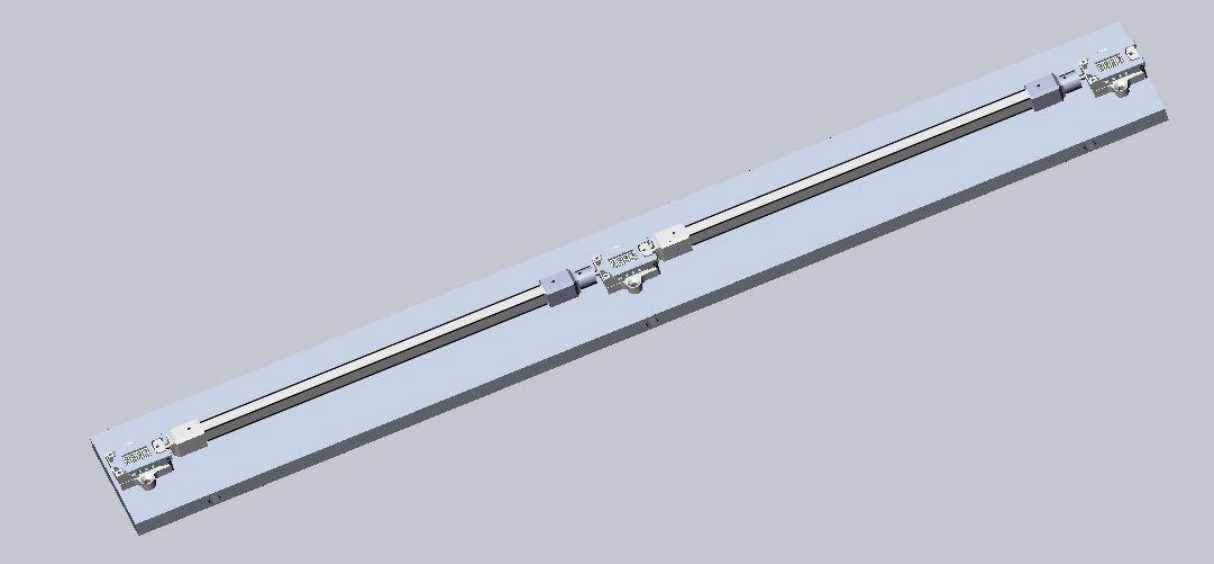

Figure 66: Triple sensor setup overview - improved design

For the transient thermal study, a convection coefficient of 6 W/m/°C was defined on the entire structure. The temperature of the heat pad was specified as 25°C for 3600 seconds to simulate heating of the structure. The transient study showed a steady temperature of 25.00°C on the bottom of the structure and a maximum temperature was attained within 5 minutes. The heat transfer in the contact region was defined using a bonded type of contact resistance of 0 °C/W.

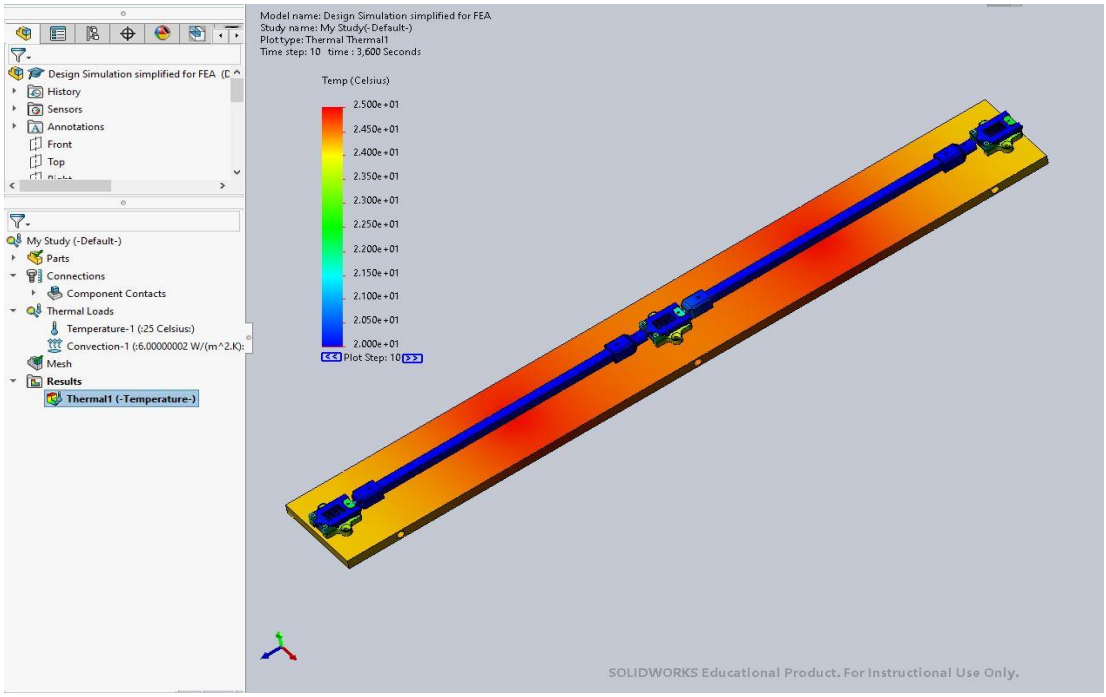

Figure 67: Triple sensor setup overview - strain applied to structure

To evaluate the stresses in the structure due to thermal loading, a linear static study was created. The result of the last step of the transient thermal study was imported into the static study while one end of the structure was fixed.

The strain due to the expansion of the structure was measured as shown in Figure 68.

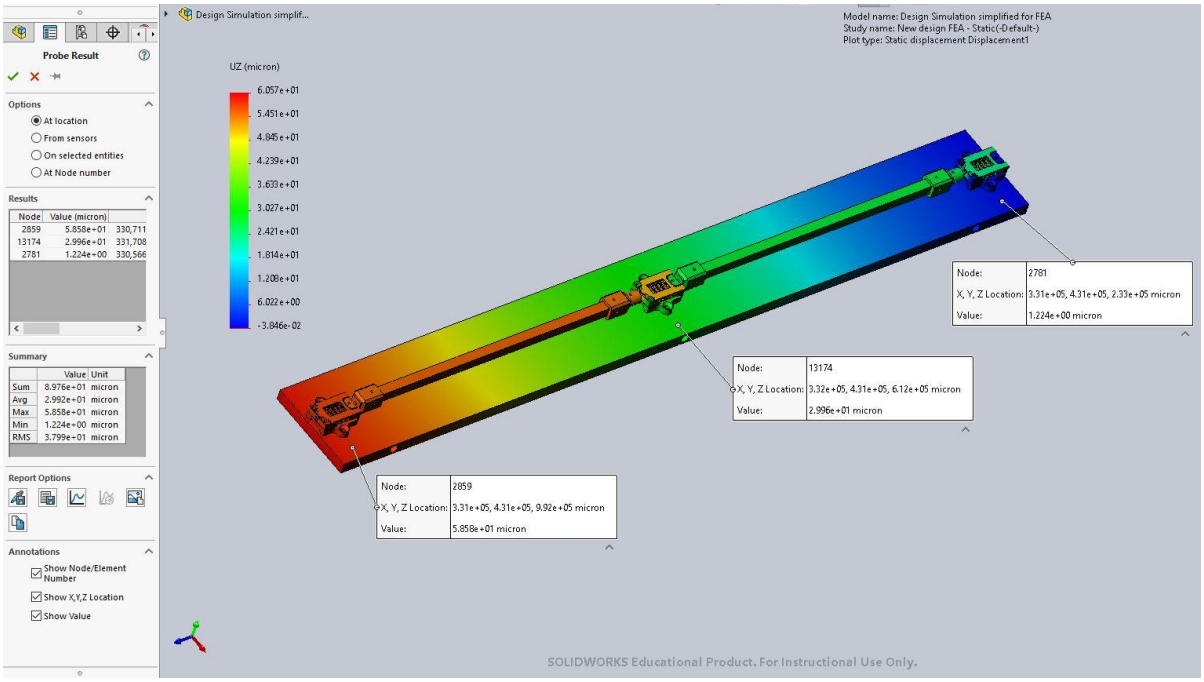

Figure 68: Triple sensor setup overview - strain applied to structure

The strain on the structure between the left sensor and middle sensor was measured as 28.62 µm while that between the middle sensor and right sensor was measured as 28.74 µm. The variability in the results is 6.73 nm which is better than the old design because of the better design of the shutters which improves the alignment.

Table 13: Result for expansion of structure under test

	Structure at 25°C		
	Actual Strain from platform		
	Left sensor module (µm)	Middle Sensor Module (µm)	Right sensor module(µm)
Displacement measured by sensor	58.58	29.96	1.22
Actual strain on structure measured by sensors	0	28.62	28.73

The average strain on the structure measured by the sensors is $\frac{28.62+28.73}{2} = 28.68\ \mu m$.

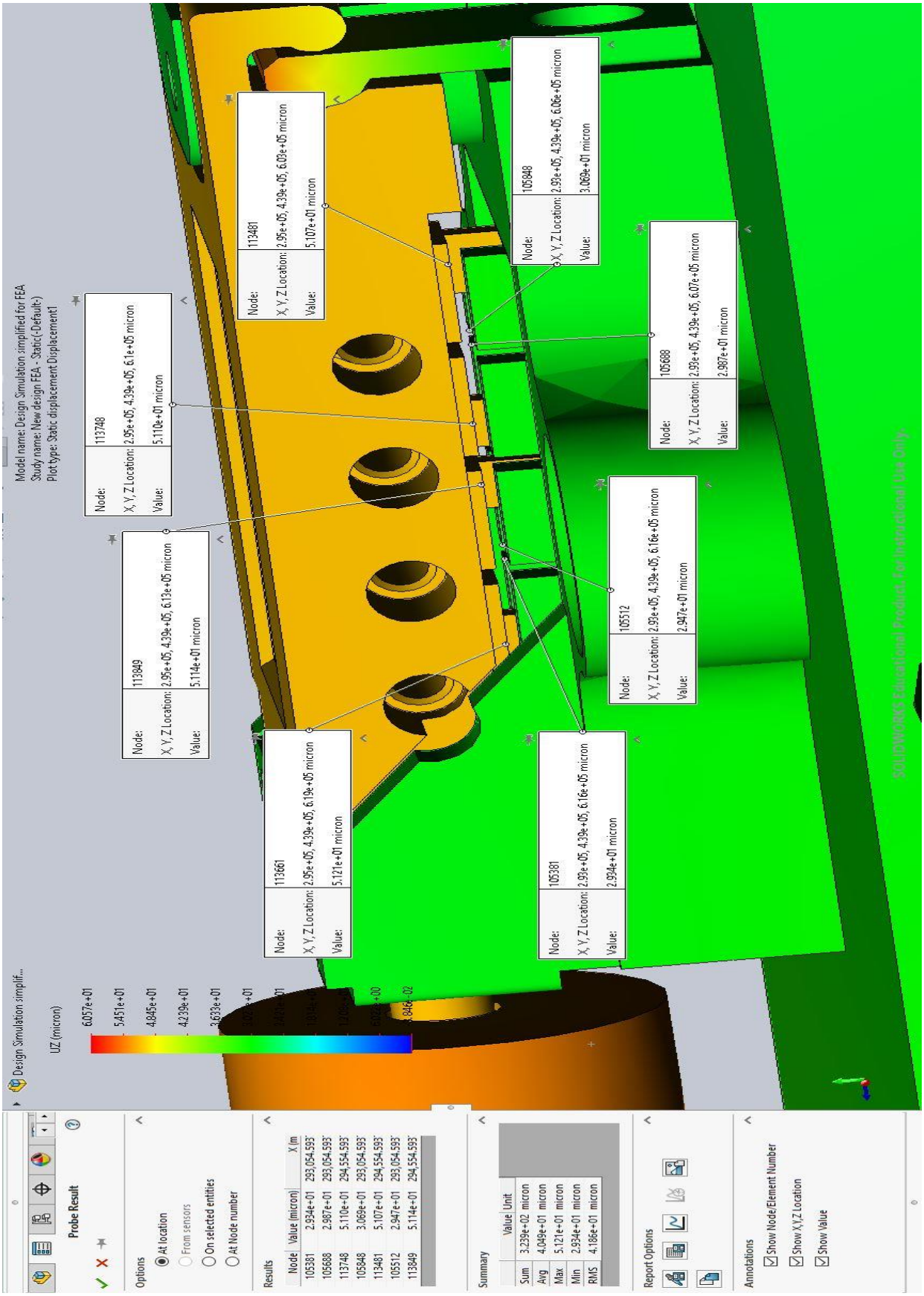

Figure 69: Strain on middle sensor

The actual extension measured by the sensors is presented in Table 14. From the results, the extension measured by the middle sensor and the right sensor are consistent as expected. Again, the main axial flexure of the left sensor is not connected to a rod hence not measuring displacement in the setup.

Table 14: Static displacement on triple sensor setup

Right sensor - Shutter data (µm)				
	Shutter 1	Shutter 2	Shutter 3	Shutter 4
Individual shutter node data	22.99	22.92	22.87	22.85
Average shutter node data	22.91			
Right sensor - Sensor data (µm)				
	SPM 1	SPM 2	SPM 3	SPM 4
SPM node data	1.29	1.35	1.55	2.09
Average node data	1.57			
Average displacement measured by right sensor	21.34			
Middle sensor - Shutter data (µm)				
	Shutter 1	Shutter 2	Shutter 3	Shutter 4
Individual Shutter node data	51.21	51.14	51.1	51.07
Average shutter node data	51.13			
Middle sensor - Sensor data (µm)				
	SPM 1	SPM 2	SPM 3	SPM 4
SPM node data	29.34	29.47	29.87	30.69
Average SPM node data	29.84			
Average displacement measured by middle sensor	21.29			

From Table 13 and Table 14, the strain on the structure is 28.68 µm. The measured strain between the left sensor and the middle sensor is 21.29 µm, while the measured strain between the middle sensor and the right sensor is 21.34 μm . The average strain from both sensors is 21.32 µm.
This shows that the sensors measure about 74% of the actual strain on the structure which illustrates an improved performance than the metal design.

6.6 Validation of Improved Design

The application of the improved 3D printed sensor design was validated using an aluminium cantilever beam. The tests and results are presented in this section.

6.6.1. Description of the Setup

The 3D printed sensor was used in an application to investigate its suitability for strain measurement. The setup consists of an aluminium rectangular beam, Zerodur connecting rods, load masses, granite bed of Zeiss CMM, and a Renishaw XL-80 laser interferometer.
A photograph of the setup used to perform validation experiments is shown in Figure 70.

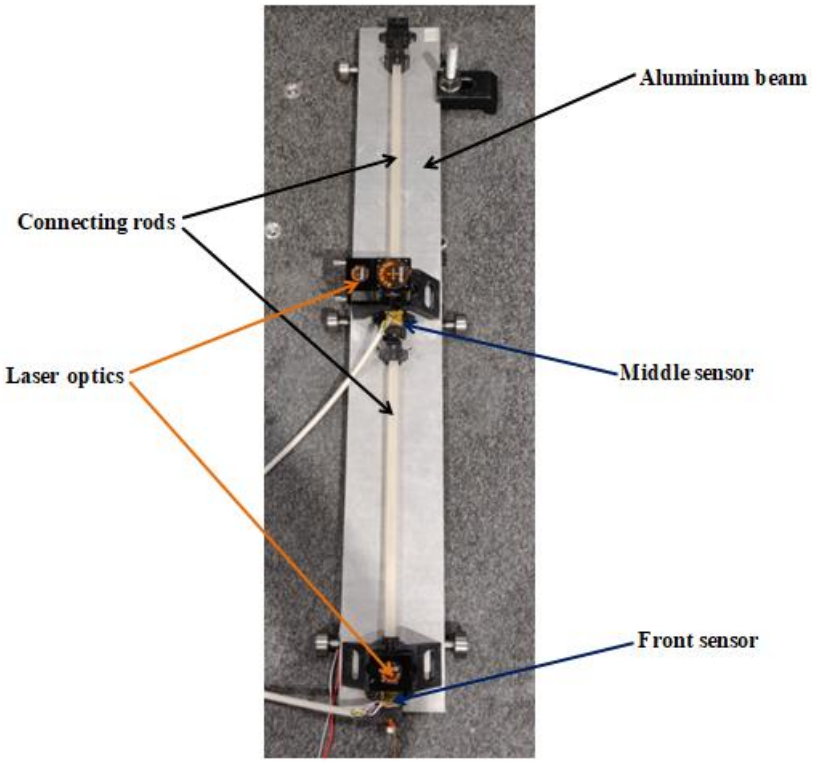

Figure 70: Setup for 3D printed sensor design validation test

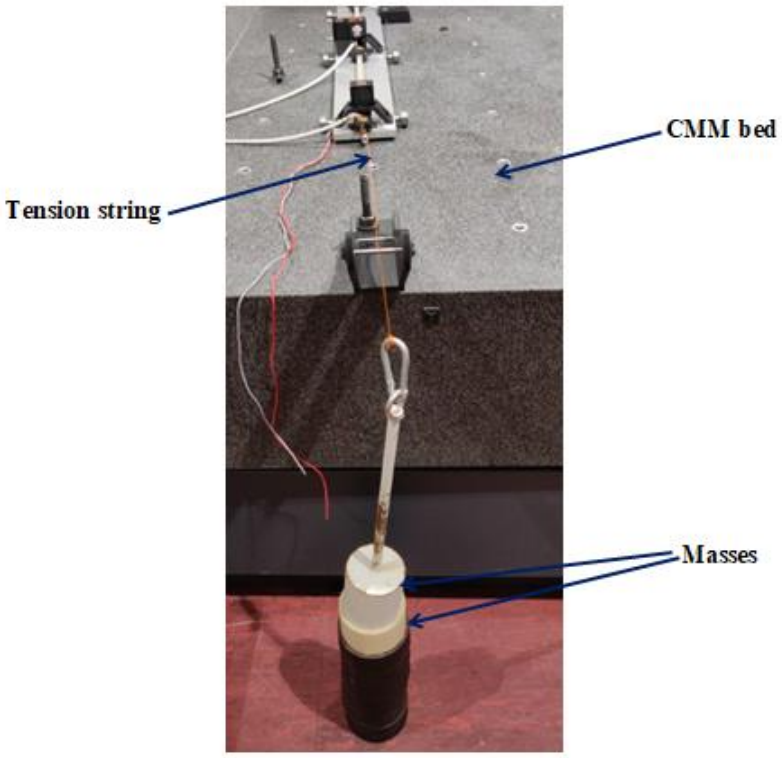

Figure 71: Calibration setup for 3D printed sensor design

A cantilever was created using an aluminium rectangular beam. To avoid shearing, the beam was fastened at one end and loaded at the other with a knife edge. Before the experiment, the mass of the loads was determined using a balance. To detect tensile strain, three SPM sensors were adhered to the surface of the beam with glue. The surface of the beam is cleaned and polished before the strain gauges are attached. Connecting rods of 200 mm were used to connect the SPM sensors. The connecting rods were made of Zerodur to reduce strain due to thermal expansion. The entire setup includes the granite bed of a Coordinate Measuring Machine (CMM) (Zeiss Prismo Access 09/18/09) and a Renishaw XL-80 laser Interferometer system (accuracy: ±0.5 ppm, resolution: 1 nm and range 80 m). The setup was mounted on the CMM bed to provide a mechanically and thermally stable reference for the experiments while the XL80 laser interferometer was provided the traceable independent reference displacement measurements.

This experiment was performed in a temperature-controlled environment, and that together with the setup ensures that thermal effects are greatly minimised.

6.6.2. Calibration of the System

The setup was calibrated by loading the beam in a bi-directional test, and recording the strain measured by the SPM sensors and interferometer. The SPM output was recorded using an in-house developed LabVIEW program. The results were compared with theoretically obtained values for the model.

For a cantilever, tensile strain ε is given by [118]

$$\varepsilon = \frac{6\,mgX}{bh^2E} \qquad [3]$$

where, m is the mass of the load in kilogram, b is width of the cantilever beam (0.1 m), X is the distance from the sensor to the load (0.003 m), h is thickness of the beam (0.012 m), g is the acceleration due to gravity (9.78 m/s^2), and E is Young's modulus of aluminium (69×10^9 N /m^2).

6.6.3. Results and Discussion

Table 15 shows the mathematically obtained strain and sensor voltages for corresponding loads. Figure 72 shows a plot of the calculated strain and output voltage, and the obtained data are fitted with a calibration curve.

Table 15: Calculated strain and sensor output voltages for different loads

Mass (Kg)	Calculated strain (μm)	Front Sensor (V)
0	0	-0.65
2	0.35	-0.61
4	0.71	-0.56
6	1.06	-0.52
8	1.42	-0.5
10	1.77	-0.45
12	2.13	-0.41
14	2.48	-0.38

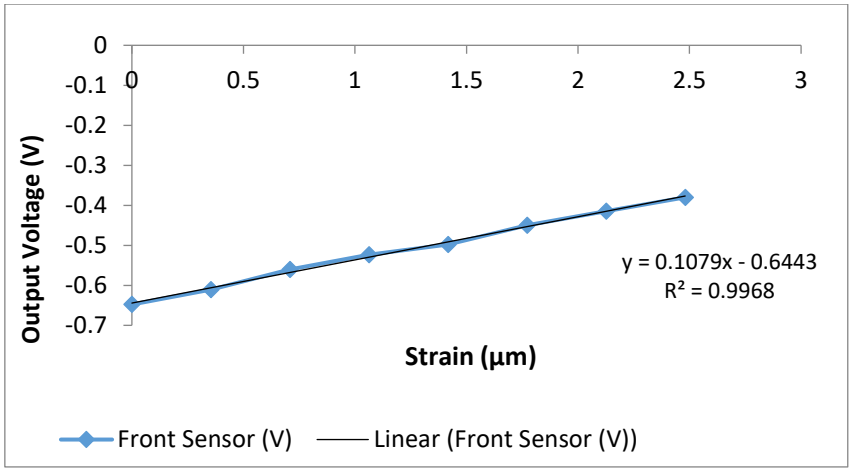

Figure 72: Calibration curve

From Figure 72, the calibration equation is given by

$$y = 0.1079x - 0.6443 \qquad [4]$$

Where x represents the strain and y represents the sensor output voltage. From the calibration equation, the sensitivity of the system is 0.1079 V/µm and the error in output voltage is 5.3 mV.

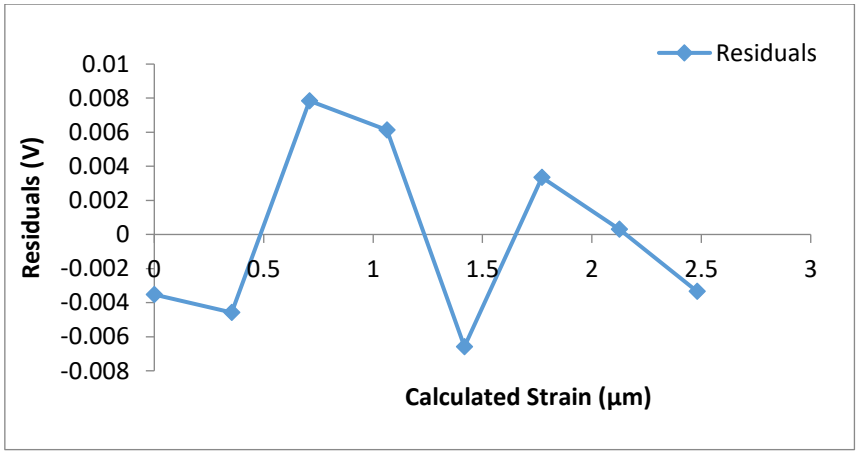

Figure 73: Residuals vs calculated strain plot

The measurements of the parameters m, X, b, and h, all contribute to the error in measurement of tensile strain.

The Figure 74 shows the experimentally obtained curve of the sensor illustrating the SPM head output voltages and XL-80 laser interferometer displacements for corresponding loads in a bidirectional test.

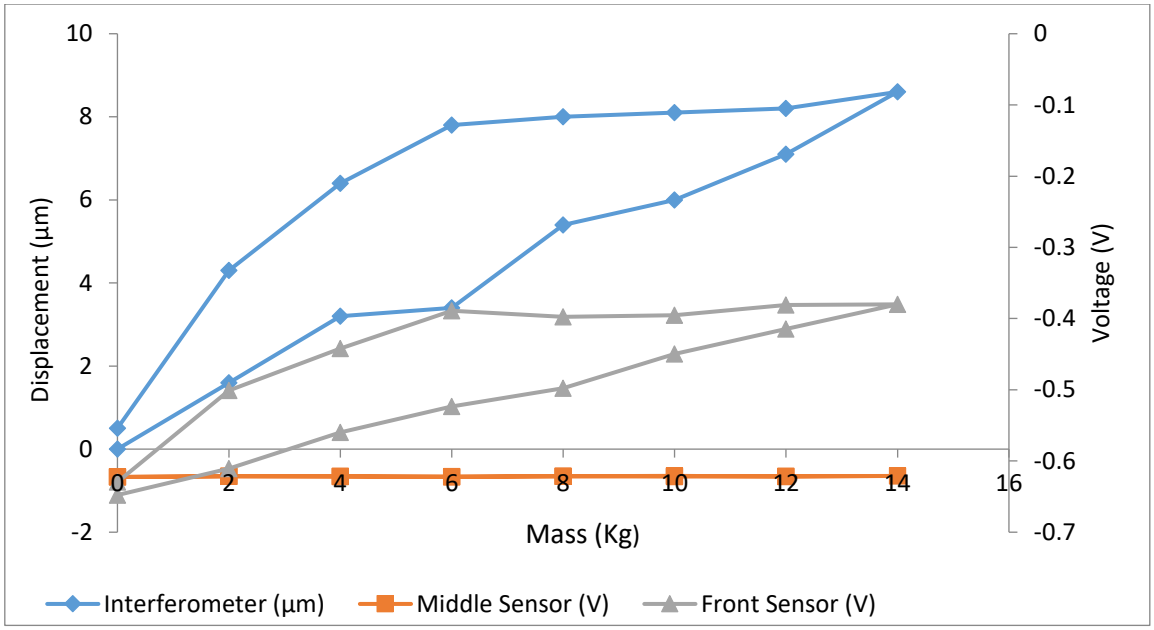

Figure 74: Characteristic curve for bidirectional test

The middle sensor is connected to the fixed sensor hence not measuring strain. It can be seen from Figure 74 that the output of the front sensor is comparable with the reference measurements from the laser. However, it was observed that the output of the laser and the sensor differ by a scaling factor of 4. This magnification is because of the compression of the Zerodur rod as it is strained.

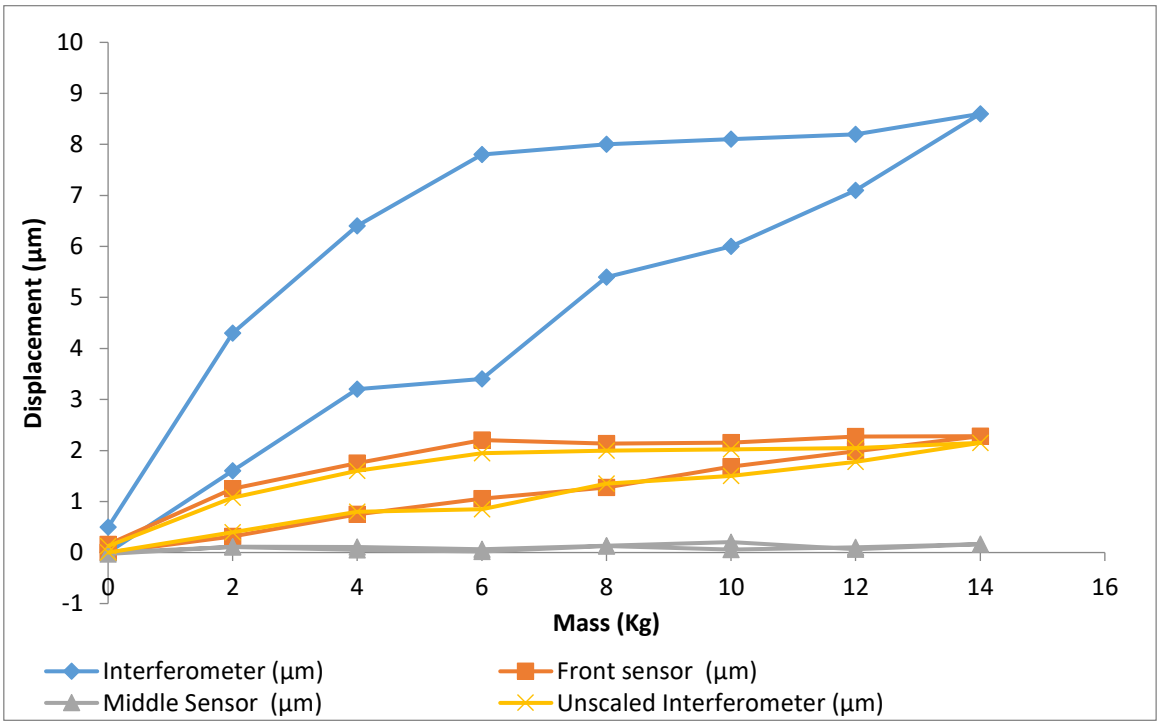

Figure 75: Characteristic curve with magnification removed

Figure 75 shows the result with the magnification factor removed. The results show that there is a strong correlation (R-squared value of 0.98) between the laser measurements and the sensor measurements for corresponding loads. For a load of 14 Kg, the strain is calculated as 2.48 µm, while the laser and SPM sensor measured 2.15 µm and 2.28 µm respectively. The standard deviation of the laser output and the sensor output are 0.73 µm, and 0.81 µm respectively, leaving a standard error of 0.088 µm. The result confirms the suitability of the sensor for strain measurement.

6.7. Sensor cost

Surface mounted sensors, also known as slotted photo-microsensors or photo-interrupters, that are commercially accessible and affordable (1.0 GBP per) were used to create a sensor in this study. Basic electrical components (resistors, capacitors, and connections) and mechanical housing make up the rest of the sensor. After factoring in the cost of plastic and the PCB, the 3D printed sensor was estimated to cost £10 per unit. The signal conditioning circuit consists of standard resistors and capacitors that cost less than 2 GBP. This is much less than the traditionally machined sensor with an estimated manufacturing cost of £800 per unit.

The sensor's output can be used with any conventional data acquisition devices and software. However, an industrial-grade data capture system (usually >= 16bit, high SNR) is preferred; even a good 24-channel system would cost around £600.

This is comparable to inductive, high-quality laser triangulation devices or capacitive cost which cost around £1000 per sensor without associated cost of data acquisition system. A system using the newly designed sensor and fixtures will cost approximately £800, while it will cost approximately £5000 to use capacitive probes for the same system. The dynamic reading unit 4CH, 1000Hz, 100 nm of range costs about 25K CHF.

6.8. Summary

In this chapter, a novel SPM displacement sensor was developed using 3D printing is presented. Sensors manufactured with the 3D printing retain lots of advantages than traditional manufacturing methods. 3D printed sensors can be adapted according to the configuration of the overall system, thus reducing the demand of sensor's rigid mounting interfaces. The 3D printing also reduces the cost of design and shortens the development cycle allowing for rapid translation of a design from concept to a useful device. The sensor design features used to improve strain measurements were explained along with design features in the flexure that increases accuracy and improves mechanical stiffness. The stiffness of the flexure in this design is 0.188 N/µm. Levels of calibration and their resulting accuracy are described. The parameters affecting total error are also discussed.

Measurement results show that the 3D printed SPM displacement sensor is 5 times less stiff and measures 2 times more strain than the traditionally manufactured sensor. Compared to traditional SPM displacement sensor fabrication method, this 3D printed sensor can be fabricated at a lower cost, and the manufacturing process is more convenient and faster.

The practical implications of the tests demonstrated the feasibility of manufacturing parts of more sophisticated structures that are difficult to fabricate using conventional techniques.

Chapter 7 - Conclusion and Future Work

In this chapter, a summary of the research work and the key contributions to knowledge are presented. Suggestions for further research in the subject area are also presented.

7.1. Thesis Summary and Contributions

Machine tool positioning errors have an immediate impact on the dimensional accuracy of manufactured items. Kinematic errors, geometric errors, thermal errors are common error sources. The control of thermally generated machine tool errors is undergoing substantial developments in the manufacturing industry. Many techniques have been investigated based on temperature-based error compensation. However, research has shown that better results can be achieved through direct measurement of structural distortion using a strain sensor for example. Fiber-optic based sensors for example FBGs are being used extensively because of their several advantages. However, they are very expensive, had relatively low resolution, and are susceptible to temperature effects. Hence, a more cost-effective solution with high resolution and low uncertainty is required.

A new design of a sensor based on inexpensive slotted photo microsensor and a differential voltage technique has been created and applied in a framework that can measure deformation of structural components in precision machinery. A flexure system was employed to reduce crosstalk and constrain the relative movement of the sensor parts to 1 DOF which is desirable for displacement sensing. The design of the sensor is compact and thermally evasive, to allow for embedding in structural applications, and to reduce thermal effects.

An aluminium design of the sensor confirmed the differential principle of the sensor, and the simulation results show a stiffness of 2.54 N/ µm. The sensor was investigated through simulation and laboratory tests, for structural monitoring using a framework consisting of carbon fiber connecting rods. The results show a very good 90% correlation with the results of a laser interferometer. The framework that uses this sensor costs about £800 including fixturing, which is very affordable when compared with inductive or capacitive sensors for a similar application.

A PLA 3D printed design of the sensor significantly reduced the cost of manufacturing the sensor to an estimated cost of £10 per unit minus fixturing, resulting in significant cost savings. The sensor design was evaluated through simulation and laboratory test, and the results show a reduced stiffness of 0.188 N/ µm which improved the performance of the sensor for strain monitoring.

The characterisation of the 3D printed sensor revealed a sensitivity of 0.1079 V/ μm, while the use of carbon fiber and Zerodur connecting rods reduced the thermal effects in the monitoring system.
The 3D printed sensor was investigated through simulation and validated through laboratory tests, for monitoring the strain in an aluminium beam using a framework consisting of the SPM sensors and Zerodur connecting rods. The results show excellent correlation of 98% with the results of a laser interferometer, thus confirming the application of the sensor for structural monitoring. A comparison of the result with that obtained from theory and a laser interferometer showed approximately 92% and 94% accuracy respectively.
A comparison of both designs show that the 3D printed design showed a reduced stiffness and measured twice as much strain on a structure as the sensor manufactured from aluminium.

An uncertainty evaluation for a system that employs the sensing framework using the aluminium design achieved a total uncertainty of 4 μm. The largest contributor to the uncertainty was the CTE of carbon fiber rods, and this effect can be reduced by using a material with lower uncertainty.

Finally, two techniques to identify and reduce the errors due to the positioning of the shutters in embedded applications was investigated and results show a 60% reduction in errors. Thus, the novel sensor can be calibrated in-situ resulting in significant cost savings in manufacturing time.

The practical implication of the results of this research is the development of a novel low–cost solution with low uncertainties that can be embedded in structures for distortion monitoring.

The important contributions of this research to knowledge are summarised in the following section.

- The design and analysis of a new displacement sensor that uses very low-cost slotted photomicrosensors (SPM) and works on a differential voltage sensing technique that reduces the effect of some uncertainty contributors.
- The development of a rectilinear framework for measuring structural distortion using the new displacement sensor design and suitable connecting rods. This structural monitoring system is easy to setup, Test results compared with a laser interferometer revealed a high correlation coefficient at zero lag confirming the feasibility of the sensor for structural monitoring.
- Investigation of the sources of uncertainty for a system that uses the newly developed SPM sensors and suitable connecting rods, and the creation of an uncertainty budget. The total uncertainty for the precision designed sensor was estimated at 4 μm.

- Investigation of the sources of uncertainty for a system that uses the newly developed SPM sensors and suitable connecting rods, and the creation of an uncertainty budget. The total uncertainty of the proposed measurement system was estimated as 4 µm. A significant contribution was the CTE of the CFRP connecting rod. This contribution was reduced by using Zerodur bars as the connecting rods.
- Investigation and development of a 3D printable design of the sensor to improve the performance, enable fine adjustment during installation and reduce the manufacturing cost of the sensor to £15. Simulation results show the low stiffness of the flexure design to reduce compression/tension losses in the connection rod. Although Zerodur is brittle and can easily break, its CTE was better suitable for this research work. Invar is another option, but with reduced CTE. The focus of this research was to minimise thermal effects on the setup. The developed 3D printed sensor was shown to measure twice as much strain as the traditionally manufactured sensor.

7.2. Future Work

- The present work can be extended in future studies to increase the range of the sensor. The current research is based on the linear range of the sensor. The sensor range is dependent on the gap between the emitter and detector. The SPM sensor used in this research (KRB021) has a gap of 1 mm while another SPM sensor, the KRB011 has a gap of 2 mm. Together with calibration, the sensor range can be increased for long range displacement measurements to suit a broad range of industrial applications.

- The validation test of the 3D printed sensor design was investigated in this thesis. Further work is expected to ascertain the performance and robustness of the sensor material to varying temperatures. Also, the sensor can be printed using materials with high strength, carbon fiber for example thus creating a more durable sensor for harsh manufacturing environments.

- The present work can be extended to include a characterization and an analysis of the uncertainty contributors for the 3D printed sensor and create an uncertainty budget that shows the significant contributors.

- The current implementation of the sensor is for 1 DoF displacement measurement. The current work can be extended by using a combination of differential measurement, sensor module layout, and signal conditioning to create a new spindle error monitoring device.

References

1. Qin, Y., et al., *Micro-manufacturing: research, technology outcomes and development issues.* International journal of advanced manufacturing technology, 2009. **47**(9-12): p. 821-837.
2. Ramesh, R., M.A. Mannan, and A.N. Poo, *Error compensation in machine tools — a review: Part I: geometric, cutting-force induced and fixture-dependent errors.* International Journal of Machine Tools and Manufacture, 2000. **40**(9): p. 1235-1256.
3. *BS EN ISO 10360-1:2001: Geometrical product specifications (GPS). Acceptance and reverification tests for coordinate measuring machines (CMM). Vocabulary*. 2001, British Standards Institute.
4. Bryan, J.B., *International Status of Thermal Error Research.* CIRP Annals, 1967.
5. Weck, M., *Handbook of machine tools: Vol.4, Metrological analysis and performance tests*. 1984, Chichester: Wiley.
6. Mayr, J., et al., *Thermal issues in machine tools.* CIRP annals, 2012. **61**(2): p. 771-791.
7. Bryan, J., *International Status of Thermal Error Research (1990).* CIRP annals, 1990. **39**(2): p. 645-656.
8. Longstaff, A.P., S. Fletcher, and D.G. Ford, *Practical Experience Of Thermal Testing With Reference To IS0 230 Part 3.* WIT Transactions on Engineering Sciences, 2003. **44**.
9. Abdulshahed, A.M., et al., *Thermal error modelling of a gantry-type 5-axis machine tool using a Grey Neural Network Model.* Journal of manufacturing systems, 2016. **41**: p. 130-142.
10. Tan, B., et al., *A thermal error model for large machine tools that considers environmental thermal hysteresis effects.* International Journal of Machine Tools and Manufacture, 2014. **82-83**: p. 11-20.
11. White, A.J., S.R. Postlethwaite, and D.G. Ford, *A General Purpose Thermal Error Compensation System For CNC Machine Tools.* WIT Transactions on Engineering Sciences, 2001. **34**.
12. Ko, T.J., T.W. Gim, and J.Y. Ha, *Particular behavior of spindle thermal deformation by thermal bending.* International Journal of Machine Tools and Manufacture, 2003. **43**(1): p. 17-23.
13. Postlethwaite, S.R., J.P. Allen, and D.G. Ford, *Machine tool thermal error reduction—an appraisal.* Proceedings of the Institution of Mechanical Engineers, Part B: Journal of Engineering Manufacture, 1999. **213**(1): p. 1-9.
14. Thomas R Hicks, P.D.A., *The Nanopositioning Book*. 1997: Queensgte Instruments Ltd.
15. E. Uhlmann, M.P. *Compensation of Thermal Deformations at Machine Tools using Adaptronic CRP-Structures*. in *CIRP Conference on Manufacturing Systems: Manufacturing Systems and Techniques for the New Front*. 2008.
16. Merloa, A., et al., *Application of composite materials for lightweight and smart structures design of high performance milling machines*
17. Ni, J., *CNC Machine Accuracy Enhancement Through Real-Time Error Compensation.* Journal of manufacturing science and engineering, 1997. **119**(4B): p. 717-725.
18. Aggogeri, F., et al., *A kinematic model to compensate the structural deformations in machine tools using fiber Bragg grating (FBG) sensors.* Applied Sciences (Switzerland), 2017. **7**(2): p. 114.
19. Fujishima, M., et al., *Thermal displacement reduction and compensation of a turning center.* CIRP Journal of Manufacturing Science and Technology, 2018. **22**: p. 111-115.
20. J.P. Allen, S.R.P.a.D.G.F., *Practical Application Of Thermal Error Correction - 4 Case Studies*, in *LAMDAMAP*. 1997. p. 11.
21. Mian, N.S., *Efficient machine tool thermal error modelling strategy for accurate offline assessment*. 2010, University of Huddersfield.

22. Potdar, A., *REDUCING THE UNCERTAINTY OF THERMAL MODEL CALIBRATION USING ON-MACHINE PROBING AND DATA FUSION*, in *Computing and Engineering*. 2016, University of Huddersfield. p. 117.
23. Zhan-Qiang, L., P.K. Venuvinod, and V.A. Ostafiev, *On-machine measurement of workpieces with the cutting tool.* Integrated Manufacturing Systems, 1998. **9**(3): p. 168-172.
24. Huang, N., et al., *Error compensation for machining of large thin-walled part with sculptured surface based on on-machine measurement.* International journal of advanced manufacturing technology, 2018. **96**(9-12): p. 4345-4352.
25. Imkamp, D., et al., *Challenges and trends in manufacturing measurement technology – the "Industrie 4.0" concept.* Journal of sensors and sensor systems, 2016. **5**(2): p. 325-335.
26. Karadayi, R. *In Process Closed Loop Metrology for Adaptive Manufacturing*. in *Annual Workshop and Conference*. 2014. Toronto, Canada.
27. Choi, J.P., B.K. Min, and S.J. Lee, *Reduction of machining errors of a three-axis machine tool by on-machine measurement and error compensation system.* Journal of Materials Processing Tech, 2004. **155-156**: p. 2056-2064.
28. Schwenke, H. *Large parts with critical tolerances: Concepts and possible solutions for traceable CMM measurements on machine tools*. in *Traceable in-Process Dimensional Measurement Final Workshop*. 2015.
29. Mutilba, U., et al., *Traceability of on-machine tool measurement: Uncertainty budget assessment on shop floor conditions.* Measurement, 2019. **135**: p. 180-188.
30. Slocum, A.H. *Precision machine design: macromachine design philosophy and its applicability to the design of micromachines*. in *[1992] Proceedings IEEE Micro Electro Mechanical Systems*. 1992. IEEE.
31. Ross-Pinnock, D. and P.G. Maropoulos, *Identification of Key Temperature Measurement Technologies for the Enhancement of Product and Equipment Integrity in the Light Controlled Factory.* Procedia CIRP, 2014. **25**: p. 114-121.
32. Arena, M. and M. Viscardi, *Strain State Detection in Composite Structures: Review and New Challenges.* Journal of Composites Science, 2020. **4**(2): p. 60.
33. Takeda, N., S. Minakuchi, and T. Nadabe. *Distributed strain monitoring for damage evolution in CFRP bolted structures with embedded optical fibers*.
34. CORP, N.I. *Measuring Strain with Strain Gages*. 2020 July 15, 2020 [cited 2019 February 20, 2019]; Available from: https://www.ni.com/en-gb/innovations/white-papers/07/measuring-strain-with-strain-gages.html.
35. Tönük, E., *Strain measurement and electric resistance strain gauges*. 2012.
36. Nur, R., et al., *A Highly Sensitive Capacitive-type Strain Sensor Using Wrinkled Ultrathin Gold Films.* Nano letters, 2018. **18**(9): p. 5610-5617.
37. Zlebic, C., et al. *Comparison of resistive and capacitive strain gauge sensors printed on polyimide substrate using ink-jet printing technology*. IEEE.
38. Sharpe, J.W.N., *Springer Handbook of Experimental Solid Mechanics*. 1st 2008. ed. 2008, New York, NY: Springer US.
39. Zhang, J.X.J. and K. Hoshino, *Molecular sensors and nanodevices: principles, designs and applications in biomedical engineering*. Second ed. 2019, London, England: Academic Press.
40. Fleming, A.J., *A review of nanometer resolution position sensors: Operation and performance.* Sensors and actuators. A. Physical., 2013. **190**: p. 106-126.
41. Shintake, J., et al., *Ultrastretchable Strain Sensors Using Carbon Black-Filled Elastomer Composites and Comparison of Capacitive Versus Resistive Sensors.* Advanced materials technologies, 2018. **3**(3): p. 1700284-n/a.
42. Amjadi, M., et al., *Stretchable, Skin-Mountable, and Wearable Strain Sensors and Their Potential Applications: A Review.* Advanced functional materials, 2016. **26**(11): p. 1678-1698.

43. Lee, C.E. and H.F. Taylor. *Interferometric fiber optic temperature sensor using a low-coherence light source*. 1990. SPIE.
44. Rao, Y.-J., *Recent progress in fiber-optic extrinsic Fabry–Perot interferometric sensors.* Optical Fiber Technology, 2006. **12**(3): p. 227-237.
45. Rao, Y.J., J. Jiang, and C.X. Zhou, *Spatial-frequency multiplexed fiber-optic Fizeau strain sensor system with optical amplification.* Sensors and Actuators A: Physical, 2005. **120**(2): p. 354-359.
46. Rajibul Islam, M., et al., *Chronology of fabry-perot interferometer fiber-optic sensors and their applications: A review.* Sensors (Basel, Switzerland), 2014. **14**(4): p. 7451-7488.
47. Campanella, C.E., et al., *Fibre Bragg Grating based strain sensors: Review of technology and applications.* Sensors (Basel, Switzerland), 2018. **18**(9): p. 3115.
48. Akshay Anand Potdar, S.F., Andrew P. Longstaff, *Performance characterisation of a new photo-microsensor based sensing head for displacement measurement.* Sensors and Actuators, 2016(239): p. 60-70.
49. Hongbo Wang, Z.F., *Ultrastable and highly sensitive eddy current displacement sensor using self-temperature compensation.* Sensors and Actuators, 2013. **203**: p. 362-368.
50. Missoffe, A., et al., *New simple optical sensor: From nanometer resolution to centimeter displacement range.* Sensors and actuators. A. Physical., 2012. **176**(176): p. 46-52.
51. Berkovic, G. and E. Shafir, *Optical methods for distance and displacement measurements.* Advances in Optics and Photonics, 2012. **4**(4): p. 441-471.
52. Shieh, J., et al., *The selection of sensors.* Progress in Materials Science, 2001. **46**(3): p. 461-504.
53. Li, Q. and F. Ding, *Novel displacement eddy current sensor with temperature compensation for electrohydraulic valves.* Sensors and actuators. A. Physical., 2005. **122**(1): p. 83-87.
54. Zhang, S. and S. Kiyono, *An absolute calibration method for displacement sensors.* Measurement, 2001. **29**(1): p. 11-20.
55. Khiat, A., et al., *High-resolution fibre-optic sensor for angular displacement measurements.* Measurement science & technology, 2010. **21**(2): p. 025306.
56. Haitjema, H., P.H.J. Schellekens, and S.F.C.L. Wetzels, *Calibration of displacement sensors up to 300 m with nanometre accuracy and direct traceability to a primary standard of length.* Metrologia, 2000. **37**(1): p. 25-33.
57. L. A. Ferreira, A.B.L.R., J. L. Santos, and I;. Farahi, *Simultaneous measurement of displacement and temperature using a low finesse cavity and a fiber Bragg grating.* IEEE photonics technology letters, 1996. **8**(11).
58. Yang, H., et al. *The study of high accuracy capacitive displacement sensor used in non-contact precision displacement measurement*. IEEE.
59. Peng, Y., et al., *A Cr-N thin film displacement sensor for precision positioning of a micro-stage.* Sensors and Actuators A: Physical, 2014. **211**: p. 89-97.
60. Maekawa, A., et al., *Experimental validation of non-contacting measurement method using LED-optical displacement sensors for vibration stress of small-bore piping.* Measurement, 2015. **71**: p. 1-10.
61. Delmas, J.R., *Optoelectronic displacement sensor*. 1982, Google Patents.
62. Kaufmann, M., et al., *Optoelectronic displacement sensor with correction filter*. 1989, Google Patents.
63. Shan, Y., J.E. Speich, and K.K. Leang, *Low-Cost IR Reflective Sensors for Submicrolevel Position Measurement and Control.* IEEE/ASME Transactions on Mechatronics, 2008. **13**(6): p. 700-709.
64. Lin, F., S.T. Smith, and G. Hussain, *Optical fiber displacement sensor and its application to tuning fork response measurement.* Precision Engineering, 2012. **36**(4): p. 620-628.

65. Li, J., H. Neumann, and R. Ramalingam, *Design, fabrication, and testing of fiber Bragg grating sensors for cryogenic long-range displacement measurement.* Cryogenics, 2015. **68**: p. 36-43.
66. Majumder, M., et al., *Fibre Bragg gratings in structural health monitoring—Present status and applications.* Sensors and Actuators A: Physical, 2008. **147**(1): p. 150-164.
67. Components, R. *KRB021 Kingbright, Surface Mount Slotted Optical Switch, Phototransistor Output*. [cited 2017 April 27, 2017]; Available from: https://uk.rs-online.com/web/p/slotted-optical-switches/6165692/.
68. OMRON. *Micro Sensing Device Data Book SPM Characteristics*. [cited 2021 May]; Available from: file:///C:/Users/user/Documents/For%20Uncertainty%20Chapter/Micro%20Sensing%20Device%20Data%20Book%20SPM%20Characteristics.pdf.
69. Ge, Y., et al., *The response of embedded strain sensors in concrete beams subjected to thermal loading.* Construction & building materials, 2014. **70**: p. 279-290.
70. Bruzzone, L. and G. Bozzini, *A flexible joints microassembly robot with metamorphic gripper.* Assembly automation, 2010. **30**(3): p. 240-247.
71. Dong, J., D. Mukhopadhyay, and P.M. Ferreira, *Design, fabrication and testing of a silicon-on-insulator (SOI) MEMS parallel kinematicsXYstage.* Journal of Micromechanics and Microengineering, 2007. **17**(6): p. 1154-1161.
72. Radgolchin, M. and H. Moeenfard, *Load-displacement behavior of fundamental flexure modules interconnected with compliant elements.* Mechanism and Machine Theory, 2018. **120**: p. 120-139.
73. Hazelton, A.J., *Flexures: elements of elastic mechanisms.* Precision engineering, 2002. **26**(1): p. 137-138.
74. Nijenhuis, M., J.P. Meijaard, and D.M. Brouwer, *Misalignments in an overconstrained flexure mechanism: A cross-hinge stiffness investigation.* Precision engineering, 2020. **62**: p. 181-195.
75. Awtar, S., J. Ustick, and S. Sen, *An XYZ Parallel-Kinematic Flexure Mechanism With Geometrically Decoupled Degrees of Freedom.* Journal of Mechanisms and Robotics, 2012. **5**(1).
76. Noll, T., et al., *Parallel kinematics for nanoscale Cartesian motions.* Precision Engineering, 2009. **33**(3): p. 291-304.
77. Kang, D. and D. Gweon, *Analysis and design of a cartwheel-type flexure hinge.* Precision Engineering, 2013. **37**(1): p. 33-43.
78. Potdar, A., et al., *Development of modular machine tool structural monitoring system*. 2013, KTH Royal Institute of Technology.
79. Torralba, M., et al., *Design Optimization for the Measurement Accuracy Improvement of a Large Range Nanopositioning Stage.* Sensors (Basel, Switzerland), 2016. **16**(1): p. 84.
80. Roths, J., et al. *Strain calibration of optical FBG-based strain sensors*. Bellingham, Wash: SPIE.
81. Habel, W.R., et al. *Guidelines for the characterization and use of fibre optic sensors: basic definitions and a proposed standard for FBG-based strain sensors*. Bellingham, Wash: SPIE.
82. Kramar, J.A., *Nanometre resolution metrology with the Molecular Measuring Machine.* Measurement Science and Technology, 2005. **16**(11): p. 2121-2128.
83. JCGM, *Evaluation of Measurement Data - Guide to the Expression of Uncertainty in Measurement*. 2008, BIPM.
84. Herschy, R.W., *The uncertainty in a current meter measurement.* Flow measurement and instrumentation, 2002. **13**(5): p. 281-284.
85. Hernandez, W. and J. de Vicente, *Measurement uncertainty estimation of a robust photometer circuit.* Sensors (Basel, Switzerland), 2009. **9**(4): p. 3149-3160.

86. Haitjema, H., *The Calibration of Displacement Sensors.* 2020. **20**(3): p. 584.
87. PLC, R. *ML 10 Gold Standard Laser System*. 2000-2002 September 14, 2018]; Available from: http://www.cmm-mexico.com/dl/L-8003-2456.pdf.
88. Park, J., G. Nam, and J. Choi, *Parameters in cause and effect diagram for uncertainty evaluation.* Accreditation and Quality Assurance, 2011. **16**(6): p. 325-326.
89. Sharma, G. and P.S. Rao, *Process capability improvement of an engine connecting rod machining process.* Journal of industrial engineering international, 2013. **9**(1): p. 1-9.
90. Mahto, D. and A. Kumar, *Application of root cause analysis in improvement of product quality and productivity.* Journal of industrial engineering and management, 2008. **1**(2): p. 16.
91. Lehtinen, T.O.A., et al., *Diagrams or structural lists in software project retrospectives – An experimental comparison.* The Journal of systems and software, 2015. **103**: p. 17-35.
92. Possetti, G.R.C., et al., *Metrological Evaluation of Optical Fiber Grating-Based Sensors: An Approach Towards the Standardization.* Journal of Lightwave Technology, 2012. **30**(8): p. 1042-1052.
93. Fleming, A.J., *A review of nanometer resolution position sensors: Operation and performance.* Sensors and Actuators, 2013. **190**: p. 106-126.
94. *NIST/SEMATECH statisticians demonstrate Internet engineering statistics handbook.* Journal of research of the National Institute of Standards and Technology, 1998. **103**(3): p. 347.
95. JCGM, *International vocabulary of metrology – Basic and general concepts and associated terms (VIM)*. 2012.
96. Ltd, E.C. *1mm Carbon Fibre Rod*. [cited 2022; Available from: https://www.easycomposites.co.uk/1mm-carbon-fibre-rod.
97. A. Kato, K.G., Y. Kogo, R. Inoue. *CHANGES IN THERMAL EXPANSION COEFFICIENT OF CFRP LAMINATE DUE TO THERMAL CYCLE*. in *International Conference on Composite Materials*. 2017.
98. Dong, C., et al., *Evaluation of thermal expansion coefficient of carbon fiber reinforced composites using electronic speckle interferometry.* Optics express, 2018. **26**(1): p. 531-543.
99. Bell, D.J., et al., *MEMS actuators and sensors: observations on their performance and selection for purpose.* Journal of Micromechanics and Microengineering, 2005. **15**(7): p. S153-S164.
100. ISO/IEC, *International Vocabulary of Metrology –Basic and General Concepts and Associated Terms (VIM)*. 2008.
101. Petrò, S., *A double shift self-calibration method for micro XY stages.* Precision Engineering, 2019. **56**: p. 476-484.
102. Buonadonna, P., et al. *TASK: sensor network in a box*. in *Proceeedings of the Second European Workshop on Wireless Sensor Networks, 2005.* 2005.
103. Hasenfratz, D., O. Saukh, and L. Thiele. *On-the-Fly Calibration of Low-Cost Gas Sensors*. 2012. Berlin, Heidelberg: Springer Berlin Heidelberg.
104. Spinelle, L., et al., *Field calibration of a cluster of low-cost available sensors for air quality monitoring. Part A: Ozone and nitrogen dioxide.* Sensors and Actuators B: Chemical, 2015. **215**: p. 249-257.
105. Tan, R., et al., *System-level calibration for data fusion in wireless sensor networks.* ACM Trans. Sen. Netw., 2013. **9**(3): p. Article 28.
106. Barcelo-Ordinas, J.M., et al., *Self-calibration methods for uncontrolled environments in sensor networks: A reference survey.* Ad hoc networks, 2019. **88**: p. 142-159.
107. Kotsev, A., et al., *Next Generation Air Quality Platform: Openness and Interoperability for the Internet of Things.* Sensors (Basel, Switzerland), 2016. **16**(3): p. 403.
108. Sharma, A., L. Golubchik, and R. Govindan, *Sensor faults: Detection methods and prevalence in real-world datasets.* ACM transactions on sensor networks, 2010. **6**(3): p. 1-39.

109. Ni, K., et al., *Article 25 (29 pages)-Sensor Network Data Fault Types.* ACM Transactions on Sensor Networks, 2009(3).
110. Balzano, L. and R. Nowak. *Blind Calibration of Sensor Networks*. IEEE.
111. Evans, C.J., R.J. Hocken, and W.T. Estler, *Self-Calibration: Reversal, Redundancy, Error Separation, and 'Absolute Testing'.* CIRP Annals - Manufacturing Technology, 1996. **45**(2): p. 617-634.
112. Fletcher Simon, C.D., Furness Thomas, Longstaff Andrew, *Design of a structural strain measurement system based on slotted photomicrosensors*, in *14th International Conference and Exhibition on Laser Metrology, Coordinate Measuring Machine and Machine Tool Performance*. March 11, 2021, Euspen.
113. Mathew, E., et al., *Fused Deposition Modelling as a Potential Tool for Antimicrobial Dialysis Catheters Manufacturing: New Trends vs. Conventional Approaches.* Coatings (Basel), 2019. **9**(8): p. 515.
114. Shahrubudin, N., T.C. Lee, and R. Ramlan, *An Overview on 3D Printing Technology: Technological, Materials, and Applications.* Procedia manufacturing, 2019. **35**: p. 1286-1296.
115. Eneko Larran˜ eta, J.D.-R., and Dimitrios A. Lamprou *Additive Manufacturing Can Assist in the Fight Against COVID-19 and Other Pandemics and Impact on the Global Supply Chain* 3DPrinting and Additive Manufacturing, 2020. **7**.
116. Kesner, S.B. and R.D. Howe, *Design Principles for Rapid Prototyping Forces Sensors Using 3-D Printing.* IEEE/ASME transactions on mechatronics, 2011. **16**(5): p. 866-870.
117. Li, B., et al., *Rapid prototyping eddy current sensors using 3D printing.* Rapid prototyping journal, 2018. **24**(1): p. 106-113.
118. Abbaspour-Gilandeh, Y. and M. Khanramaki, *Design, Construction and Calibration of a Triaxial Dynamometer for Measuring Forces and Moments Applied on Tillage Implements in Field Conditions.* MĀPAN : journal of Metrology Society of India, 2013. **28**(2): p. 119-127.

Appendices

Table A - 1: Node data on SPM surface

	Node Data on SPM surface (µm)		
	Left Sensor Module	Middle Sensor Module	Right Sensor Module
	-0.250	-0.686	-1.119
	-0.252	-0.688	-1.121
	-0.250	-0.686	-1.119
	-0.252	-0.688	-1.121
	-0.252	-0.688	-1.121
	-0.250	-0.686	-1.119
	-0.251	-0.687	-1.121
	-0.252	-0.687	-1.121
	-0.251	-0.687	-1.121
Average	-0.251	-0.687	-1.120

Taking the left sensor module for example, the column labelled ‘left sensor module’ represent points on the surface of one of the sensors in the module.

Table A - 2: Node data on shutter surface

	Node Data on shutter (µm)		
	Left Sensor Module	Middle Sensor Module	Right Sensor Module
	-0.56818	-0.99364	-1.1161
	-0.56845	-0.9946	-1.1174
	-0.56792	-0.99264	-1.1148
	-0.56793	-0.99268	-1.1148
	-0.56845	-0.9946	-1.1174
	-0.56793	-0.99266	-1.1148
	-0.56845	-0.9946	-1.1174
	-0.56819	-0.99363	-1.1161
	-0.56832	-0.99412	-1.1167
	-0.56806	-0.99315	-1.1154
	-0.56805	-0.99314	-1.1154
	-0.56832	-0.99412	-1.1167
Average	-0.5681875	-0.993631667	-1.11608333

The column labelled ‘left sensor module’ represent points on the corresponding shutter of the sensor in. These points are used to monitor the movement of the shutter relative to the sensor.

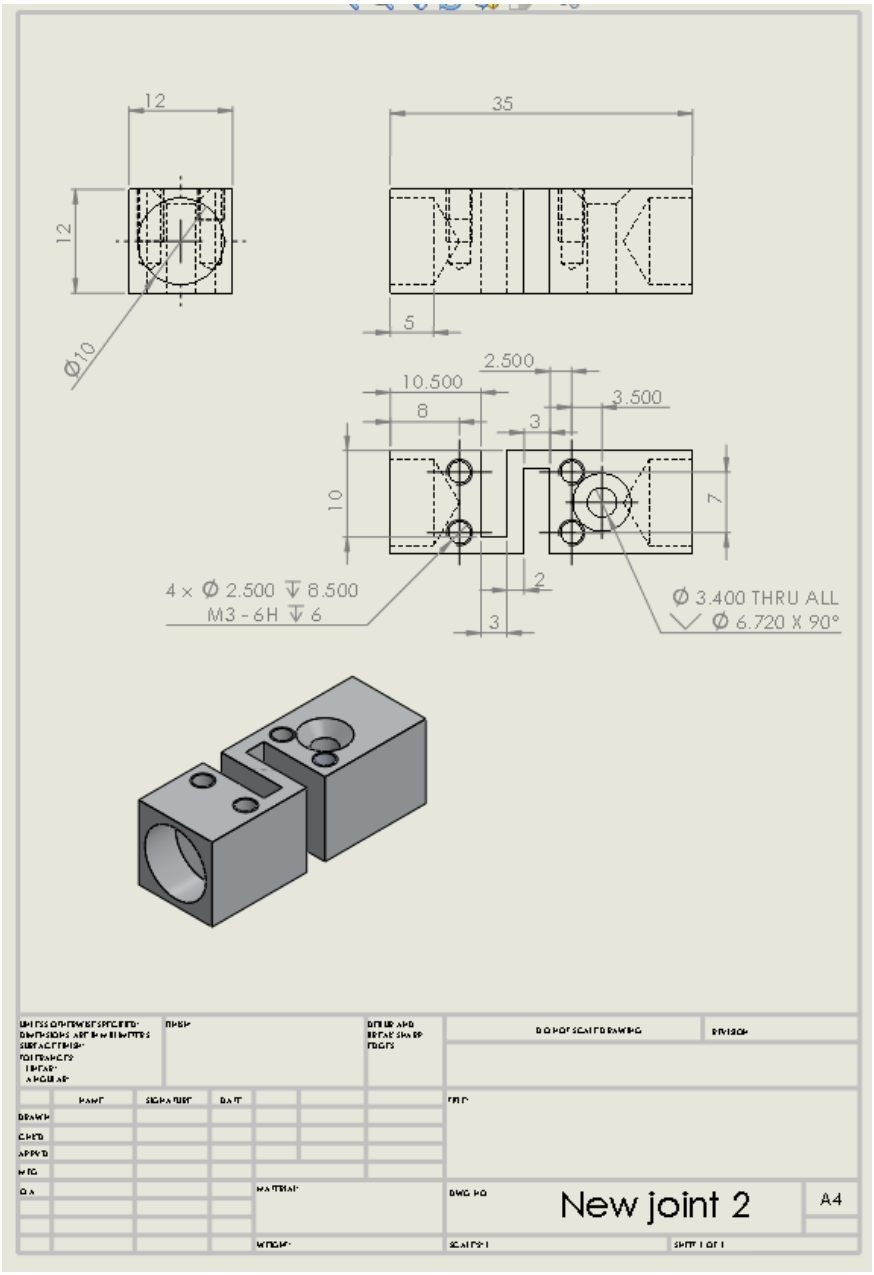

Figure A - 1: Multistrain flexure joint design

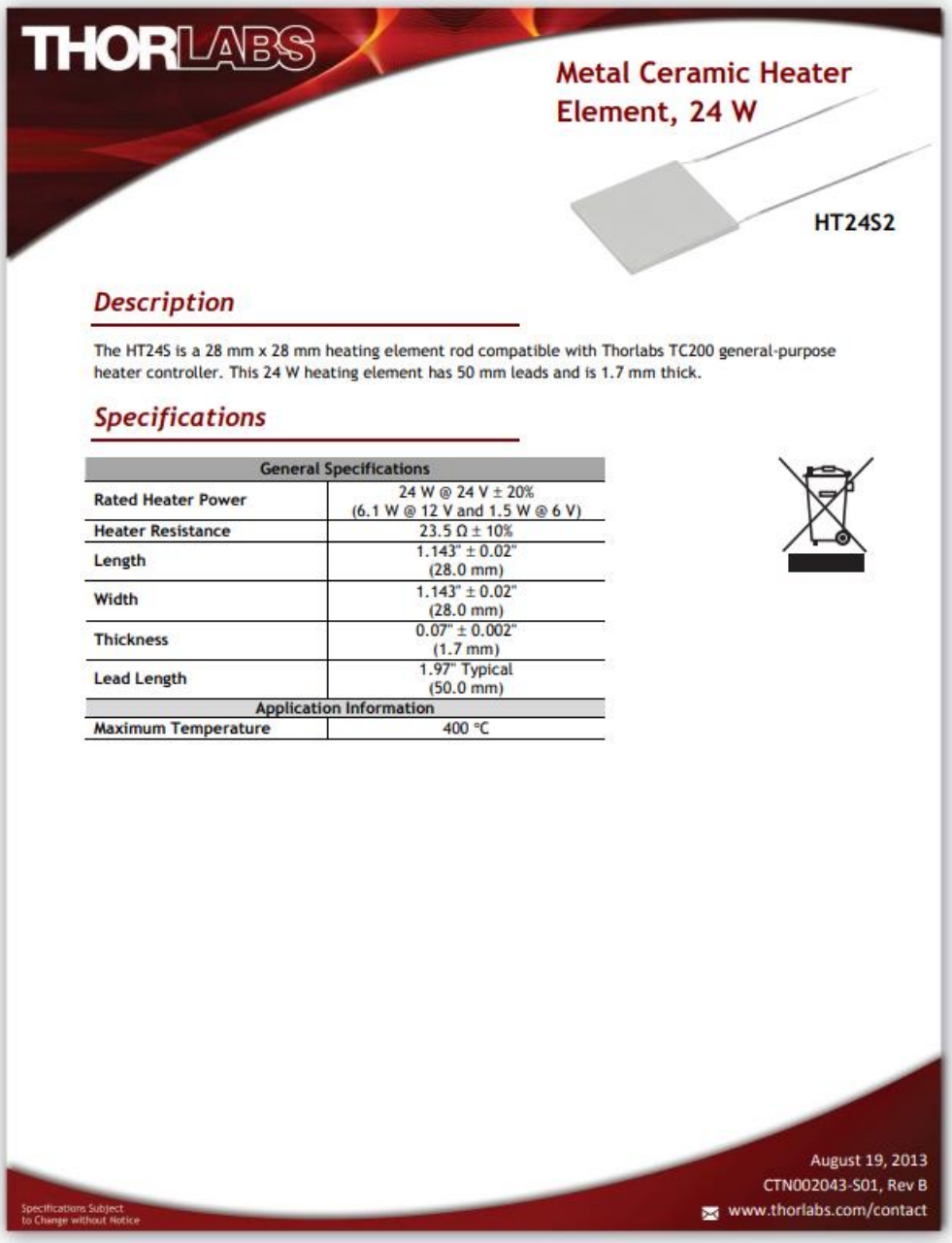

THORLABS

Metal Ceramic Heater Element, 24 W

HT24S2

Description

The HT24S is a 28 mm x 28 mm heating element rod compatible with Thorlabs TC200 general-purpose heater controller. This 24 W heating element has 50 mm leads and is 1.7 mm thick.

Specifications

General Specifications	
Rated Heater Power	24 W @ 24 V ± 20% (6.1 W @ 12 V and 1.5 W @ 6 V)
Heater Resistance	23.5 Ω ± 10%
Length	1.143" ± 0.02" (28.0 mm)
Width	1.143" ± 0.02" (28.0 mm)
Thickness	0.07" ± 0.002" (1.7 mm)
Lead Length	1.97" Typical (50.0 mm)
Application Information	
Maximum Temperature	400 °C

August 19, 2013
CTN002043-S01, Rev B
www.thorlabs.com/contact

Specifications Subject to Change without Notice

Figure A – 2: SpecSheet for Heatpad